UNIVERSITÉ GRENOBLE ALPES

THÈSE

Pour obtenir le grade de

DOCTEUR DE L'UNIVERSITÉ GRENOBLE ALPES

Spécialité: **Ingénierie-Matériaux Mécanique Énergétique Environnement Procèdes Production (510)**

Arrêt ministériel: 7 août 2006

Présentée par

Viviana BONILLA SIERRA

Thèse dirigée par **Frédéric-Victor DONZÉ**,
co-encadrée par **Luc SCHOLTÈS** et **Marc ELMOUTTIE**

préparée au sein du **Laboratoire 3S-R**
dans **l'École Doctorale IMEP2**

De la photogrammétrie à la modélisation 3D : Evaluation quantitative du risque d'éboulement rocheux

Thèse soutenue publiquement le **10.12.2015**,
devant le jury composé de:

Frédéric PELLET
Professeur à MINES ParisTech, Rapporteur
Farid LAOUAFA
HDR Chercheur à INERIS, Rapporteur
Yves GUGLIELMI
Professeur à Aix-Marseille Université, Membre
Frédéric-Victor DONZÉ
Professeur à l'Université Joseph Fourier, Membre
Luc SCHOLTÈS
Maître de Conférences à l'Université de Lorraine, Membre
Pierre PLOTTO
Docteur en Géologie et Président de la société IMSRN, Membre
Marc ELMOUTTIE
Chercheur Scientifique Sénior à CSIRO, Australie, Invité

Dedicado a mis padres, a mi hermano et à Yohan

Acknowledgements

I would like to thank Frédéric Pellet, Farid Laouafa and Yves Guglielmi, for kindly accepting to be part of the jury committee and for their insightful comments.

A special thanks to my thesis supervisor Frédéric-Victor Donzé from the Université Joseph Fourier (France), for his valuable orientation, collaboration and support during this research project. His ideas and his good spirit stimulated me to finally achieve my (our) goal.

I am grateful to my co-advisor Luc Scholtès from the Université de Lorraine (France), for his special dedication, providing very helpful and detailed suggestions as well as his important support through these three years.

Beyond the distances, Marc Elmouttie from the CSIRO (Australia), succeeded to co-supervise this research, contributing with important ideas, some of them materialised during my visit to CSIRO in Brisbane. I have to thank him for his availability, hospitality and for making possible such amazing professional and personal experience. Brett Poulsen and Andy Wilkins from the CSIRO's Energy Flagship are also thanked for their fruitful discussions and for their kindness.

Because of Frédéric-Victor, Luc and Marc orientations and dedicated support, I had the occasion to take part of international conferences, which boosted my work and helped me to keep the momentum until the end. Also thanks to their investment, we achieved to publish some articles before the end of this Ph. D. program. I am very glad I had the opportunity to work along with them.

Funding for this project was provided by IMSRN company (France). I am very thankful to Pierre Plotto, IMSRN president, for his participation as industrial advisor and sponsor.

During the time we coincided in 3SR Laboratory, Jérôme Duriez (currently in University of Calgary, Canada) kindly offered me his relevant advices and motivation. Merci beaucoup !

I want to thank Matías Silva, former post-doctoral researcher at 3SR Laboratory and current Associate Professor at the Universidad Técnica Federico Santa María (Valparaíso, Chile), for his advises and help provided while writing this manuscript. I am also grateful for his kind invitation to Valparaíso, where I gave my last scientific talk as Ph. D. student.

Special thanks to my dear friends and colleagues from Colombia, France, Chile, Greece, Italy, Germany, Netherlands, Catalonia, Syria, Poland, Brazil, Lebanon, Serbia, Croatia, Slovenia... This amazing diversity is one of the advantages of doing an international Master and working at 3SR Laboratory!

And to conclude, the origin of this Ph. D. program would not have been possible without completing a Master program. In consequence, I would like to thank Cino Viggiani, current Director of Laboratoire 3SR and head of the Geomechanics, Civil Engineering and Risks Master program, for his initial support that he has kindly kept to this day.

"No sólo no hubiéramos sido nada sin ustedes, sino con toda la gente que estuvo a nuestro alrededor desde el comienzo. Algunos siguen hasta hoy. ¡Gracias... totales!" *"No only we would have been nothing without you, besides everyone who has been with us since the beginning. Some still stand by us to this day. Thanks... a lot!"*

Gustavo Cerati, from Soda Stereo, at River Plate Stadium (Buenos Aires, Argentina) during *El Último Concierto* tour (20/09/1997).

Contents

List of Figures

List of Tables

Abstract

Title in english: The use of photogrammetry and 3D discrete element models to better assess rock slope stability

Structural and mechanical analyses of rock mass are key components for rock slope stability assessment. The complementary use of photogrammetric techniques and numerical models coupling discrete fracture networks (DFN) with the discrete element method (DEM) provides a methodology that can be applied to assess the mechanical behaviour of realistic three-dimensional (3D) configurations for which fracture persistence cannot be assumed.

The stability of the rock mass is generally assumed to be controlled by the shear strength along discontinuity planes present within the slope. If the discontinuities are non–persistent with their continuity being interrupted by the presence of intact rock bridges, their apparent strength increases considerably. In this case, the contribution of the rock bridges located in-between these discontinuities have to be accounted for in the stability analysis.

The progressive failure of rock slope involving non–persistent discontinuities can be numerically investigated based upon simulations performed using a DEM approach. The intact material is represented as an assembly of bonded particles interacting through dedicated contact laws that can be calibrated to properly represent the behaviour of the rock material. The advantage of the method is that it enables to simulate fracture initiation and propagation inside the rock matrix as a result of inter-particle bond breakage. In addition, pre-existing discontinuities can be explicitly included in the model by using a modified contact logic that ensures an explicit and constitutive mechanical behaviour of the discontinuity planes.

Stability analyses were carried out with emphasis on the contribution of rock bridges failure through a mixed shear-tensile failure process, leading to the generation of new failure surfaces. Jennings' formulation being considered to be one of the first rock slope stability analysis that evaluates the resistance to sliding as a weighted combination of both, intact rock bridges and discontinuity planes strengths, its validity was discussed and systematically compared to results obtained from numerical simulations. We demonstrate that the validity of Jennings' formulation is limited as soon as tensile failure becomes predominant and an alternative formulation is proposed to assess the resulting equivalent strength.

Regarding field slope stability, we show that the combination of high resolution photogrammetric data and DFN-DEM modelling can be used to identify valid model scenarios of unstable wedges and blocks daylighting at the surface of both natural and engineered rock slopes. Back analysis of a real case study confirmed that failure surfaces can be simulated as a result of both fracture propagation across rock bridges and sliding along pre-existing discontinuities. An identified wedge failure that occurred in an Australian coal mine was used to validate the methodology. Numerical simulations were undertaken to determine in what scenarios the measured and predicted failure surfaces can be used to calibrate strength parameters in the model.

The work presented here is part of a more global need to improve natural and mining hazards management related to unstable rock masses. We believe that the proposed methodology can strengthen the basis for a more comprehensive stability analysis of complex fractured rock slopes.

Keywords: Rock slope stability, photogrammetry, non-persistent discontinuities, rock bridges, progressive failure, DFN-DEM numerical modelling.

Résumé

Titre en français : De la photogrammétrie à la modélisation 3D : Évaluation quantitative du risque d'éboulement rocheux

Les analyses structurale et mécanique des pentes rocheuses constituent des éléments clés pour l'évaluation de leur stabilité. L'utilisation complémentaire de la photogrammétrie et des modèles numériques qui couplent les réseaux discrets de discontinuités (DFN selon son sigle en anglais) avec la méthode des éléments discrets (DEM selon son sigle en anglais), présente une méthodologie qui peut être utilisée pour évaluer le comportement mécanique des configurations tridimensionnelles (3D) de terrain pour lesquelles l'existence de discontinuités non persistantes peut être supposée.

La stabilité des masses rocheuses est généralement supposée être contrôlée par la résistance au cisaillement le long des plans de discontinuité. Si les discontinuités sont non persistantes, avec leur continuité interrompue par la présence de ponts rocheux (portions de roche intacte reliant la masse rocheuse au massif), leur résistance apparente augmente considérablement. Dans ce cas, la contribution des ponts rocheux localisés entre ces discontinuités doit être prise en compte dans l'analyse de stabilité.

La déstabilisation progressive des massifs rocheux dans lesquels des discontinuités non persistantes sont présentes, peut être étudiée par des simulations numériques réalisées à l'aide de l'approche DEM. La roche intacte est représentée comme un assemblage de particules (ou éléments discrets) liées entre elles par des contacts dont les lois de comportement spécifiques peuvent être calibrées pour représenter correctement le comportement de la roche. L'intérêt de la méthode est qu'elle permet de simuler l'initiation de la rupture et sa propagation à l'intérieur de la matrice rocheuse du fait de la rupture des contacts cohésifs entre les particules. De plus, les discontinuités préexistantes peuvent être prises

en compte explicitement dans le modèle en utilisant une loi de contact *ad hoc* qui assure un comportement mécanique représentatif des plans de discontinuité.

Des analyses de stabilité ont été effectuées et ont mis en évidence le rôle des ponts rocheux dans la génération de nouvelles surfaces de rupture qui peuvent se développer à travers des mécanismes de rupture mixte en traction et en cisaillement. On peut considérer la formulation de Jennings comme l'une des premières méthodes d'analyse de la stabilité des pentes rocheuses qui évaluent la résistance au glissement comme une combinaison pondérée des résistances mécaniques des ponts rocheux et des plans de discontinuité. Sa validité a été discutée et systématiquement comparée aux résultats obtenus à partir de simulations numériques. Il a pu être montré que la formulation de Jennings perd sa validité dès que la rupture des ponts rocheux intervient majoritairement par des mécanismes de traction. Une formulation complémentaire a alors été proposée.

En ce qui concerne l'étude de la stabilité des massifs rocheux sur site, il a été montré que l'association entre les données issues de la photogrammétrie en haute résolution et l'approche DFN-DEM peut être utilisée pour identifier des scénarios de rupture. L'analyse en retour de cas réels a montré que les surfaces de rupture peuvent être simulées comme le résultat de mécanismes combinant la fracturation des ponts rocheux et le glissement le long des discontinuités préexistantes. La rupture d'un dièdre qui a eu lieu dans une mine de charbon australienne, a été utilisée pour valider cette méthodologie. Des simulations numériques ont été réalisées pour déterminer les scénarios pour lesquels les surfaces de rupture simulées et celles repérées sur le terrain, peuvent être utilisés pour calibrer les paramètres de résistance du modèle numérique.

Le travail présenté ici répond à un besoin plus général visant à améliorer la gestion des risques naturels et miniers liés aux masses rocheuses instables. La méthodologie proposée constitue une alternative robuste dédiée à renforcer la fiabilité des analyses de stabilité pour les pentes rocheuses fracturées à structure complexe.

Mots-clés : Stabilité de falaises rocheuses, photogrammétrie, plans de discontinuité non-persistants, ponts rocheux, rupture progressive, modélisation numérique par DFN-DEM.

Introduction

Rock slope stability analysis requires a better understanding of the mechanical behaviour of fractured rock masses, which consist of interlocking blocks of rock material separated by persistent or non-persistent discontinuity planes (Hoek, 1983). Indeed, the mechanical behaviour of fractured rock masses is influenced by the presence of discontinuities, inducing variations in hydraulic conductivity, strength reduction and increase in deformation rate (Dershowitz, 1984). Sufficient knowledge of the failure mechanisms observed in fractured rock slopes is essential to build capable models for several geotechnical applications. In consequence, stability analysis methods get more complex as more realistic and accurate geotechnical models are required to include geological, structural, rock mass and hydrogeological components (Read et al., 2009).

Environments such as mountainous zones, quarries or mines are frequently exposed to unstable rock blocks prone to collapse. Lambert et al. (2012) defined two successive mechanisms triggering rock slides: *i)* the detachment of a rock block (*i.e.* failure) and, *ii)* its propagation down the slope. Rock failure and rock slides are both matter of study focussed to minimise the risk and prevent incidents. Special attention is given here to the failure mechanisms taking place before the rock slide occurs, based on the fact that slope instabilities are the source of the problem.

There are evidences that massive boulders may endanger the population, as it occurred in the French commune Saint-Martin-Le-Vinoux, where several tons of rock detached from a nearby cliff and rolled down the hill, stopping around 200-m away from a hamlet (Figure 1). Detaching blocks may also cause route incidents, as shown in Figure 2, where the access to the ski resorts located in the Tarentaise Valley (France) was temporary closed during winter 2014-2015.

Engineered slopes, such as open pit mine walls, are also susceptible to rock slides

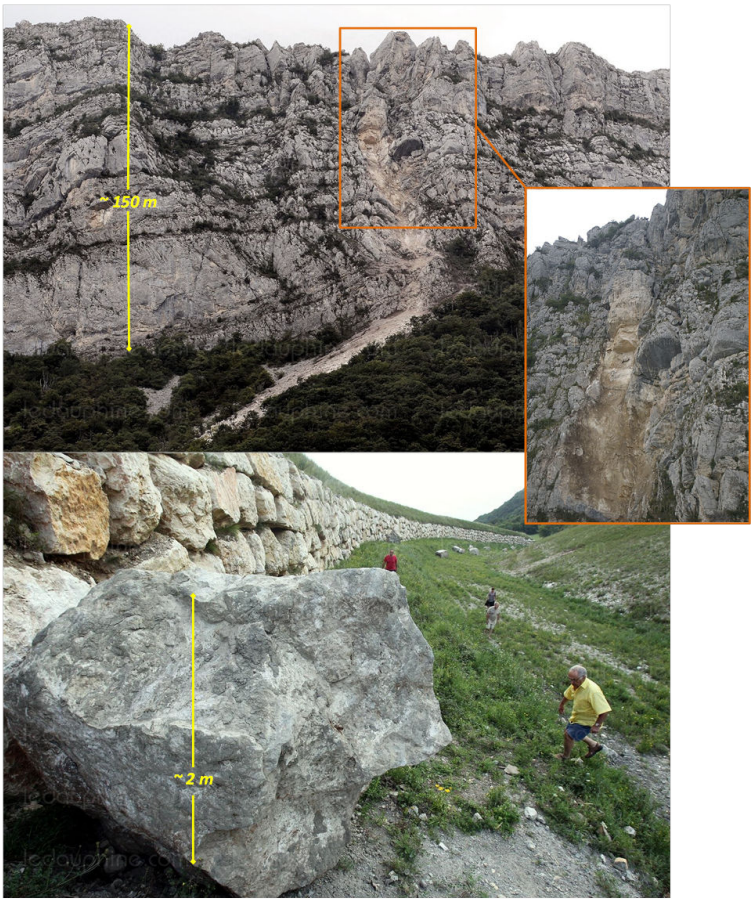

Figure 1: Mount Néron (France) after a rockfall occurred on 14 August 2011. The rockfall is evidenced by the long bright scar left on the slope. A detail of the zone of detachment and a remaining rock block on the slope are highlighted in orange (top). Collapsed block next to the retaining barrier (bottom) (*Credit: Christophe Agostinis - ledauphine.com*).

due to the mechanical disturbance induced by the mineral exploitation. Pre-existing discontinuities reactivate and may create new ones. The elevated height and steep overall dip angle of the pit walls are also problematic, taking into account that benches can reach heights between 30 m and 50 m, with face angles as steep as 90°, facilitating blocks tilting (Figure 3).

Certain rock slopes may remain in equilibrium over a relatively long period of time. However, failure can occur when the rock mass strength is progressively reduced due to triggering mechanisms such as weathering, fatigue and fracture propagation through intact rock segments (Eberhardt, 2008), known as rock bridges. These rock bridges are usually defined as patches of intact material connecting the potentially unstable rock blocks to the slope (Figure 4). Depending on their distribution (quantity and location on

Figure 2: Detached rock block on the road D117 in the Tarentaise Valley (France). Picture taken on 27 February 2015 (*Credit: savoie.fr*).

Figure 3: Highly fractured walls and detached blocks observed in an open pit coal mine (Australia)

the failure surface), the rock bridges have an important influence on the equilibrium of the rock block.

Indeed, rock bridges provide both shear and tensile strength to the fractured rock mass. Their contribution is therefore considered essential to determine the stability of the rock slope in presence of non-persistent discontinuities. Taking into account rock bridges in the geotechnical model may result in considerable differences when assessing the degree of stability of the slope (Scavia, 1990). As an early example, the analytical approach proposed by Jennings (1970) accounts for the presence of intact rock bridges along failure surfaces, and allows to describe failure in fractured rock slopes as a combination of shearing along discontinuities and fracturing through intact rock bridges. Following this concept, another simple fracture mechanics model based on crack growth was developed by Kemeny (2003) in order to predict time-dependent degradation of joint cohesion as a result of the breakage of rock bridges along co-planar discontinuities. More recently, robust numerical models based upon complex configurations including non-coplanar discontinuities have been proposed to simulate rock slopes failures, either by tensile or shear failure of intact rock bridges (Havaej et al. (2014); Mejía-Camones et al. (2013); Eberhardt et al. (2004)).

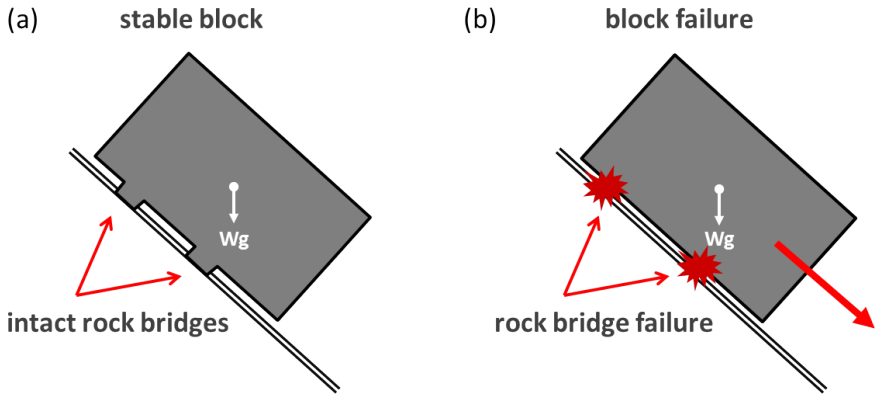

Figure 4: Scheme of (a) intact rock bridges providing stability to a block, and (b) block failure due to rock bridges failure

Rock bridges distribution along the failure surface is difficult to determine and depend on diverse factors such as rock weathering and the discontinuities distribution. *In situ*, geophysical methods such as ground penetrating radar (GPR) can be used to determine the spatial distribution of rock bridges inside the rock mass (Deparis et al., 2007), but can be only applied for specific surveys limited by the high electrical resistivity of some rock slopes (Lévy, 2011).

Back analysis of collapse events are an alternative methodology to study and understand the role of rock bridges in the stability of rock slopes. As a matter of fact, after failure, the rock bridges can be visually recognisable from digital images by colour contrast on the failure surface, as shown in Figure 5. For instance, Lévy (2011) carried out a closer

inspection of failure surfaces to assess the proportion of rock bridges involved in the stability of collapsed rock masses. A qualitative surface analysis led to estimate the potential failure mechanisms that triggered fracture, either by tensile or shear stresses. Furthermore, Frayssines and Hantz (2009) suggested that percentage of rock bridges ranging from 0.2% to 5% of observed failure surfaces was sufficient to keep rock masses in equilibrium.

Three-dimensional (3D) images generated by photogrammetric techniques can be also used as a reliable tool to identify roughness variation of fresh rock patches (Bonilla-Sierra et al., 2015) and, moreover, can provide structural information such as distribution and configuration (dip and dip direction) of the main discontinuity planes.

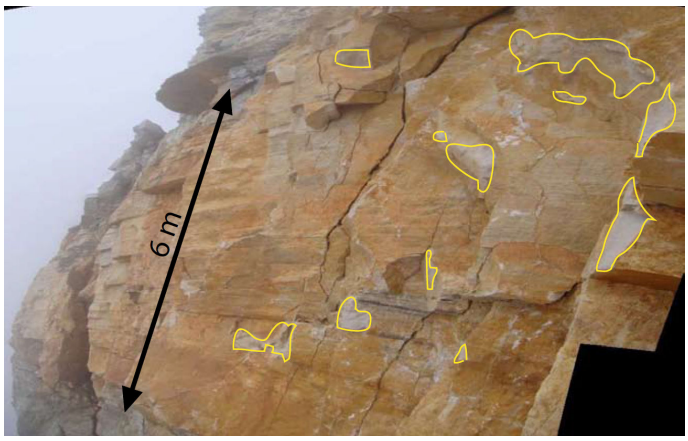

Figure 5: Rupture surface after the collapse of a calcareous rock column, in Vercors massif (France). The location of rock bridges are identified as fresh intact rock zones circled in yellow (Lévy, 2011)

Baczynski et al. (2000) mentioned that rock slope failure can occur as a consequence of different mechanisms, such as sliding along both pre-existing planar discontinuities, or circular shallow surfaces in the particular case of weak rock masses. The approach presented here, aims to simulate those phenomena accounting for all these mechanisms, *e.g.* shear failure along discontinuities, tensile and shear failure across rock bridges and progressive failure inside the intact rock.

An advanced numerical modelling technique is proposed to investigate failure mechanisms in order to improve rock slope stability analysis and contribute to the global need to better manage natural hazards and open pit mine operation. Three-dimensional photogrammetry was utilised for detailed surface mapping as superficial recognition of the main discontinuities planes and their geometrical properties (dip and dip direction), which are considered as a critical input to build up pertinent discrete fracture networks (DFN). These DFN can be later plugged into the mechanical model in order to enhance the rock mass numerical model.

The discrete element method (DEM) has been chosen here for modelling the rock

mass due to its capability to represent the progressive failure of the rock matrix. The discrete elements (DE), making up the assembly that represents the rock matrix, are bonded together through a dedicated constitutive law that enables to simulate the rock mass behaviour. The scope of this Ph.D. thesis is to develop a methodology based on the application of the DEM to model slope failure as a result of fracture propagation and coalescence in the presence of non-persistent discontinuities, numerically represented by the aforementioned DFN (Scholtès and Donzé, 2012).

The coupled DFN-DEM model is carefully adapted to better assess and predict rock slope instabilities by highlighting the contribution of rock bridges. The advantage of this approach is that rock bridges can be explicitly integrated into the numerical model, represented as zones of intact rock delimited by non-persistent discontinuities. Several questions related to rock slope stability, such as existence and failure of rock bridges, are discussed in each chapter of this dissertation. Considered as a critical component of the strength of unstable masses, the contribution of rock bridges is investigated and assessed in real and idealised case studies.

The dissertation is composed of four chapters. The **first chapter** resumes the state-of-the-art of the methods developed to assess rock slope stability leading to the choice of the proposed method as an innovative and effective contribution. The **second chapter** presents an application of the methodology from photogrammetric data acquisition to DFN-DEM modelling, to the case of a natural rock slope located in the Chartreuse massif, in the French Alps. The mount Néron case was analysed to investigate the presence of rock bridges on the back side of an unstable rock block, and their contribution to the destabilisation process. The simulated progressive failure and the coalescence of pre-existing discontinuities succeeded to reproduce the actual rock bridge failure that triggered the rock block instability. From this chapter, an article was published (February 2015) in *Acta Geotechnica*. In the **third chapter**, the contribution of rock bridges to rock slope stability is investigated using a DEM model, discussing the reliability of Jennings' formulation (Jennings, 1970), which is one of the pioneer methodologies proposed to estimate the strength contribution of rock bridges to the stability of fractured rock masses. An idealised slope was studied in presence of non-persistent discontinuities to assess the rock mass strength in the case of translational sliding failure. An article issue of this chapter has also been published (September 2015) in the *International Journal of Rock Mechanics and Mining Sciences*. The **fourth chapter** presents an implementation of the DFN-DEM model to an open pit mine wall case. A back analysis of a wedge failure was carried out, in order to assess the effect of the mechanical properties and the geometry, *i.e.* the size of rock bridge, on the stability and also on the failure surface generation. An article on this work has been submitted to the *Journal of Rock Mechanics and Geotechnical Engineering*. **Annexe A** presents an evaluation of a selected set of software which provide facilities to create 3D models used for geotechnical analysis purposes.

CHAPTER 1

Rock slope stability analysis

The causes of rock slope instabilities need to be understood in order to provide suitable tools for stability analysis. The difficulties arises from the complexity of the system to consider, accounting for complex three-dimensional (3D) configurations involving geological structures and presence of rock bridges. In order to assess rock slope stability, several analysis techniques have been developed based on simplified representations of rock masses and their mechanical behaviour. As a result, numerous analytical methods and numerical modelling techniques applied to conceptual and realistic scenarios, have been proposed to describe the mechanical response of unstable rock masses.

Within the numerical modelling techniques, two-dimensional (2D) and 3D models have been widely developed. Although 2D models can offer a preliminary estimation of failure mechanism, they may provide a misleading interpretation of the mechanism actually involved. 3D models enable a realistic representation of rock slopes, but are computationally expensive. As their complexity increases, the models become difficult to control due to the large number of parameters involved to properly simulate the mechanical behaviour of both, the rock material and the discontinuities.

Nevertheless, numerical models are required to provide an advanced alternative to conventional methods for rock slope stability widely used in geotechnical and geomechanical engineering. The goal of this research project is to present a methodology based on numerical simulations as a potential tool for assessing the stability of complex and real scale 3D configurations. Obviously, some simplifications were done in order to efficiently manage the computational cost. However, the results are representative and comparable to the observed failure mechanisms.

Because of its capability to simulate progressive failure mechanisms, a model based on the discrete element method (DEM) was used to represent the medium as an assembly of bonded discrete elements (DE). In addition, discontinuities can be included into the numerical model, in order to consider their mechanical properties and better represent fractured rock masses behaviour. As a result, failure can be simulated as a combination of fracture propagation through the intact rock and sliding along pre-existing discontinuities. The proposed methodology from 3D surface and structural data acquisition to numerical modelling applied to rock slope stability assessment will be presented in detail in the following sections.

1.1 3D surface and structural data collection

Three-dimensional (3D) models have become a valuable tool for geotechnical and geomechanical analysis, since they provide a realistic representation of rock slopes. There are several techniques for creating 3D surface models, specially developed to be applied in the analysis of deformation and evolution of natural and engineered slopes. For instance, at large-scale, satellite imagery resources such as Synthetic Aperture Radar (SAR) images, can be used to detect movement of large slopes or glaciers in high mountainous environment where access may be difficult or even dangerous. For example Echelard (2014) investigated the potential displacements of a rock-glacier in the French Alps, using European Remote Sensing satellite (ERS) archives and high resolution images taken using a new generation sensor TerraSAR-X, allowed to observe the main features of the glacier and derive more accurate displacement fields (Figure 1.1).

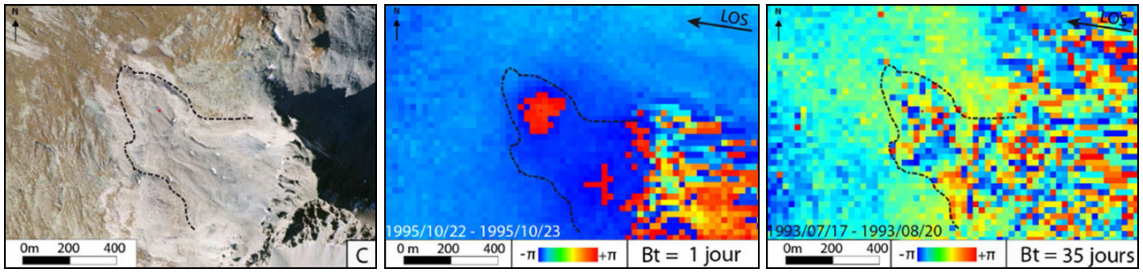

Figure 1.1: Example of displacements detected by using ERS interferograms, from the Pierre Brune NW rock-glacier, in the Vanoise massif (France). Timestep: 1 day and 35 days (LOS: Line Of Sight). After Echelard (2014)

Other methods more commonly used to study the stability of rock slopes are laser scanning and photogrammetry due to their adaptability to the study of slope surfaces (Figure 1.2). Laser scanning consist of the reconstruction of 3D surfaces from high resolution point clouds which can also be used to track large scale displacement (Figure 1.3).

Similarly, photogrammetry is an image-based technique capable of generating 3D images from 2D photographs. Both methods are used interchangeably and their accuracy may be comparable depending on the distance between the observer and the target and the accessibility to the slope (Bottelin et al. (2014); Sturzenegger and Stead (2009); Salvini et al. (2013)). Note however that to achieve comparable point cloud densities using laser scanning, both the scanning mode of the laser and the field procedure used must be appropriate (*e.g.* Sturzenegger and Stead (2009)).

Data acquisition can be done at large-range, *e.g.* aerial scanning (by drone, by aeroplane or by helicopter), or at close-range, as for example terrestrial photogrammetry. The reliability and accuracy of both 3D reconstruction methods have been evaluated by several authors (Sturzenegger and Stead (2009); Haneberg (2008); Travelletti et al. (2012)), demonstrating in addition their effectiveness for characterizing rock masses and their contribution to improve the efficiency of stability analysis (Figure 1.4).

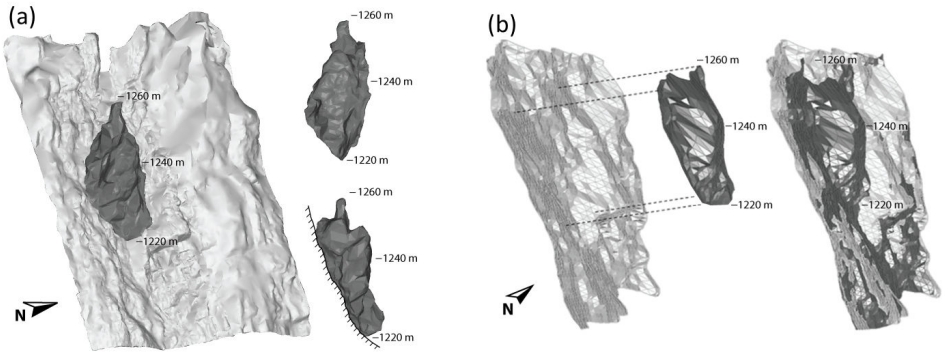

Figure 1.2: 3D model of an unstable rock block laying on a slope (a) Laser scanned model. (b) Photogrammetric model. After Bottelin et al. (2014)

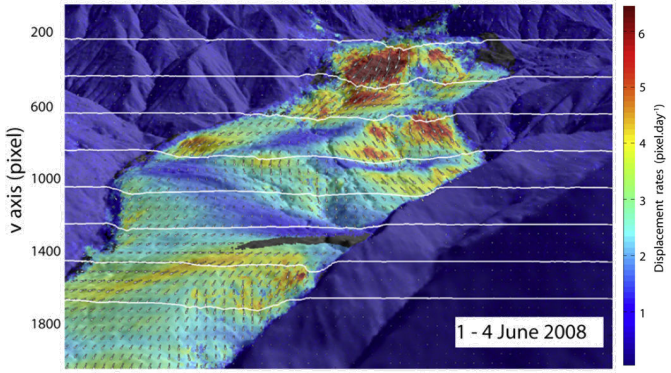

Figure 1.3: Displacement rate amplitude over 5 days from the Super-Sauze landslide (France), usign laser scanning data. After Travelletti et al. (2012)

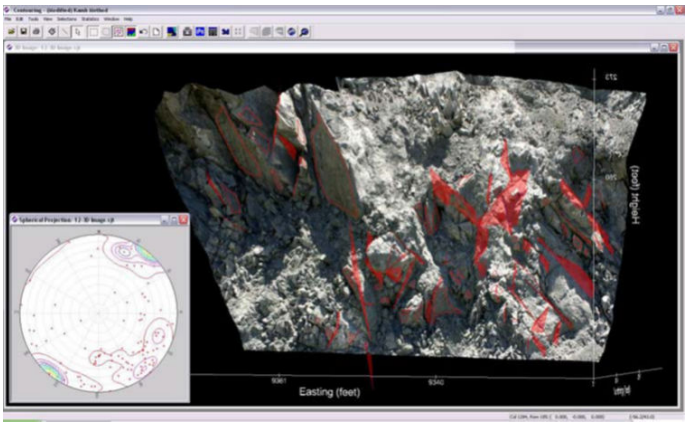

Figure 1.4: Detailed structural information gathered from a 3D photogrammetric model of a quarry located along the San Andreas fault (United States). After Haneberg (2008)

In particular, photogrammetry has become a valuable technique to build up 3D models of rock slope used in structural analysis, preferred over laser scanning due to budget limitations and implementation simplicity. Recent software packages have greatly improved algorithms for data extraction and image reconstruction, providing an easy method to create realistic and accurate 3D surfaces from good quality overlapping, and often georeferenced (surveyed), 2D pictures (Poropat (2006); Sturzenegger and Stead (2012)). Several commercial photogrammetry packages are available for the non-expert users to create 3D models from a set of images. Among them, the most commonly used for geotechnical support are Agisoft Photo Scan Pro (Agisoft, 2013), Smart3D Capture (Acute3D, 2012), Sirovision (Sirovision, 2010) and 3D Analyst (ADAM-Technology, 2007). The two latest are capable of interpreting superficial structures directly on the generated 3D surfaces, making them more suitable to rock slope stability analysis.

Basically, the software processes 2D images from a chosen scene, following an automatic work-flow which includes the 3D reconstruction done by plotting out key points on the photograph to give the software a sense of scale and proportion within the image. Afterwards, these points and data are used by the program to create a realistic 3D model of the object (Figure 1.5). Annexe A presents an evaluation of a selected set of software which provide facilities to create 3D models used for geotechnical analysis purposes.

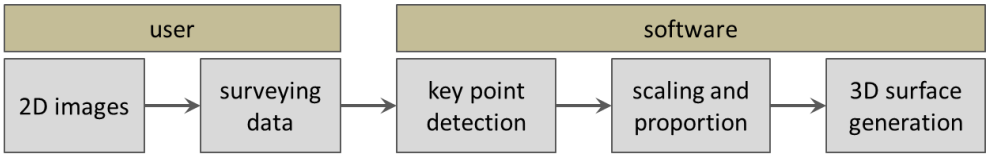

Figure 1.5: Photogrammetry simplified workflow

Terrestrial photogrammetry has been chosen here as the 3D reconstruction technique

to reproduce realistic surfaces in some of the analysed case studies. In particular, Sirovision (Sirovision, 2010) was used, due to its capability to accurately build up 3D surfaces and for its supported discontinuity detection tool. This software was created specifically for geological and geotechnical mapping technology developed by the CSIRO, who has provided a specific license to be used under the framework of this research project.

1.2 Available methods for rock slope stability analysis

Modelling the mechanical response of fractured rock masses implies dealing with complexities such as heterogeneous surfaces and pre-existing discontinuities (geometry) and inhomogeneous material properties (mechanics). Therefore, advanced numerical models specially designed to couple slope geometry and mechanical properties, are the most adapted methods to assess slope stability. Depending on their approach, the numerical techniques are commonly distinguished as continuum and discrete based methods.

Numerical models are now widely used in geotechnical engineering. Their complexity and accuracy are constantly improved by researchers looking for more sophisticated and reliable solutions to better reproduce the mechanical response of fractured rock masses. These methods have evolved in the last 25 years from basic graphic and analytical calculations to advanced simulations performed on powerful computers. Nowadays, the available methods range from simple finite slope and planar failure limit equilibrium analysis to sophisticated coupled finite-discrete element method (FEM-DEM) models (Stead et al., 2001). The main available methods are summarised in Table 1.1.

Classic finite element method (FEM) applied to geomechanical modelling can represent the discontinuities implicitly or even explicitly through the use of joint elements. They are considered through constitutive laws that can simulate their physical behaviour. In particular, a method for rock slope stability analysis proposed by Pariseau et al. (2008) presents a new finite element fractured rock mass model by defining representative volume elements (REVs), also known as domains, within the rock matrix, which contains explicitly non persistent discontinuities and intact rock bridges. With this approach, intact rock and discontinuity failure mechanisms can be reproduced and integrated to the global rock slope stability analysis. In this context, Pouya (2015) developed a numerical formulation that allows using FEM for modelling the flow in fractured porous media. Nevertheless, the continuum approach is limited when fracture propagation occurs (Donzé et al., 2009). To overcome this limitation, FEM enhancements have been proposed to simulate fracture propagation through finite elements, such as the extended finite element method (XFEM), which have been successfully used in several mechanical applications (Zi and Belytschko, 2003).

As an alternative, the DEM has been introduced and carefully adapted to represent

Conventional method	brief description
Stereographic and kinematic	Provides a preliminary failure evaluation based on critical discontinuities and their representative shear strength. May lead to identify keyblocks.
Limit equilibrium	Capable of simulating different basic failure modes such as planar, wedge and toppling. Based on slope geometry, rock mechanical properties (cohesion and friction), discontinuity shear strength. Can estimate factor of safety. Suitable to 2D and 3D modelling.
Numerical method	**brief description**
Continuum	Elastic and elasto-plastic constitutive laws can be implemented to model deformation and failure. Shear strength can be simulated on the surfaces. Suitable to dynamic analysis.
Discontinuum	Block deformation and relative movement are allowed. Can model complex mechanical behaviour combining rock discontinuities mechanical properties. Intact rock behaviour simulated through elasto-plastic laws. Suitable to dynamic analysis.
Hybrid/coupled modelling	Combination of discontinuum and continuum approaches to simulate complex and large-scale problems.

Table 1.1: Summary of conventional and numerical modelling techniques for slope stability. Adapted from Stead et al. (2001)

the material as an assembly of separated elements, so-called particles or blocks, interacting between each other through defined mechanical laws to reproduce the behaviour of rock masses. Furthermore, it has been shown that DEM models can explicitly account for discontinuities as specific discrete fracture networks, also known as DFN. The DFN provides an important tool to explicitly represent the properties and uncertainties of discontinuities within the rock mass. This 3D representation also supports visualisation of various phenomena, such as rock mass deformation. For example, Wang et al. (2003), Eberhardt et al. (2004) and Eberhardt (2008) presented two-dimensional (2D) discrete models to simulate rock mass failure in presence of discontinuities (Figure 1.6). Later, three-dimensional (3D) modelling was implemented by Sturzenegger and Stead (2012),

Scholtès and Donzé (2012), Harthong et al. (2012) and Damjanac et al. (2013), among others (Figure 1.7) in order to provide a better insight on complex rock mass configurations.

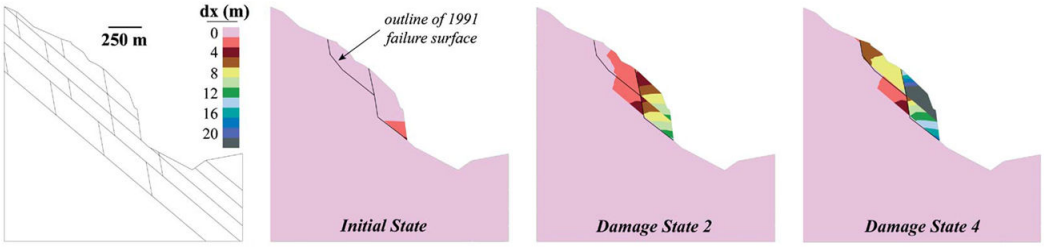

Figure 1.6: 2D discrete modelling of progressive failure in the presence of discontinuities represented by the horizontal displacement field. After Eberhardt et al. (2004)

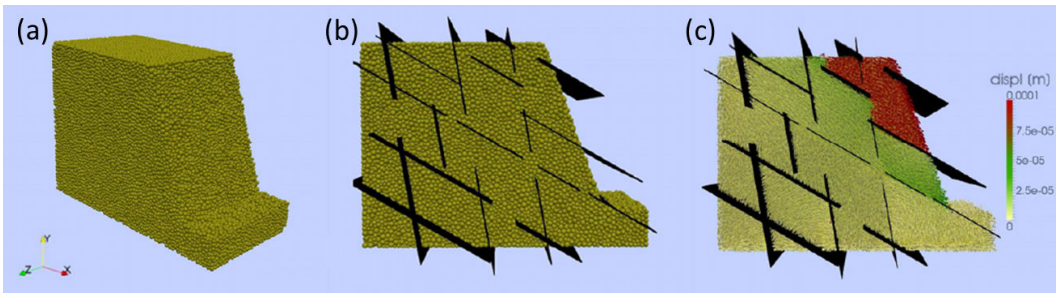

Figure 1.7: 3D discrete modeling of a slope in the presence of non-persitent discontinuities. (a) 3D view of the DEM model, (b) side view of the DFN configuration plugged into the DEM model and (c) side view of the displacement field at failure. After Scholtès and Donzé (2012)

Despite the numerous works published on this topic, the development of DFN-DEM geomechanical models, applied to the analysis of real scale problems, is quite recent. To mention some prominent works, Li et al. (2002) used a 3D-DEM model coupled with sets of pre-existing discontinuities surveyed on-site, in order to simulate the excavation of a high slope located at the Three-Gorges area (China). Sturzenegger and Stead (2012) investigated the prehistoric Palliser Rockslide that occurred in the Rocky Mountains (Canada), implementing photogrammetric techniques to gather 3D-surface data. The back-analysis of the failure surface provided evidence of failure mechanisms such as sliding along curved and planar surfaces. The 3D model simulated an identified wedge failure, as shown in Figure 1.8a. A complementary 2D FEM analysis was carried out to specifically identify intact rock fracturing in zones between non-persistent discontinuities . The different rock bridges scenarios were simulated to estimate their strength contribution (Figure 1.8b). More recently, a DFN-DEM approach was used by Grenon et al. (2014) to evaluate the

mechanical response of fractured rock mass, depending on the variability in structural data surveyed in a Canadian gold mine. Havaej et al. (2015) demonstrated the application of photogrammetry in discontinuity characterisation plugged into DEM simulations, to evaluate the stochastic nature of geological structures and its influence on slope failure mechanisms, at a slate quarry located in United Kingdom (Figure 1.8c).

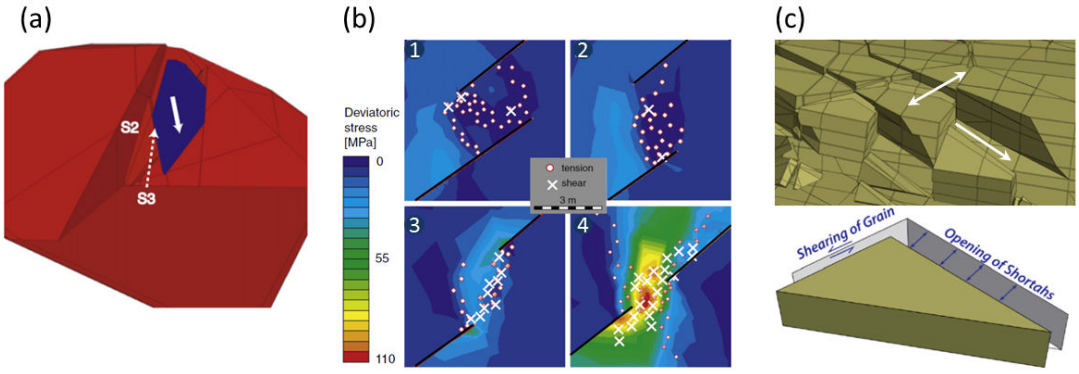

Figure 1.8: 3D coupled DFN-DEM models for rock slope stability applied to real cases. (a) Simulation of wedge failure mechanism in the Palliser Rockslide case. The dark blue block is showing sliding in the direction of the white arrow, after Sturzenegger and Stead (2012). (b) complementary FEM model showing the deviatoric stress distribution within the Palliser Rockslide and the elements failed in tension and shear for four types of intact rock bridges, after Sturzenegger and Stead (2012) (c) Illustration of opening and shearing failure mechanisms simulated for the Delabole slate quarry, after Havaej et al. (2015)

Adopting the DEM approach, the mechanical behaviour of both, the rock matrix and the discontinuities can be simulated taking into account the complexity of each one. Therefore, methods for rock stability analysis become more representative and adapted to predict potential rock block collapses.

1.3 From terrestrial photogrammetry to coupled DFN-DEM modelling

Regarding the pertinence of terrestrial photogrammetry for 3D surface reconstruction and discontinuities modelling, a DFN-DEM approach is proposed as an alternative for assessing the stability of real fractured rock slopes. The methodology aims to couple the mechanical behaviour of pre-existing discontinuities with the mechanical response of the rock matrix with the possibility for describing fracture initiation and propagation.

Spatial distribution of exposed faults and discontinuities within the rock mass, which can be recognised by structural models, can be explicitly represented by DFN models (Sturzenegger, 2010). The DFN offers a practical tool to have an insight about failure mechanisms development, particularly when the failure involves sliding along the major structures and fracture propagation within the intact rock matrix, *i.e.* rock bridges (Read et al., 2009).

For the cases presented here, the numerical topography and the structural data were acquired using the aforementioned software Sirovision (Sirovision, 2010). The software required overlapping stereo pairs of digital photographs and survey information to create 3D digital models that can be scaled and oriented within a specified coordinate system (Gates et al., 2012). Since Sirovision provides a functionality for rock mass discontinuity mapping, visualisation and analysis, the discontinuities can be detected directly on the surface, and then represented as 3D polygons or planes. In addition, the generated 3D slope surface can be used to generate a closed volume, which can be imported along with the DFN into the mechanical model. Once the geometrical model is set up, the intact rock mass can be modelled as a set of bonded particles packed into the generated volume that represents the slope (Donzé and Magnier, 1995) (see Chapter 2 for a detailed description of the packing procedure).

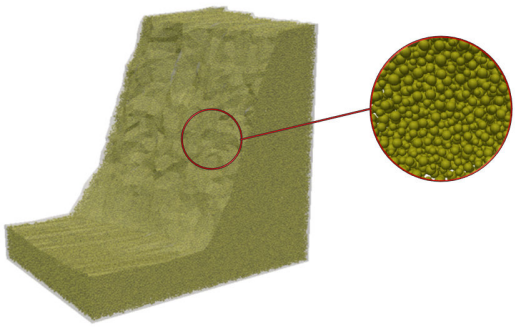

Figure 1.9: DE packed into the closed volume representing the rock slope

Cundall and Hart (1992) first defined DEM modelling as an approach that allows finite displacement of DE and recognises new contacts between them all along the simulation. The numerical simulations described in this research project were implemented in Yade Open DEM platform (Kozicki and Donzé (2008); Kozicki and Donzé (2009)), an extensible open-source software based on the DEM dynamic formulation. The algorithm implemented is based on two principles: *i)* the computation of interaction forces between DE through dedicated constitutive laws and *ii)* the computation of the displacement of each DE by applying Newton's second law to time-integrate the resulting acceleration (Scholtès and Donzé, 2012).

The following presentation of the local constitutive law implemented here is a summarise of the rigorous modelling procedure detailed presented in Scholtès and Donzé (2012); Scholtès and Donzé (2013). The inter-particle bonds obey an elastic-brittle behaviour in both normal and tangential directions. The interaction force F applied to one DE to another, may be decomposed into the normal force F_n and the shear force F_s which are related to the relative normal (U_n) and the incremental shear (ΔU_s) displacements through the stiffnesses, k_n and k_s, in the normal and the tangential directions, respectively (Figure 1.10a,b). In consequence, in compression F_n is given by the following linear expression:

$$F_n = k_n \, U_n \tag{1.1}$$

Note that, for $U_n > 0$ the DE get closer.

The normal interaction force in tension is also linear depending on k_n but with $U_n < 0$, which means that the DE get apart from one another. The maximum acceptable tensile force, $F_{n\ max}$, is a function of the tensile strength, T, such that,

$$F_{n\ max} = -T \, A_{int} \tag{1.2}$$

where $A_{int} = \pi(_{min}(R_a, \ R_b))^2$ is the interacting area between DE a and b, respectively.

The shear force F_s is calculated by updating its orientation and intensity depending on the increment of shear force, which depends on ΔU_s, such that,

$$F_s = [F_s]_{t-1} + k_s \, \Delta U_s \tag{1.3}$$

The inter-particle bonds can break either by tension or shear failure mechanisms according to a modified Mohr-Coulomb criterion with a tensile cut off. After bond breakage, particles can interact through frictional contact. The maximum shear force $F_{s\ max}$ is characterised by F_n, the cohesion C, the local frictional angle φ and the local residual frictional angle φ'. Therefore, the maximum shear force for a bonded interaction is calculated according to,

$$F_{s\ max} = F_n \tan\varphi + C A_{int} \tag{1.4}$$

Although only purely frictional new contacts between DE can appear during the simulation, with a maximum shear force defined as,

$$F'_{s\ max} = F_n \tan\varphi' \tag{1.5}$$

The rupture criterion is illustrated in Figure 1.10c.

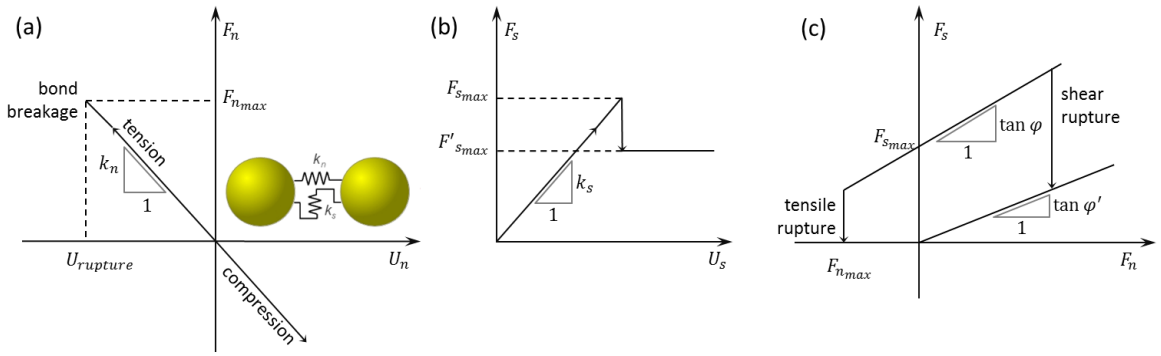

Figure 1.10: Local constitutive law between DE. (a) Normal interaction force between DE. (b) Tangential force between DE. (c) Modified Mohr-Coulomb criterion. Adapted from Scholtès and Donzé (2012)

For the discontinuities, a smooth joint model (SJM) formulation was used to explicitly represent these structures into the numerical medium. The discontinuities are simulated by slip surfaces located between the DE laying on the opposite side of the discontinuity surface (see Scholtès and Donzé (2012); Scholtès and Donzé (2013); Scholtès and Donzé (2015); Harthong et al. (2012) for details). The SJM formulation provides a direct equivalence between the properties of the macroscopic discontinuity and the properties of the inter-particle bonds crossing this discontinuity. This formulation also allows the possibility to model dilatancy in the fracture. Moreover, the SJM ensures that the behaviour of the simulated discontinuity surface is independent of the inherent discretisation or roughness produced by the arrangement of the particles along the interface (Scholtès and Donzé, 2015).

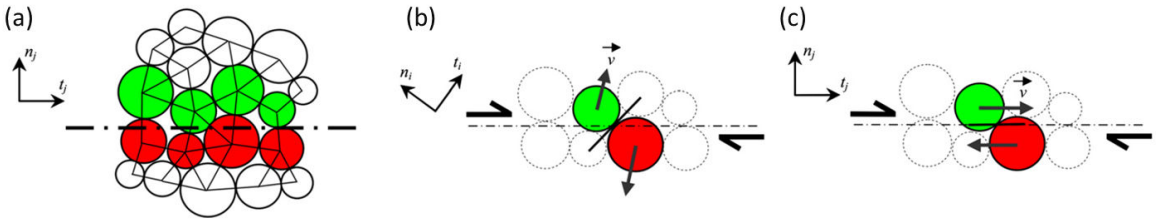

Figure 1.11: Smooth joint model. DE are coloured depending on the side of the plane to which they belong. (a) Identification of the inter-particle bonds crossing the discontinuity plane, defined by n_j and t_j vectors. (b) Classic inter-particle bond orientation, defined by n_i and t_i vectors. (c) Modified inter-particle bond orientation. After Scholtès and Donzé (2012)

The model can be calibrated so as to simulate the macroscopic behaviour of brittle rocks. The procedure followed for this research project was based on Scholtès and Donzé

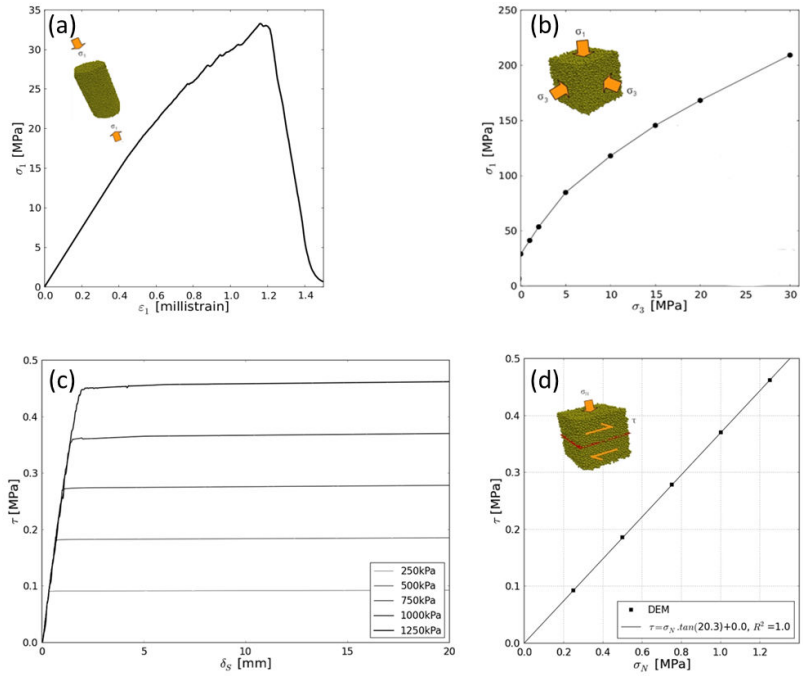

Figure 1.12: Simulation of the macroscopic behaviour of fractured rock masses. (a) Stress-strain curve obtained from uniaxial compressive test simulation performed on the rock matrix. (b) Predicted failure envelope of the rock matrix. (c) Stress–strain curves obtained from direct shear test simulations performed on the calibrated joint model under a constant normal load σ_n ranging from 0.25 to 1.5 MPa. τ is the shear stress and δ_s is the shear displacement of the joint and (c) the corresponding predicted failure envelope for the rock joint.

(2013) proposed calibration methodology to determine the related DEM parameters. The elastic properties and the strength of the simulated rock are determined by performing uniaxial tensile and compressive tests, as well as triaxial tests simulations (Figure 1.12.

The non-linearity of the failure envelope is controlled by the number of interaction forces per DE, which defines the degree of DE interlocking (see Scholtès and Donzé (2013) for details). This degree of DE interlocking can be set by defining a given interaction range coefficient (γ_{int}) that allows for near neighbour interaction. The larger this coefficient is, the larger the number of interaction forces and the more competent the material is (Figure 1.13a). On the contrary, if the coefficient is close to one, the simulated material behaves as a cohesive granular material (Figure 1.13b).

The methodology based on the DFN-DEM model for rock slope stability analysis is developed in order to describe the macroscopic behaviour of fractured rock masses. The fracture process is tracked by following the progressive failure induced by the strength reduction and influenced by the presence of pre-existing discontinuities. Coupled DFN-

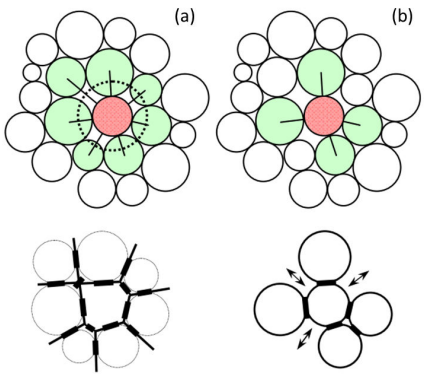

Figure 1.13: Interaction range coefficient defining the degree of DE interlocking: (a) $\gamma_{int} > 1$ and (b) $\gamma_{int} = 1$. After Scholtès and Donzé (2013)

DEM model is presented as an innovative technique that can provide a reliable rock slope stability model, due to the realistic aspect of structural 3D surface obtained by photogrammetry and the simulation of the progressive failure mechanisms taking place in rock bridges (Scholtès and Donzé, 2012). Figure 1.14 presents a general overview on the DFN-DEM approach implemented here.

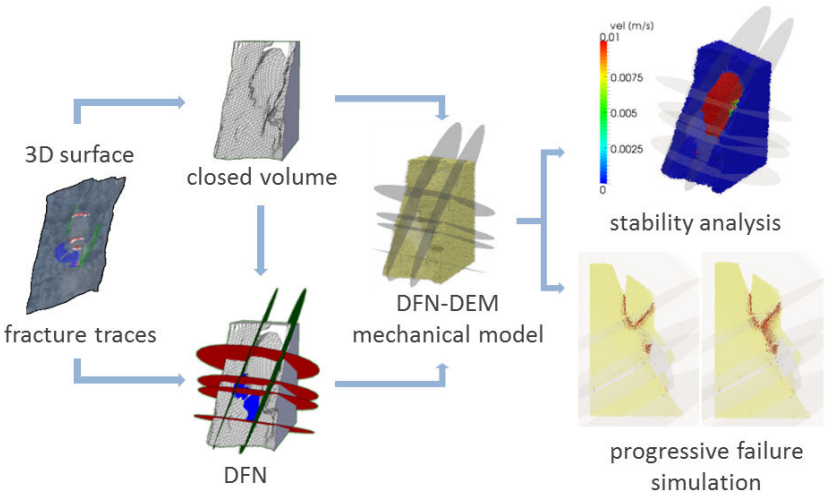

Figure 1.14: Overview of the DFN-DEM approach

CHAPTER 2

Rock slope stability analysis using photogrammetric data and DFN-DEM modelling

Structural and mechanical analyses of rock mass are key components for rock slope stability assessment. The complementary use of photogrammetric techniques and numerical models coupling Discrete Fracture Networks (DFN) with the Discrete Element Method (DEM) provides a methodology that can be applied to assess the mechanical behaviour of realistic three-dimensional (3D) configurations for which fracture persistence cannot be assumed. A real case has been studied to show the complete methodology from the acquisition of the photogrammetric data to the numerical modelling of the potential progressive failure process occurring in the rock mass. Using a 3D mapping system and its associated structural mapping tool Sirovision, the topography and the discontinuity set of an unstable rock block located in a limestone layer of the Mount Néron, located in the French Alps, were imported into a DEM code specially enhanced for the modelling of pre-fractured rock masses. A stability analysis has been carried out, emphasizing the contribution of rock bridge failure through a mixed shear-tensile failure process to the generation of new failure surfaces. This approach addresses limitations in methodologies using only shear strength reduction method. It is believed that the proposed methodology can strengthen the basis for a more comprehensive stability analysis of complex fractured rock slopes.

2.1 Introduction

Rock slope stability is commonly analysed using limit equilibrium techniques or limit analysis associated with numerical methods, but a minimum understanding of the mechanical processes involved is needed to successfully apply these classical methodologies (Read, 2007). For instance, the failure processes can reach high levels of complexity in fractured rock masses because they combine the mechanical properties of the rock blocks, the geometry and properties of the structural defects and the progressive failure of the rock matrix in the presence of non-persistent discontinuities (Einstein et al. (1983); Stead et al. (2006)).

As a minimum requirement, the geotechnical model should include the geological model, *i.e.* rock type and structural description, the rock mass model including the mechanical properties of both the rock matrix and the fracture network and the hydrogeological model, characterising water flow in the rock mass. However, setting up such a model requires a detailed and reliable description of the rock mass for which the internal characteristics are often hidden or can only be characterised stochastically (Elmouttie et al., 2014).

Among these difficulties, the definition of a Discrete Fracture Network (DFN) which represents appropriately the spatial distribution and geometry of the discontinuities in the structural model is of major importance for accurate understanding and prediction of rock mass deformation and slope failure mechanisms (Brideau et al., 2009). This is particularly important when the failure involves sliding along major structures and/or fracturing of the rock bridges present between these structures (Read et al., 2009).

The geometry and structural properties of inaccessible rock slopes can be estimated using remote sensing techniques when the rock outcrops are available provided that the vegetation cover is limited and that the meteorological conditions are favourable. Under such conditions, terrestrial photogrammetry provides valuable information sufficiently precise to construct realistic digitised surfaces (Poropat (2006); Sturzenegger et al. (2011)). From the structural analysis of these digitised and georeferenced surfaces, a first assessment of the DFN can be defined from the mapping of discontinuities on the slope surface. If possible, this DFN can then be better constrained by well logging data (*e.g.* Diavik northwest wall case, (Beale et al., 2014). The digitised parametric surface and its associated DFN can then be imported into numerical software packages to set up rock mass mechanical model for stability analysis (Firpo et al. (2011); Sturzenegger and Stead (2012)).

Due to limitations in computing resources, most of the current 3D numerical models are limited to handling no more than two orders of magnitude in structure size distribution (Harthong et al., 2012). This actually limits the amount of geometrical information which can be retained in the mechanical model. Working for example at a 10 meter scale, the

DFN that can be implemented into the model will be composed of structures ranging from 10-cm to 10-m (Esmaieli et al., 2010). Further, for similar reasons, the analysis is also limited to relatively few DFN realisations, a limitation that can be significant for studies of structural models based on stochastic representations (Elmouttie et al., 2014). These limitations should therefore be kept in mind with respect to the modelling strategy and the interpretation of the results.

One key requirement for the successful integration of the geological model within the mechanical model is for field data to be sufficiently accurate and pre-processed for importation. In this study, Sirovision software (Sirovision, 2010) was chosen to map rock slope surfaces and structures from stereo photographs, motivated by the fact that the digitised surfaces resulting from the numerical processing can be conveniently imported into a mechanical model which represents explicitly these features. With regard to this consideration, the YADE Open DEM platform was selected to simulate the mechanical response of the rock mass (Scholtès et al. (2011); Scholtès and Donzé (2012); Harthong et al. (2012)).

In this section, a strategy that combines Sirovision and YADE Open DEM is presented and applied, for the stability analysis of a rock slope. First, it will be shown that even for a large camera to rock slope distance range (tested at about one kilometre), the accuracy of the collected data, although considering the large distance limitation, is sufficient to assess the role of the structures on the stability of this particular jointed rock slope. This process will be illustrated through the study of a hanging rock block of about 3,000 m^3 located on the Mount Néron eastern slope, located in the French Alps. Then, for validation, the orientations of the structures identified by the photogrammetric means will be compared to the orientations obtained by the use of a compass on the field.

Since the authorities decided to blast this block to avoid an uncontrolled rockfall event, post-blasting photogrammetric data acquisition could be performed. By comparing with aerial LIDAR data, it was then possible to assess the accuracy of the data acquired using terrestrial photogrammetry in terms of blasted volume. Besides this comparison, the post-blasting analysis of the outcrop helped us to set up a refined DFN where non-persistent structures could be taken into account. This DFN has then been used in the DFN-DEM model to simulate how the instability could occur if the blasting was not carried out. Using a Tensile and Shear Strength Reduction (TSSR) technique, it will be shown that a combination of rock bridge failure, sliding and toppling modes were involved in the destabilisation process, emphasizing the fact that the use of a classical stability factor can be strongly limited for this kind of configuration.

2.2 Data acquisition

Mount Néron is located 5 km NW of Grenoble (Isère, France), at the southern end of the Chartreuse carbonate massif (Figure 2.1, on the left). The top of its eastern slope (between 1,150 and 1,300 m in altitude) is composed by a 150-m high, near-vertical cliff made up of lower-Urgonian massive limestone (Figure 1, on the right). Below the cliff, the 40° inclined slope (1,150 m – 600 m) is covered with scree deposits overlying marly limestones, while the lower part of the slope shows gentle slope with marl outcrops (Gidon and Arnaud, 1978). In summer 2003, the SAGE consulting company detected a 4,700 m^3 unstable rock column in the limestone cliff, between 1,210 m and 1,260 m in altitude (Fabre et al., 2013) (Figure 2.2).

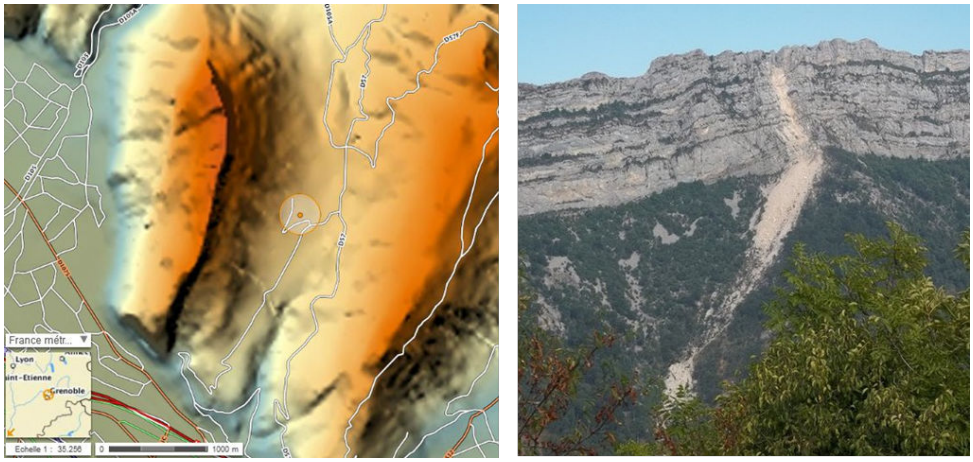

Figure 2.1: On the left, the situation map (Geoportail map). The topography is shown by the colour scale, and the major roads are marked with white thick lines. The orange circle points out the bottom part of the rockfall propagation zone for the triggered event. On the right, a picture of Mount Néron was taken from the east after the triggered event, with Urgonian limestone (UL, rock slope) and marly limestone (ML, vegetal slope). The rockfall and the scree deposit zones are part of the long bright scar on the slope (*credit: Jérôme Creton*)

A rockfall occurred at 02:30 Coordinated Universal Time (UTC) on 14 August 2011. The 2,000 m^3 lower part of the column (shown with the dashed blue line on Figure 2.2) detached from the cliff, free fell about 100 m below and propagated down the slope. The 2,700 m^3 upper compartment of the rock column (circled with the red dashed line in Figure 2.2) remained attached to the cliff. Because of its apparent low residual stability, the decision was taken to blast it. The blasting, operated by Hydrokarst company, occurred on 13 December 2011. An extensive study about this artificially triggered rockfall event involving geophysical measurements has been recently published in Bottelin et al. (2014). The following sections describe the proposed method for data acquisition and integration

for numerical modelling.

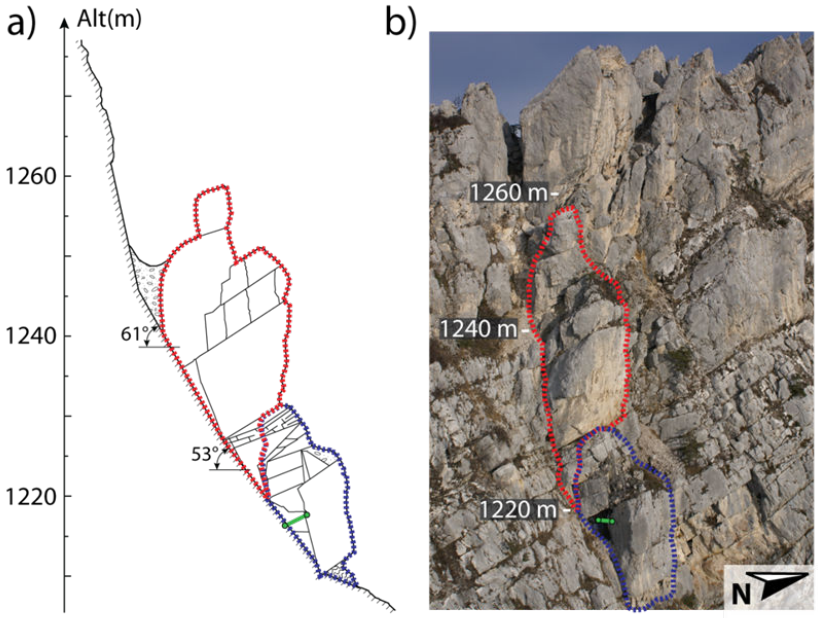

Figure 2.2: a) 2D schematic cross-section of the unstable column. The cliff is indicated with the hatched line, and discontinuities are shown with black continuous lines. b) Picture of the unstable rock column before the two rockfalls was taken from the south-east. Altitude is given with the white marks. For (a) and (b), blue and red dashed lines delineate the natural and blasted compartments, respectively. From Bottelin et al. (2014).

2.2.1 Georeferencing and overlapping 3D surfaces

Digital outcrop model creation and 3D mapping were done using Sirovision, a software package created specifically for geological and geotechnical mapping (Sirovision, 2010). This software uses overlapping stereo pairs of digital photographs and survey information to create 3D digital models that are scaled and oriented within a specified coordinate system (Gates et al., 2012). The software consists of two components, one for 3D model creation and one for rock mass discontinuity mapping, visualisation and analysis (Haneberg, 2008).

The equipment used in the present study consists in a Canon EOS 5D Mark II camera with a 21.1 megapixels resolution and a lens of 135 mm fixed on a tripod. Based on the depth of field required to image the slope as well as the prevailing lighting conditions, a maximum focal ratio of *f/8* was kept for all shots. Two photographs of the same slope were taken at a distance close to 1,500 m. The success of using this technique to build 3D

models of the rock slope depends on good field procedure, which includes the adoption of a recommended ratio between the baseline between camera positions and the distance to the face (typically ranging from 1:10 to 1:6). Given the equipment used in this study, with distance to the target of 1,500 m and baseline of 1/7 (Poropat, 2006), the theoretical resolution (*i.e.* ground pixel size) of the 3D images equates to 50 mm. The planimetric accuracy expected is 25 mm (considered as 0.5 of the ground pixel size (Birch, 2006), and the corresponding depth accuracy is equal to 100 mm. However, this configuration assumes that an appropriately calibrated imaging system is used and does not account for georeferencing accuracy or particular field conditions (*e.g.* inaccuracies in the image matching process caused by lighting, occlusion, unfavourable surface orientations and atmospheric distortions).

Additionally, the TruePulse 200B laser range finder manufactured by Laser Technology Inc. (with a stated maximum error ±30 cm at 1,000 m but our trials indicated the error was around 1 m) was used to obtain the horizontal distance from the camera, height, azimuth and inclination of the control points selected on the rock face. Using a Getac PS535F GPS device, with one-metre precision, the positions of each camera station were also acquired. The surveying process resulted in a total of two camera positions and three well-identified points (see Figure 2.3). Three points were enough to georeference the 3D image, considering that the optimum geometry can be achieved if the points form an approximate equilateral triangle and are well distributed (Sirovision, 2010).

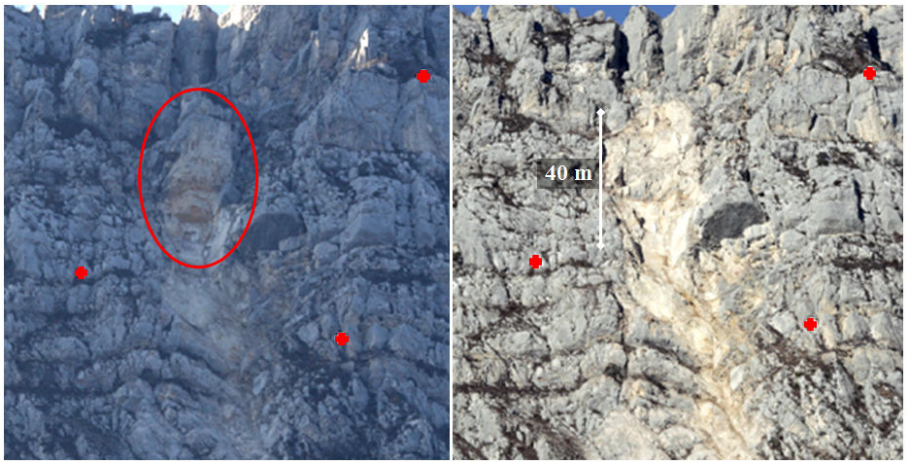

Figure 2.3: Unstable rock block before the blast (left); after the blast (right). Red crosses correspond to the control points used for georeferencing

The final model precision was more controlled by the accuracy of the georeferencing procedure than by the predicted photogrammetric precision stated above. Considering the precision of the laser range finder and the GPS precision using for the surveying process, the resulting spatial accuracy of the 3D georeferenced image from transformation error assessment done by Sirovision was 2-m. Given the scale of the analysis performed in this

work, this accuracy was deemed tolerable both in terms of location and orientation of the structures being mapped off the 3D model. The following section presents assessments of this assumption.

2.2.2 Identification and validation of sets of discontinuities and their orientations

Prior to this photogrammetric investigation, a limited field mapping exercise of the cliff was done by the SAGE consulting company, using a compass-clinometer. It revealed that the back of the unstable column was bounded by a potential sliding plane (F1) striking N10°, 53-61°SE, while the bedding (S0) strikes N15° and dips 45°W inwards (Table 2.1). These discontinuities divide the column in many compartments, the largest one reaches out to 400 m^3. In order to challenge the acquisition capability of Sirovision system (Sirovision, 2010), the structural features of the cliff were extracted from the 3D digital image for the same zone using photogrammetric data acquired before the triggered rockfall. The planes to process for discontinuity orientation characterisation were both, automatically (Figure 2.4a) and manually selected (Figure 2.5a), showing that the results obtained manually are representative of the automatic set. The automatic characterisation process is based on selection criteria such as a coherent area threshold. The poles of three identified sets of discontinuities in the rock block zone are plotted on a stereographic diagram (Figure 2.4b and 2.5b), using Wulff lower hemisphere projection. The average pole (square marker) and average plane (circle line) for each set are drawn in Figure 2.5b (manually detected planes) and listed in Table 2.1. The bedding (S0, in green) strikes between N29°W and N55°E with 16°W to 58°W inward dipping (mean: N06°E, 39°W), while the two fracture sets F1 (blue) and F2 (red) are oriented between N62°E and N26°W, with dip angle oscilating between 38°SE to 90°E (mean: N11°E, 68°SE) and N04°E to N85°W with dip of 43°S to 88°S (mean: N88°E, 69°S), respectively.

As presented in Table 2.1, photogrammetric and field measurements are in good agreement. However, the fracture set F3 observed in field was difficult to find by the photogrammetric analysis since it did not generate sufficiently large facets at the surface of the 3D image. Nonetheless, the photogrammetric technique showed its ability for retrieving the main discontinuity pattern, even from such a remote viewpoint at over 1-km range.

2.2.3 Post-blast volumetric assessment

The potential of the photogrammetric technique used here was verified also through a volumetric evaluation. The volume difference and the displacement variation in the selected area were computed by superposition of the 3D surfaces collected before (dark grey) and after (light grey) the blasting as represented in Figure 2.6.

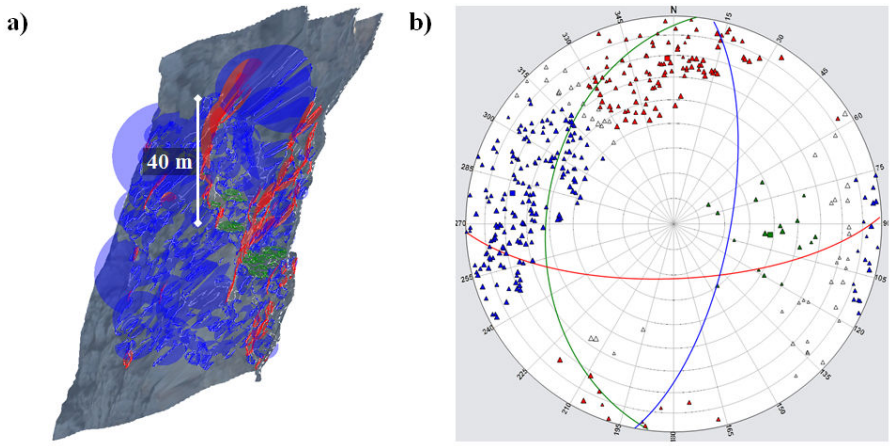

Figure 2.4: a) 3D picture of the cliff before the triggered rockfall. The planes automatically detected for discontinuity orientation characterisation are shown with coloured discs. The mean cliff plane (in blue) strikes N 11 E. b) Stereographic diagram of (a) using Wulff lower hemisphere projection. The pole of each facet is shown by a triangle, whereas the average pole is pointed out with a square marker. The average plane is drawn with a circle line. The bedding (S0, in green) as well as F1 (blue) and F2 (red) fracture sets are retrieved

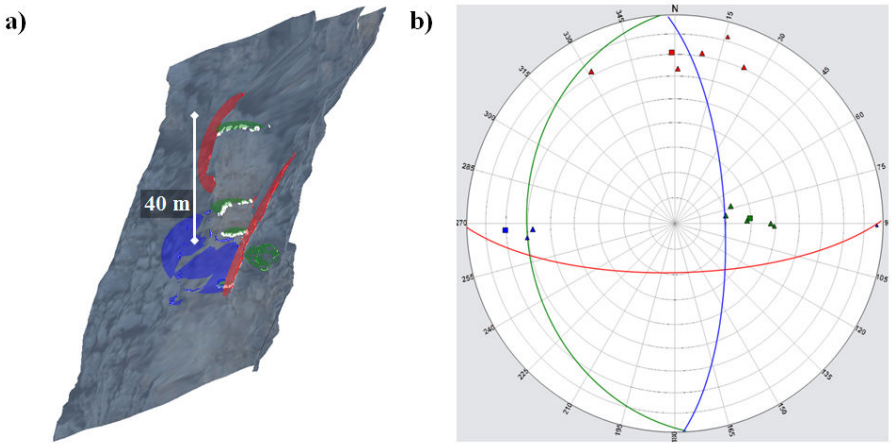

Figure 2.5: a) 3D picture of the cliff before the triggered rockfall. The planes surrounding the unstable mass are manually selected for discontinuity orientation characterisation, they are shown with coloured discs. b) Stereographic diagram of (a) using Wulff lower hemisphere projection. The pole of each facet is shown by a triangle, whereas the average pole is pointed out with a square marker. The average plane is drawn with a circle line

The blasted volume was estimated at 2,380 $\pm$200 m^3, which is consistent with the volumes estimated *in situ* by the SAGE consulting company (2,700 m^3) and determined from LIDAR data (2,570 m^3) (see Bottelin et al. (2014), for more details). This latter case

set	field analysis		stereoscopic analysis	
S0	N 15°	45° W	N 06° E	39° W
F1	N 10°	53°-61° SE	N 11° E	68° SE
F2	N 70°	80°-90° S	N 88° E	69° S
F3	N 125°	70°-90° N	-	-
Slope orientation	-	-	N 20° E	67° SE

Table 2.1: Mean discontinuity orientation revealed by field and stereoscopic stereographic analyses

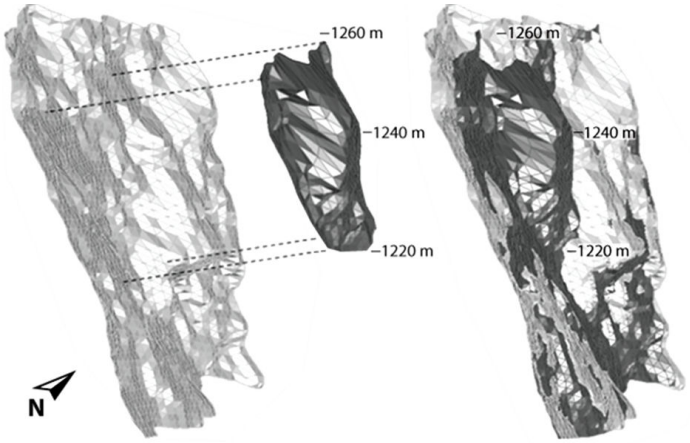

Figure 2.6: On the left, 3D images collected before (dark grey) and after (light grey) the blasting event. On the right, Sirovision model with superimposition of the 3D images for volume determination (From Bottelin et al. (2014))

is more consistent with the volume estimated using our approach; however, the aerial LIDAR provided a more complete topography than the photogrammetric technique because it could have access to the backside of the hanging block (see Figure 2.2), which was not visible from the places where the pictures were taken. The ground-based photogrammetric technique, while being much less expensive than the aerial LIDAR approach, is more susceptible to occlusion.

2.2.4 Post-blasting back face characterisation and potential presence of rock bridges

The presence of rock bridges (patches of intact material connecting the different compartments in calcareous rocks) was assumed based on the observation and identification of scars left on the surface after the triggered rockfall. The 3D image generated after the blasting was used to identify colour differences on the surface, given that the fresh

fracture surfaces usually contrast with the rest of the scar (Frayssines and Hantz, 2009). This observation suggests that rock bridges could be present at the rear of the blasted block in zone 3 (Figure 2.7), between two smooth and open fracture planes identified for the lower one by zone 5 and the upper one by zones 1 and 2. This characterisation is essential as the presence of intact rock bridges was found to be the critical factor for compartments prone-to-falling in calcareous rocks (Frayssines and Hantz, 2009). Indeed, by connecting the blocks, rock bridges can stabilise the rock mass. Rock bridges failure may thus result in promoting new potential failure surfaces involving both sliding along pre-existing discontinuities and fracturing of intact rock (Einstein et al. (1983); Stead et al. (2006)). A comprehensive mechanical model should then be set up, taking into account non-persistent fractures associated with possible rock bridges at the back of the unstable block.

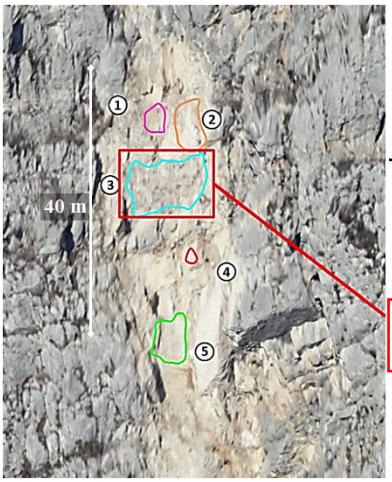

No. Plane	Strike (°)	Dip (°)
1	N 55	60 SE
2	N 41	65 SE
3	N 28	63 SE
4	N 75	68 S
5	N 8	56 SE

Figure 2.7: Potential rock bridge identified based on contrast in colours

2.3 Rock mass model

Since the breakage of rock bridges can play a major role in the rock mass destabilisation, a model able to simulate the progressive failure of intact rock needs to be used. To that matter, the YADE Open DEM platform (Kozicki and Donzé (2008); Kozicki and Donzé (2009); Šmilauer et al. (2010)) was chosen for the analysis.

2.3.1 Discrete Element Method

As in classical particle models, the intact rock is represented by a set of discrete elements (DE) glued together by cohesive bonds that can break either by tension or shear failure to

simulate the progressive development of fracturing induced by an external loading (Donzé and Magnier, 1995). The bond behaviour is defined according to a cohesive frictional contact law that needs preliminary calibration to simulate the desired material, fractured Urgonian limestone in the present case. Recent works have shown that it was possible to accurately describe intact rock behaviour through a pertinent choice of parameters and a rigorous calibration procedure (Scholtès and Donzé, 2013). In particular, by allowing contacts to be created between near-neighbour DE, it is possible to reduce the limitations of spherical DEM and to implicitly take into account the degree of interlocking associated with the micro-structural property of the considered rock type (Scholtès and Donzé, 2013). Ergo it is possible to reproduce high values of the uniaxial compressive strength (UCS) to tensile strength (TS) ratio characteristic of brittle rocks, as well as the non-linear nature of low porous rock failure envelopes as will be shown later (Figure 2.2).

Moreover, the model can reproduce an essential component of brittle rock failure, that is, cohesion weakening and frictional strengthening as a function of rock damage or plastic strain which are mechanisms of primary importance in progressive failure processes.

2.3.2 Discrete Fracture Network

The DFN is modelled as a set of circular surfaces whose orientations were selected according to the structural analysis (Figure 2.5a), each surface representing a pre-existing fracture in the rock mass. The DFN simplification (Figure 2.8) implies the assumption of bedding planes (S0) being persistent through the simulation volume based on the fact that the unstable rock block is likely divided in many compartments by those planes, as observed in Figure 2.2. In the same manner, the set of discontinuities F2 has been considered persistent, in order to constrain the stability of the rock block only to the existence of the rock bridge that has been adjusted depending on the size of the plane F1, which was assumed to be non-persistent. The planar assumption is commonly used in rock engineering (Zhang and Einstein, 2000) and has the advantage of greatly simplifying the modelling and the analyses. This assumption is tolerable for the current analysis given the acquired structural mappings.

The presence of the potential rock bridge is reproduced by keeping an intact zone within the model, just behind the hanging block (see Figure 2.9). To take into account the effect of the discontinuities in the DEM, the DFN is overlaid into the DE packing for the identification phase.

2.3.3 Model set-up

Once the numerical topography was acquired, the 3D digitised and meshed surface was processed by a CAD software package to define the studied rock mass as a closed (man-

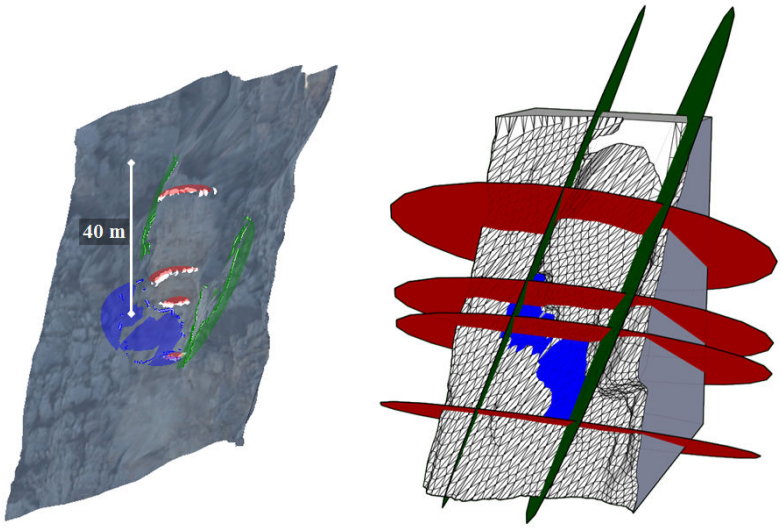

Figure 2.8: On the left, the discontinuities involved in the studied rock block and identified from the structural analysis. On the right, the associated discrete fracture model which has been used for the mechanical simulations

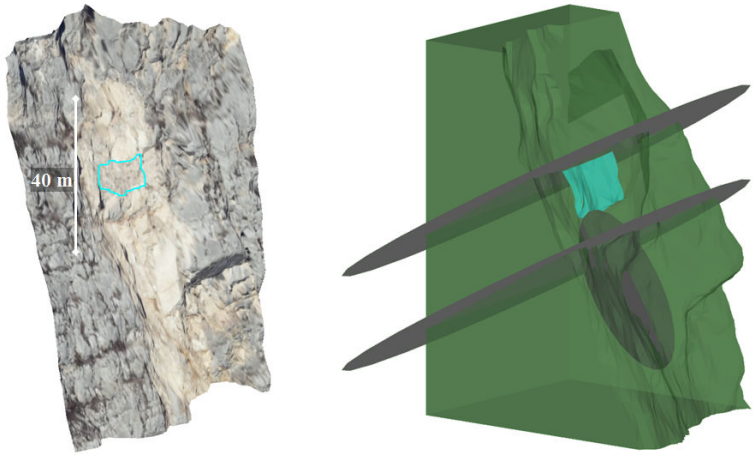

Figure 2.9: On the left, the blue line indicates the possible rock bridge area identified on the surface after the blast using Sirovision. On the right, the corresponding rock bridge zone (coloured in blue) in the numerical model

ifold) volume (Figure 2.10, left). The initial 3D surface had to be modified in order to represent the notch observed behind the unstable mass which could not be retrieved from the 3D image due to the occlusion effects. The mesh was then edited and cut following the 2D schematic cross section presented by SAGE (see Figure 2.10, right), considering that the notch cannot be neglected in the stability analysis of the rock block. One can note that the match is not perfect between the schematic cross section and the mesh, due to the wide angle and the large distance from which the 2D images were taken. The

consequence is that the size of the simulated rock block is most likely slightly smaller than its actual size on field.

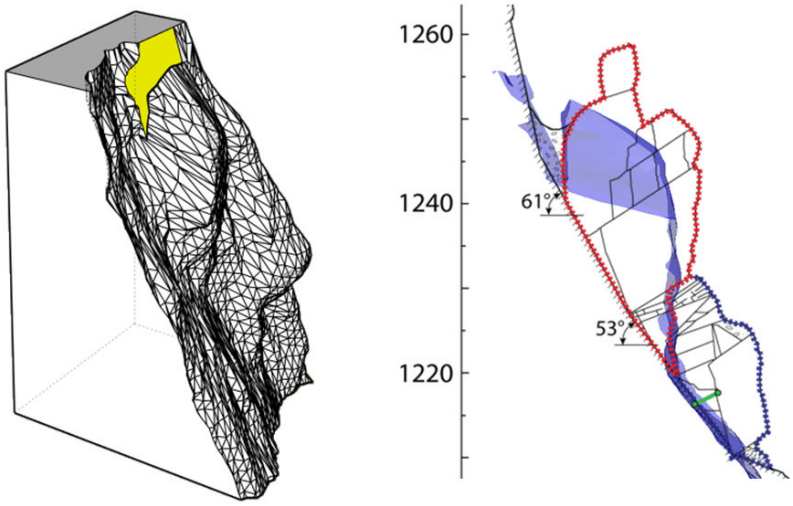

Figure 2.10: On the left, the closed volume modified to represent the notch (in yellow) behind the unstable mass. On the right, a vertical cut of the 3D surface (in blue), including the discrete fracture model, is superimposed to the schematic 2D cross-section provided by the SAGE company

The numerical model is built up according to the following procedure:

- First, the DE are packed into the closed mesh using a generation technique where a small dense and isotropic brick is first created by dynamic growth of an initial DE cloud and then periodically cloned to fill the entire volume to model (Figure 2.11). Care has to be taken here to generate polydisperse packings in order to avoid anisotropic effects associated with regular packings (Belheine et al., 2009). The size of the DE also has to be chosen to ensure a sufficient discretisation of the inter-space between the pre-existing fractures, keeping in mind; however, the associated computational cost as running simulations with more than 10^6 DE can be problematic. This requirement can therefore necessitate adjustments after preliminary simulation trials. YADE's formulation ensures size independence of the mechanical response for the intact part of the medium. Nonetheless, discrepancies can emerge from the presence of discontinuities when not enough DE describe the rock bridge, as discussed in Harthong et al. (2012).

- Defining the intact part of the medium, the DE forming the assembly are then bonded together through cohesive frictional interactions whose properties have to be identified. Model parameters were calibrated here to match the behaviour of intact Urgonian limestone as described in Frayssines and Hantz (2009). In order to take

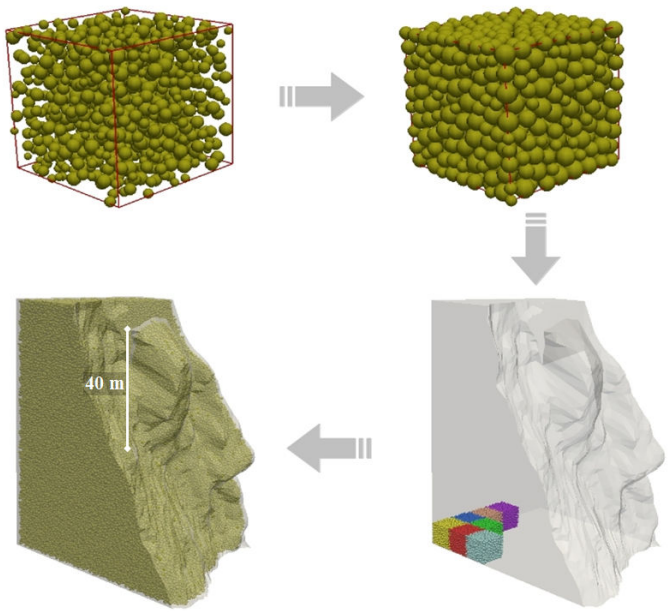

Figure 2.11: Packing procedure for model generation in YADE Open DEM

into account a scale effect on strength, we chose to apply a reduction factor of 0.1 on the mechanical properties measured in the laboratory following the recommendation of Frayssines and Hantz (2009). The reader is referred to Scholtès and Donzé (2013) for a detailed description of the contact laws and calibration procedure. Stress-strain curves and failure envelopes obtained from tensile and compression test simulations performed on the calibrated model are presented in Figure 2.12.

- Every pair of DE separated by a discontinuity plane need to be identified, and their interaction is subjected to a dedicated numerical treatment which can be related to the work initiated by Cundall *et al.* (Cundall et al. (2008); Mas-Ivars et al. (2011)) for the development of the synthetic rock mass. This specifically adapted contact treatment is based on the identification and reorientation of each discrete interaction that intersects the geometrical plane representing the pre-existing fractures (see Scholtès and Donzé (2012) for details). The discontinuity surfaces are thus discretised into sets of contacts sharing the same pre-defined orientation and micro-mechanical properties. This special feature ensures that the behaviour of the surface is independent of the inherent roughness produced by the arrangement of the discrete elements at the interface. As for the intact part of the discrete model, the behaviour of these surfaces has to be defined through a preliminary calibration of the contacts making up the interface. As a complement to the contact law used for the intact par of the model, a dilation component can be added to the force normal to the discontinuity surface, in order to simulate the aperture of the joint

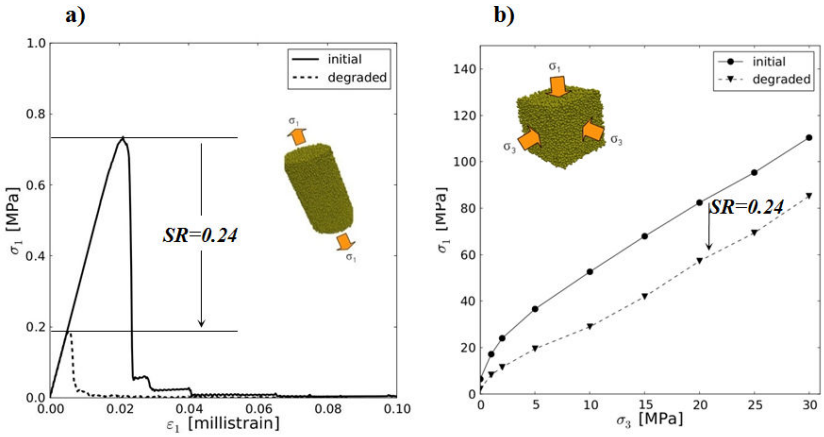

Figure 2.12: Behaviour of the DEM model in its initial and its degraded configurations. a) stress-strain curve obtained from direct tensile test simulations, b) failure envelopes obtained from triaxial compressive test simulations. SR refers to the strength reduction factor applied at the interaction scale during the stability analysis

usually observed with shearing (Scholtès and Donzé, 2012). The micro-mechanical properties of the interactions making up the discontinuities were calibrated here based on the properties obtained from laboratory test performed on Urgonian limestone joints by Frayssines and Hantz (2009). The failure envelope obtained from direct shear test simulations performed on the calibrated joint model is presented in Figure 2.13. Table 2.2 summarises the macroscopic properties of the rock mass model.

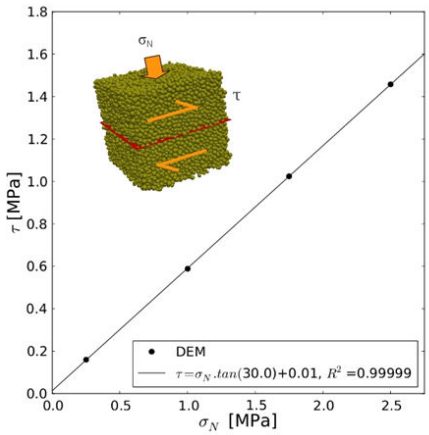

Figure 2.13: Failure envelope obtained from direct shear test simulations performed on the calibrated joint model

parameter	intact rock	discontinuities
Young's modulus E (GPa)	35	-
Poisson's ratio ν(-)	0.3	-
Tensile strength TS (MPa)	0.75	0
Compressive strength UCS (MPa)	7	-
Cohesion c (MPa)	1.3	0
Friction angle (°)	33	30

Table 2.2: Mechanical properties of the rock mass model

2.3.4 Boundary conditions

The model is then submitted to gravity loading. In order to mimic the *in situ* stress field, the displacements of the DE defining the boundaries with the surrounding rock mass were avoided in the direction perpendicular to the model surface. During the stress initialisation, discontinuities are assigned high values of cohesion so as to avoid failure or block displacements triggered by inertial effects. Even though artificial, this procedure ensures that the stress field is pre-constrained by the DFN in accordance with the *in situ* anisotropic stress conditions. Once the model has stabilised under gravity, discontinuity properties are assigned to their *in situ* values.

2.4 Stability analysis using a Tensile and Shear Strength Reduction method

2.4.1 Strength reduction method

In the presence of rock bridges, the slope model can eventually stand in a stable configuration after the stress initialisation. In this case, a strength reduction method is then used in order to promote failure. This strength reduction (SR) method involves the progressive and simultaneous decrease in the interparticle bond tensile strength and cohesion. Classically, only Shear Strength Reduction (SSR) technique is used in numerical models, *e.g.* Hammah et al. (2005). This makes sense as long as shear fracture mode is predominant.

In the present overhanging configuration, we can expect a mixed (shear and tensile) mode of failure, and therefore, a Tensile and Shear Strength Reduction (TSSR) method was chosen to promote both local shear and tensile cracks. Defined at the particle scale, the formation of the micro-cracks will contribute to decrease progressively the macroscopic tensile and compressive strengths of the medium. This method presents the advantage

of preserving the same shape of the failure envelope during the weakening process of the rock mass (Figure 2.12b).

In comparison with the Shear Strength Reduction Factor (SRF) used by Francioni et al. (2014), where the shear strength was iteratively decreased only in the joint properties until the slope failed to simulate pure structurally controlled failure, the TSSR method used here involves the possibility of a failure mechanism to occur within the entire rock mass so as to lead to the rock bridges failure from the propagation and coalescence of pre-existing fractures.

This strength reduction method can be used to calculate a relative "Factor-of-Stability" (FoS), defined as follows:

$$FoS = \frac{1}{SR} = \frac{initial\ strength}{failure\ strength} \tag{2.1}$$

The ratio indicates how much weaker the rock is at failure compared to its initial strength. Usually, a Factor-of-Safety is used to assess the stability of a rock slope in the context of jointed Mohr-Coulomb materials. Typically, the shear strength of the joint is progressively reduced to bring the slope to a state of limit equilibrium characterised by failure along pre-existing fracture planes. However, in the presence of rock bridges, the state of limit equilibrium will never be reached as long as the intact rock matrix does not break. The critical factor is therefore the strength of the rock matrix rather than the strength of the pre-existing discontinuities. This is why we make reference to a "Factor-of-Stability" rather than a "Factor-of-Safety" to quantify how much the strength of the rock matrix needs to be reduced to reach the global instability of the structure.

2.4.2 Application

The strength reduction is applied at the scale of the bonds making up the cohesion of the rock matrix while properties of the rock joints stay unchanged. The material strength is thus gradually reduced by iteratively applying a SR factor equal to 0.75 to the previous strength values, namely the bond tensile and shear strengths. Each time this SR is performed, the system is allowed to reach equilibrium before a new SR is applied. Ultimately, failure occurs when the material is no longer able to sustain the loading. Following this iterative process, bonds break in zones where the material strength is overcome by the load, leading the system or at least part of it, to an unstable regime (*i.e.* independent groups of particles detach from the slope and collapse). A possible way to follow the progressive failure of the model is to track the increasing amount of broken bonds, *i.e.* cracks, as the strength decreases (Figure 2.14). As the TSSR factor reaches a value of 0.24, it can be noted that the amount of cracks increases dramatically. This sudden increase in damage is associated with a finite displacement of the hanging

block (see Figure 2.15). The velocity of the upper part of the block increases as well, showing an irreversible destabilisation of the block. This configuration corresponds to the definition of the factor of safety equal to one. Considering an initial value of 0.75 MPa for the global tensile strength of the rock matrix and the value at failure of 0.18 MPa, the Factor-of-Stability is thus equal to four (FoS = 4, *i.e.* the initial strength has been reduced by 75%, or the rock is 4 times weaker). Note that the obtained value of the Factor-of-Stability depends on the initial properties of both rock matrix and joints. The simulations were set up with a reasonable friction value for the discontinuities (30°). For different friction values, the resulting value of the "Factor of Stability" would have been only slightly different, because the joints involved in the destabilisation process of this configuration are the almost vertical ones. Thus, it is the rock bridges resulting from the non-persistence of the joints which play a crucial role.

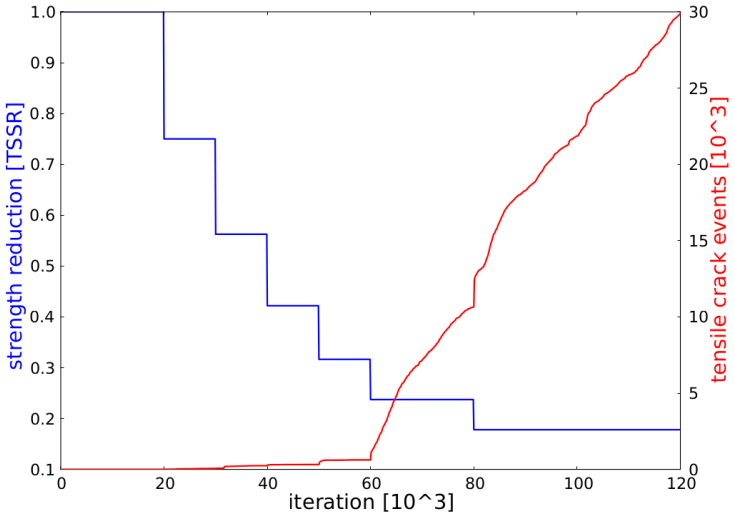

Figure 2.14: Decrease in the strength as a function of the iteration numbers (blue curve). The red curve represents the cumulative amount of cracks

2.4.3 Analysis of the failure process of the rock

As presented in Figure 2.16 where the spatial distribution of micro-cracks is plotted at several times of the simulation, it is possible to follow the progressive failure of the slope in the model. Failure initiates from two distinct zones in the rock mass, one of them located at the upper tip of the vertical discontinuity and the other at the intersection of this discontinuity and a bedding plane discontinuity.

Figure 2.17 illustrates the velocity field facilitating the identification of unstable rock blocks split into three distinct parts, all of them falling progressively. As a result of this mechanism, the lower block located below the third bedding plane (from bottom to top) is

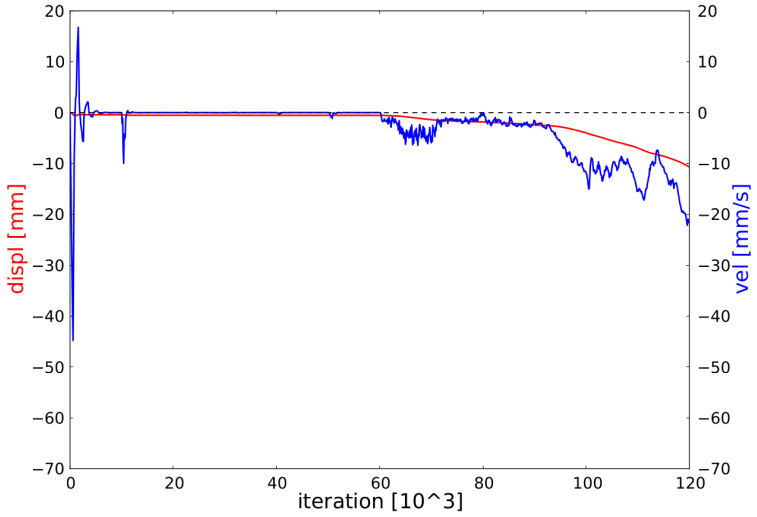

Figure 2.15: Vertical displacement of the top zone of the hanging block as a function of the iteration numbers (red curve). The blue curve represents its velocity

first separated from the face and slides as shown in the upper left and right of Figure 2.18. Then, the block located between the third and fourth bedding planes separates from the rock mass and collapses in a combination of toppling and sliding denoted in the lower left in Figure 2.18, where the direction of the velocity vectors indicates the tilt around Y-axis. The remaining upper block moves also toward the front around its base (see lower right in Figure 2.18). The toppling process observed here was confirmed as cracking events mainly occurred in tensile mode.

Since the rockfall was artificially triggered, this critical state could not be observed on field. However, the results obtained applying the proposed methodology show that the block was still in a stable configuration unless SR had been induced.

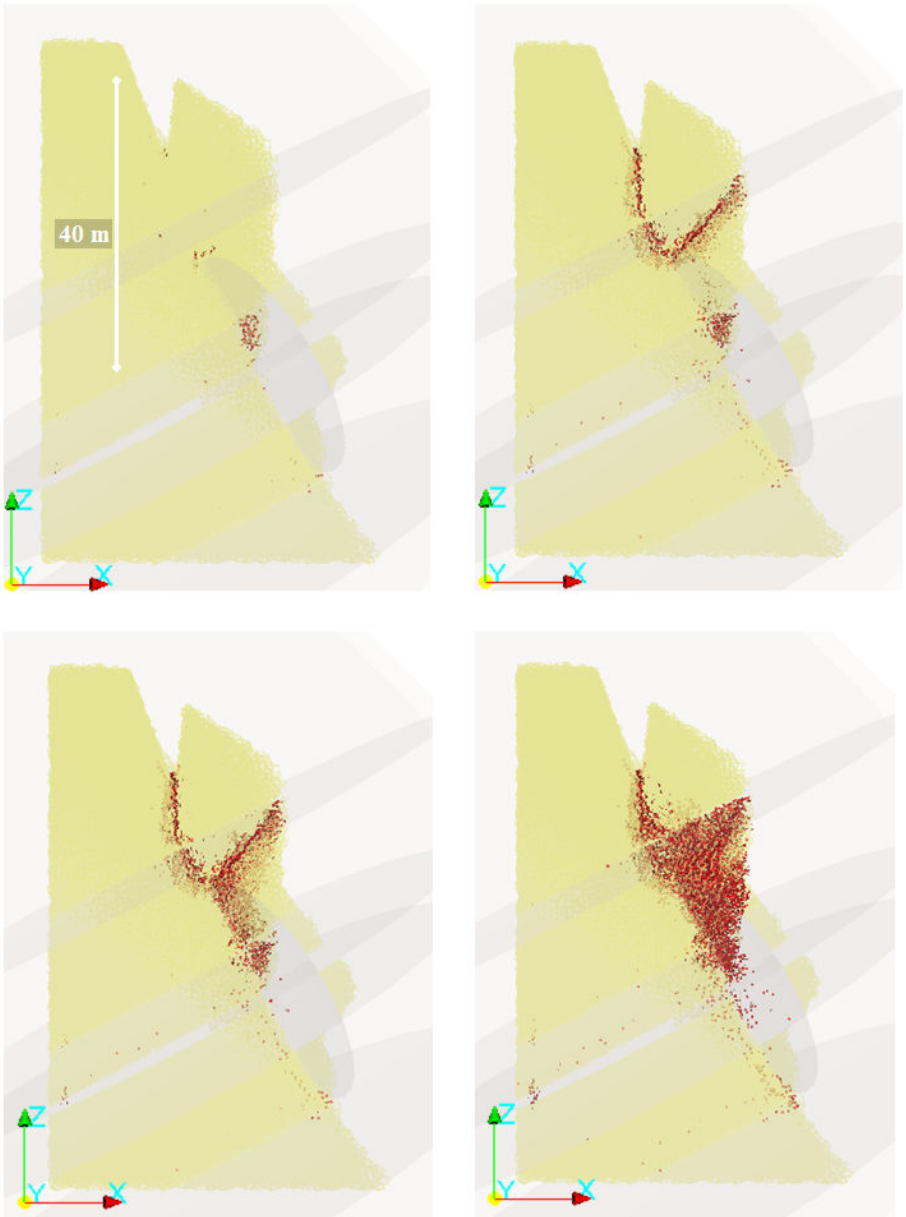

Figure 2.16: Vertical cut of the model. The set of discrete elements is in yellow. The discrete fractures are in grey and the cracks are in red. The upper left figure is plotted after 60,000 iterations, the upper right after 70,000 iterations, the lower left, after 80,000 iterations and the lower right after 120,000 iterations

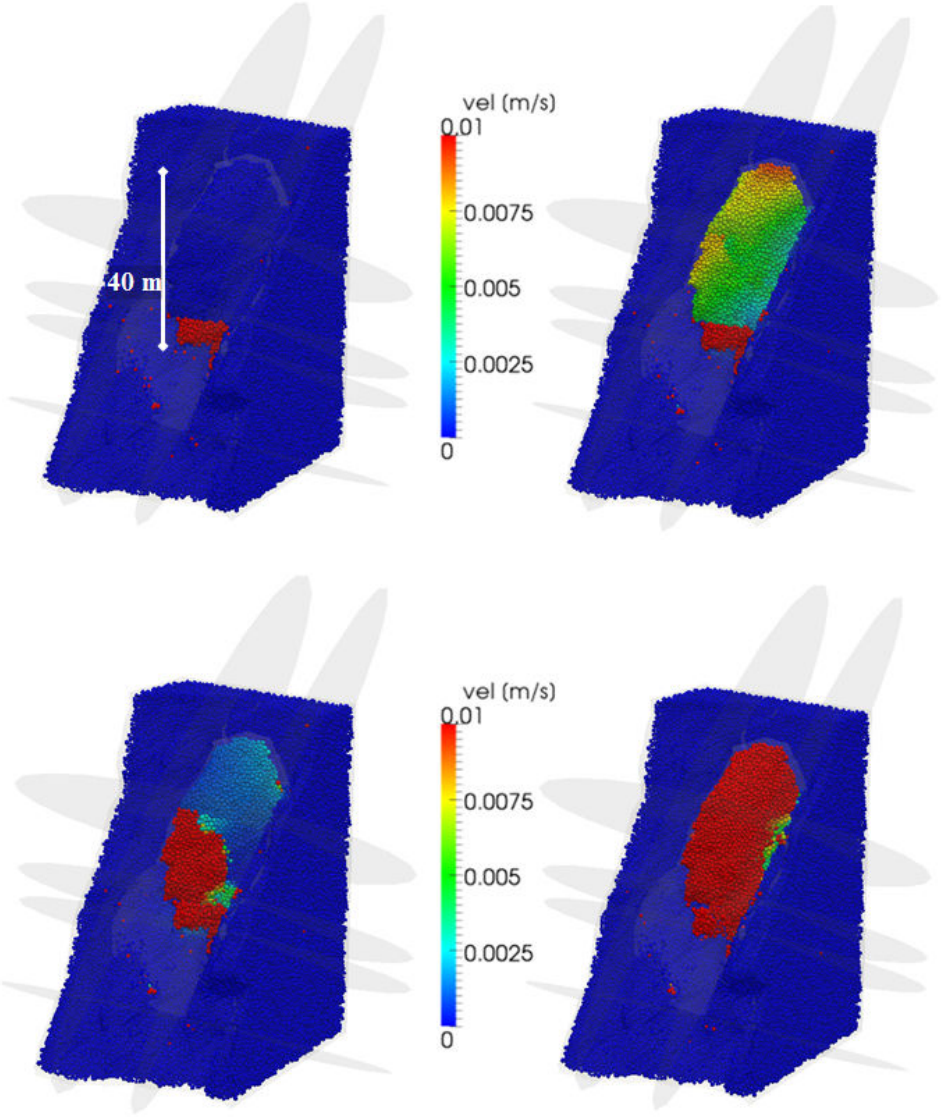

Figure 2.17: 3D view of the velocity field. The upper left figure is plotted after 60,000 iterations, the upper right after 70,000 iterations, the lower left, after 80,000 iterations and the lower right after 120,000 iterations

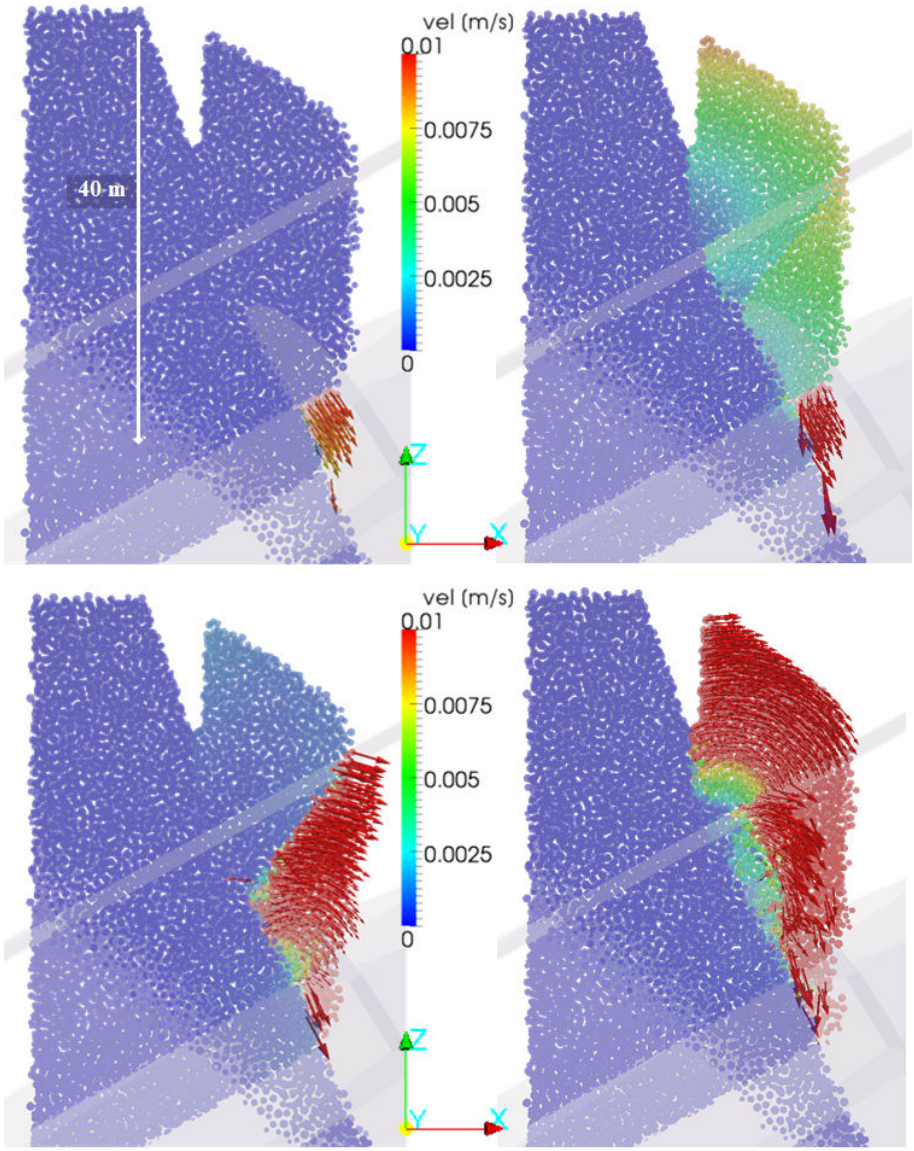

Figure 2.18: Vertical cut of the velocity field and direction vectors indicating the combination between sliding and toppling process. The upper left figure is plotted after 60,000 iterations, the upper right after 70,000 iterations, the lower left, after 80,000 iterations and the lower right after 120,000 iterations

2.5 Conclusion

The Sirovision photogrammetry system was used to map the discontinuities and slope geometry for a rockfall hazard located in Mount Néron (French Alps). The data were processed to construct the structural model of a rock slope which was then used as input in a numerical model to carry out a stability analysis. A DFN-DEM formulation was chosen for modelling since it can explicitly take into account the fracture sets generated by Sirovision and for its ability to reproduce progressive failure mechanisms which are inevitable when non-persistent fracture planes are presented in the rock mass. Both sliding along pre-existing discontinuities and fracturing of the rock bridges located in between these discontinuities can thus be taken into account in the analysis to produce mixed failure mechanisms which cannot be usually tackled by conventional methods. The overall methodology, from the photogrammetry acquisition to the mechanical modelling and the stability analysis, is presented and discussed based on the Mount Néron case study.

The numerical simulations confirmed the stability of the blasted rock block before the SR was applied.

A Factor-of-Stability can be established applying a strength reduction method involving a TSSR method. However, the meaning of the defined Factor of Stability needs to be considered with caution as its value might depend on many assumptions, such as fracture mechanical and geometrical properties, rock bridge size and initial strength of the intact rock matrix at the decameter scale. Further investigations are being carried out to assess the reliability of such strongly non-linear factor, keeping in mind that the DEM simulation mainly provides a way to understand the failure mechanism before proposing a reasonable if not reliable stability criterion.

2.6 Acknowledgements

This work has been partly supported by the IMSRN company through a CIFRE grant N°2012/0710, the Research network "Vulnerability of structures undergoing a natural or technological hazard" (Grenoble, France) and the Sirovision project (CSIRO, QCAT, Pullenvale, Australia). The laboratory 3SR is part of the LabEx Tec 21 (*Investissements d'Avenir* - grant agreement n°ANR-11-LABX-0030).

CHAPTER 3

DEM analysis of rock bridges and the contribution to rock slope stability in the case of translational sliding failures

In the presence of joint sets sub–parallel to a slope face, the stability of the rock mass is assumed to be controlled by the shear strength along the joints. If the joints are persistent, the shear strength can be assessed according to the Mohr–Coulomb criterion with appropriate values for the cohesion and the friction angle on the associated surface. If the joints are non–persistent with their continuity being interrupted by the presence of rock bridges, their apparent strength increases considerably. In this case, the contribution of the rock bridges has to be accounted for in the stability analysis. Jennings' formulation is considered to be one of the first rock slope stability analysis that evaluates the resistance to sliding as a weighted combination of both intact rock and joint planes strengths. The present study discusses the validity of Jennings' formulation. The progressive failure of a rock slope involving a non–persistent joint is numerically investigated based upon simulations performed using a Discrete Element Method specifically enhanced to model jointed rock masses. The intact material is represented as an assembly of bonded particles. Pre-existing discontinuities are explicitly included in the model by using a modified contact logic that ensures an explicit and constitutive mechanical behaviour of the joint planes. The failure of the rock bridges is simulated through the breakage of the inter-particle bonds. In addition, rock bridges can be spatially distributed along the sliding surface following a prescribed spatial probabilistic distribution. The respective contribution of spatial distribution of rock bridges over the main sliding plane, the dip angle of that plane and the location of the centre of gravity of the likely unstable block were investigated through a series of numerical simulations and the results systematically compared

to Jennings' predictions. The limit of Jennings' formulation appears as soon as tensile failure becomes predominant and an alternative formulation is proposed to assess the resulting equivalent strength.

3.1 Introduction

Geologic structures play a major role in rock slope stability. The structural model, which provides the orientation, distribution and nature of the discontinuities at different scales, represents a key feature of the geotechnical model (Read (2007); Brideau et al. (2009); Stead and Wolter (2015)). If the discontinuities are persistent, potentially unstable structures such as classic planar and wedge failures can be easily identified. Their stability can then be directly assessed using the Mohr–Coulomb criterion, assuming appropriate values for the cohesion and the friction coefficient along the joint surface (Hoek (1983); Wyllie and Mah (2004)). In the case where discontinuities are non–persistent, the contribution of rock bridges needs to be considered, especially in sedimentary rocks where bedding planes act as preferential sliding surfaces (Havaej et al., 2014). For instance, planar failures can develop by combining sliding along non–persistent discontinuities (joints) and fracturing of the intact rock bridges located in between (Einstein et al. (1983); Sturzenegger and Stead (2012); Scholtès and Donzé (2015)). Jennings (1970) introduced a detailed limit equilibrium model for estimating the stability of a slope where such planar failures may occur. This formulation is considered as one of the first analytical rock slope analyses that includes the possibility of shear failure both along joints and through intact rock. Attempts have also been made to solve the planar failure problem using an equivalent continuum approach. For example, Hoek–Brown failure criterion deals with the combined influence of intact rock and non–persistent joints by considering the rock mass as an equivalent continuous medium (Hoek and Brown (1997); Hoek et al. (2002)). However, this approach ignores the failure history that can dramatically influence the overall *in situ* stress as well as the failure kinematics which is generally controlled by the orientation of the discontinuities.

The reliability of Jennings' formulation has been previously discussed from diverse approaches (see for instance Einstein et al. (1983); Scavia (1990); Mejía-Camones et al. (2013)), but has not been exhaustively tested. Besides the application of this analytical formulation, a transition from deterministic to probabilistic approaches has been developed to deal with issues related to parameter uncertainty in order to provide more reliable analyses, *e.g.* Baczynski et al. (2000) and Miller et al. (2004). The study presented here uses Jennings' formulation as a reference case to investigate how the spatial distribution of rock bridges, the dip angle of the main sliding plane, as well as the location of the centre of gravity of the likely unstable block, can affect the stability analysis in the case

of translational sliding failures.

To introduce Jennings' formulation, we consider the Factor of Safety (FoS) which can be formulated to assess the stability of a rock slope in the presence of a single persistent sliding surface as Wyllie and Mah (2004):

$$FoS = \frac{T_{max}}{F_{gx}} = \frac{Ntan\phi + cA}{F_g sin\theta} \tag{3.1}$$

where T_{max} is the maximum shear force along the joint surface with N the normal force, ϕ the frictional angle of the sliding plane, c the cohesion, A the sliding area (joint surface), θ the inclination angle of the joint surface, and F_{gx} is the tangential component of the gravitational force F_g.

Failure occurs when the shear strength of the joint is unable to resist the driving force, *i.e.* $FoS < 1$. Based on this consideration the critical cohesion for FoS. Based on this consideration, the critical cohesion, c_{crit}, for $FoS = 1$ is given by,

$$c_{crit} = \frac{F_g cos\theta}{A}(tan\theta - tan\phi) \tag{3.2}$$

If the joint is non-persistent, *i.e.* its continuity interrupted by the presence of rock bridges (Figure 3.1), its shear strength increases considerably (Jennings (1970); Wittke (1990)). The critical cohesion is therefore controlled by both the strength of the rock matrix and the strength of the pre-existing joints.

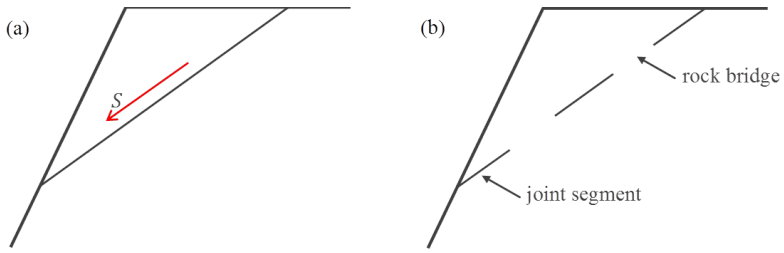

Figure 3.1: (a) shear failure through a persistent joint. (b) co–planar joints between rock bridges (after Einstein et al. (1983)).

Considering the presence of co-planar joints separated by intact rock bridges, the relative amount of intact rock along the sliding surface can be expressed by the ratio k, defined as:

$$k = \frac{\sum A_j}{\sum A_j + \sum A_r} \tag{3.3}$$

with $\sum A_j$ the joint surface and $\sum A_r$ the rock bridge surface (Figure 3.2).

Therefore, if a Mohr-Coulomb criterion is still relevant to describe the behaviour of a non-persistent joint, its parameters might be replaced by the equivalent parameters c_{eq} and ϕ_{eq}, as proposed by Jennings (1970):

$$c_{eq} = (1 - k)c_r + kc_j \tag{3.4}$$

$$tan\phi_{eq} = (1 - k)tan\phi_r + ktan\phi_j \tag{3.5}$$

with ϕ_r and ϕ_j the friction angles of the intact rock and of the joint respectively, and c_r and c_j the cohesions of the intact rock and the joint respectively.

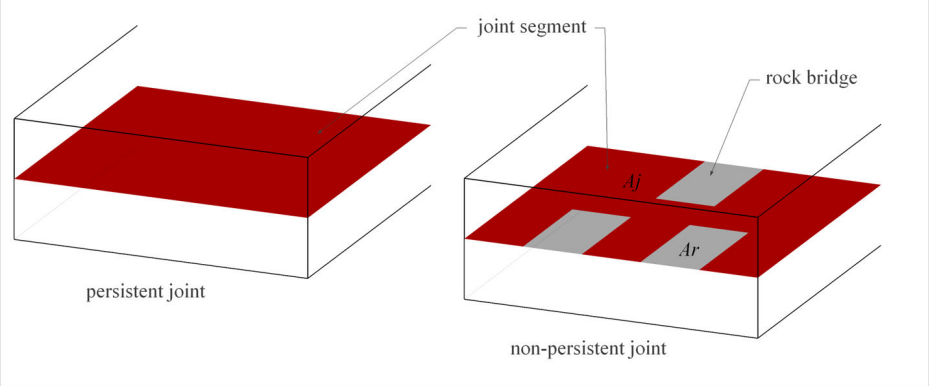

Figure 3.2: Persistent and non–persistent joints (Adapted from Wittke (1990)).

The objective of the present study is to directly compare this formulation to the predictions of a numerical model that offers the possibility of explicitly describing rock bridge failure. The model is based on the discrete element method (DEM) which was chosen for its capability to model progressive failure mechanisms (Scholtès and Donzé (2012); Scholtès and Donzé (2013)). In addition to this numerical methodology, probability techniques were also applied here to prescribe the spatial distribution of the rock bridges along the sliding surface. First, the model will be presented together with the methods used to distribute the rock bridges along the failure surface. Then its predictions will be compared to Jennings' formulation (Jennings, 1970).

A sensitivity analysis is provided to emphasise the critical mechanisms that lead a slope to translational failure with the objective to discriminate between the respective roles of the joint dip angle, the mass distribution of the unstable block and the proportion of rock bridges on the destabilisation process. Finally, a discussion on the application and validity of Jennings' formulation will be carried out.

3.2 Model setup

Two models were used to generate different distributions of rock bridges along the likely sliding surface. First, a fractal distribution law was used to investigate the role of the location and clustering of rock bridges along the sliding plane. Second, a mean uniform distribution law was used to study the effect of the location and number of rock bridges, as well as the influence of their spatial distribution along the sliding plane.

3.2.1 Fractal distribution of rock bridges

The distribution of the rock bridges along the sliding plane was chosen to follow a fractal distribution law defined by a sub–division cascade process which corresponds to fractal probability fields (Harthong et al., 2012). In this case, the spatial density of rock bridges is assumed to be fractal and obeys Equation 3.6 (Bour and Davy (1999); Bonnet et al. (2001); Darcel et al. (2003); Davy et al. (2010):

$$n(L) = \alpha^D \tag{3.6}$$

where $n(L)$ denotes the number of rock bridges located within a joint surface of size L, α is a proportionality constant related to the quantity of rock bridges to be generated, and D is defined as the clustering fractal dimension. The exponent D controls the correlation between the probability values; the smaller it is, the more rock bridges are clustered within the zones of high probability. The value of D is related to a fractal dimension and constrains the density distribution for the rock bridges among the probability values.

An algorithm modified after Harthong et al. (2012) was used to generate rock bridges along the sliding plane. At the first iteration, the plane of size $L \times L$ is divided into four sub-domains of dimension $L/2$. A probability value (P_i) is assigned to each of the four sub–domains. This set of four probabilities is maintained throughout the sub–division process. At the second iteration, each sub–domain is divided into four more sub–domains of dimension $L/4$, and the four probabilities are assigned to the four sub–domains with a random permutation (Figure 3.3). The rock bridges were generated in a two-dimensional plane (*i.e.* the sliding plane); hence D was kept within the range 1, 2. Considering that D quantifies the probability of finding a rock bridge in the vicinity of another one, when $D = 2$, this probability is not correlated to the position of its neighbours. On the other hand, when $D < 2$, there is an increasing probability of finding a rock bridge in the vicinity of another one.

A trapezoidal prism intersected by a plane of 10×10 m^2 representing the sliding surface was used as the geometrical model (Figure 3.4). The sliding plane was divided in 16 cells, *i.e.* 16 sub-domains, following the sub-division cascade process described

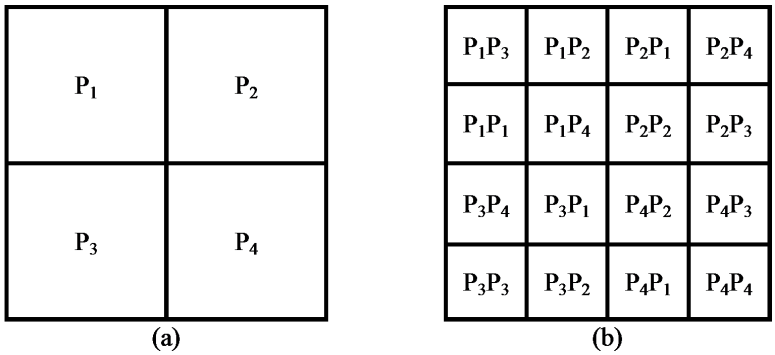

Figure 3.3: 2D illustration of the subdivision cascade process. (a) First sub–division step: each subdomain is assigned a probability P_i. (b) Second sub–division step: each subdomain is subdivided, and the probabilities P_i are randomly assigned to the sub–subdomains. The resulting probability for each subdomain at subdivision step n is the product of the n probabilities assigned at each step (after Darcel et al. (2003)).

previously (Figure 3.4(a)). Three different sets of fractal distribution were generated for D equal to 1, 1.5 and 2, respectively. One of these sets is represented in Figure 3.5, showing how the distribution of the rock bridges on the surface depends on the D value. For $D = 1$, the rock bridges are clustered in the cells with high probability. For $D = 1.5$, the rock bridges are more scattered along the surface. Finally, for $D = 2$, the probability of finding a rock bridge is equivalent for every cell, thus the rock bridges are uniformly distributed over the sliding surface.

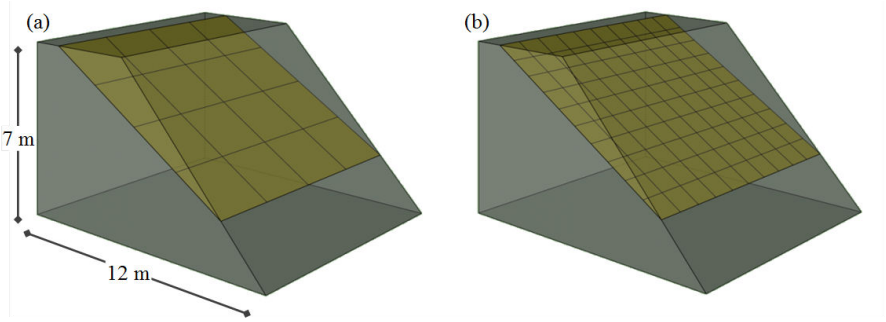

Figure 3.4: Sliding plane of 10×10 m^2. (a) division into 16 cells for the fractal distribution generation. (b) division into 100 cells for the mean uniform distribution generation.

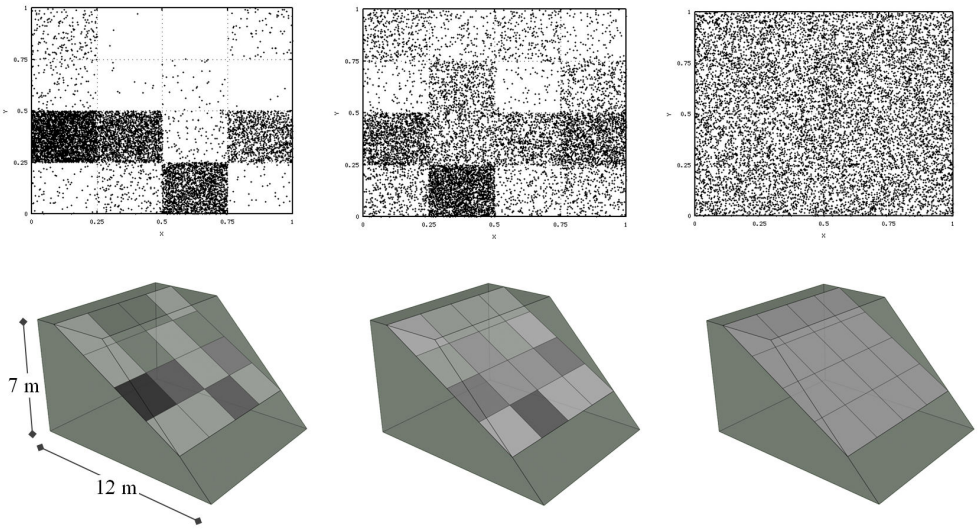

Figure 3.5: Fractal distribution law. From the left to the right, 6% of rock bridges distribution for $D = 1$, $D = 1.5$ and $D = 2$.

The quantity of rock bridges that are distributed along the surface is given by the inverse of the number of sub–domains. In this case, 16 sub–domains were used in the sub–division cascade process. Thus 6% of rock bridges are located along the sliding surface. This percentage was kept constant no matter the D value assumed. One drawback to this method is that it does not support the analysis of the effect of the number of rock bridges on stability. To overtake this limitation, a mean uniform distribution law was thus introduced.

3.2.2 Mean uniform distribution of rock bridges

The sliding plane of 10×10 m^2 was divided into 100 identical cells (Figure 3.4(b)). Similarly to the fractal case described previously, an algorithm was developed to generate the rock bridges along the sliding plane. Taking advantage of the division of the plane into 100 cells, the total area of rock bridges is defined as a percentage, which can be chosen initially. All the cells have the same probability of being chosen, so each time a percentage is defined, the selection is made randomly over the plane. Some of the configurations used in this study are shown in Figure 3.6, where rock bridges are represented in black and joints in light green.

3.2.3 Role of the mass distribution of the sliding block

To analyse the effect of the mass distribution of the sliding block, two additional configurations were tested with different shapes for the sliding block. From the original slope

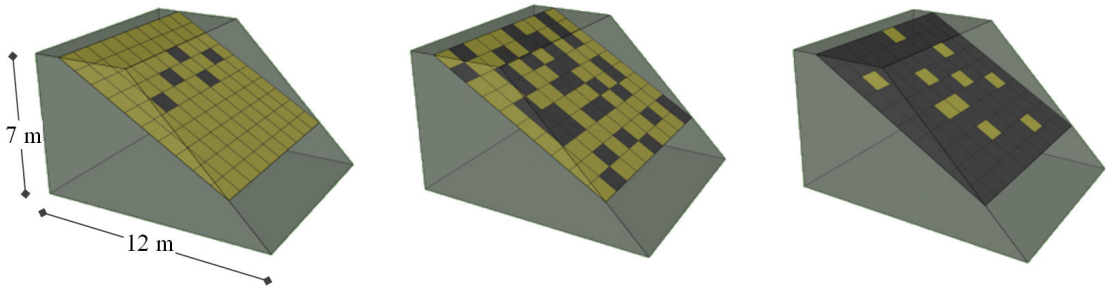

Figure 3.6: Mean uniform distribution of rock bridges. From the left to the right, configurations with 5%, 35% and 90% of rock bridges. Rock bridges (cohesive zones) are represented in black, and the joints (frictional zones) are represented in light green.

model (Figure 3.7, left), where the centre of gravity is located on the upper part of the block, a second configuration was derived for which the block was rotated, such that its centre of gravity is shifted to the lower part of the slope (centre of Figure 3.7). In the third configuration, the shape was modified, such that the block is a rectangular parallelepiped with the same volume and its centre of gravity being located at the centre of the block (Figure 3.7, right).

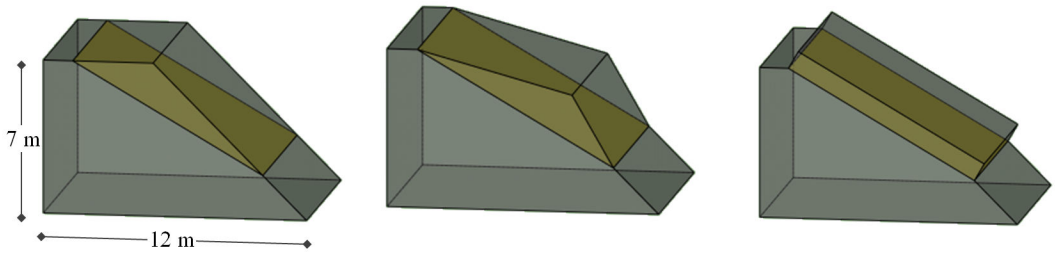

Figure 3.7: Different block shapes used in the stability analysis. On the left, the centre of gravity is located in the upper part of the block. On the centre, the block was rotated upside down, thus its centre of gravity is located in the lower part of the block. On the right, keeping the same volume, the block was modified as a regular shape with its centre of gravity located at the centre of the block.

3.2.4 Role of the dip angle of the sliding surface

Different dip angles were tested to assess their influence on the failure mechanism. The objective was to compare the results obtained for the gentle slope (*e.g.* 30°) to the ones obtained for steeper slopes (50° and 70°), in which failure may occur in mixed shear and tensile modes.

In order to make the results comparable, the shape (and thus the weight) of the sliding block was kept constant by rotating the gravity vector, instead of changing the

dip of the sliding surface which would have changed the geometry of the structure. In Figure 3.8, the original configuration (with a dip angle of 30°) is shown being rotated to obtain steeper angles for the sliding surface. Numerically, this effect was implemented by carefully changing the direction of the gravity vector.

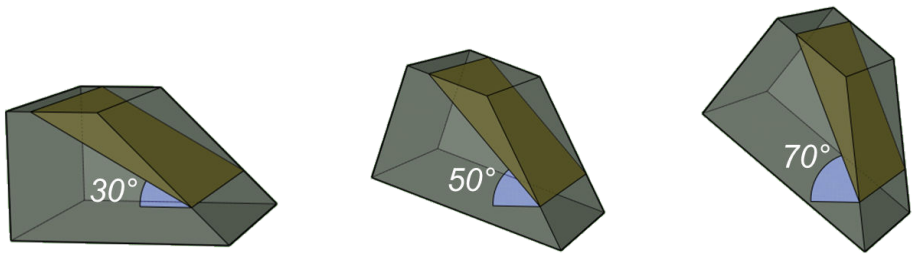

Figure 3.8: The three different dip values used in the present stability analysis.

3.2.5 Discrete Element Method

The simulations were run with Yade Open DEM (Kozicki and Donzé (2008); Kozicki and Donzé (2009)), an extensible open-source software based on the discrete element method (DEM). The intact rock is modelled as a bonded particle assembly (Scholtès and Donzé (2012); Scholtès and Donzé (2013); Donzé and Magnier (1995)).The inter-particle bonds obey elastic-brittle behaviour in both normal and tangential directions. The bonds can break either by tension or shear failure mechanisms according to a modified Mohr-Coulomb criterion with a tensile cut off. After bond breakage, particles can interact through frictional contact. As in Bonilla-Sierra et al. (2015), the model was calibrated so as to simulate the macroscopic behaviour of a brittle rock with a volumetric mass ρ equal to 2,500 kg/m^3, a Young's modulus E of 35 GPa, a Poisson's ratio ν of 0.3, a tensile strength TS of 0.75 MPa, a uniaxial compressive strength UCS of 7 MPa, a cohesion c of 1.9 MPa and a friction angle ϕ equals to 33°. These macroscopic properties were obtained by defining a local normal stiffness at the bond scale equal to $70 \times \bar{D}$ GPa.m with $\bar{D}$ being the harmonic mean of the interacting particles diameters (Scholtès and Donzé, 2013), as well as a bond shear/normal stiffness ratio of 0.3, a bond tensile strength of 1 MPa, a bond cohesion of 10 MPa, and a bond friction angle equals to 18°. In order to match the volumetric mass of the simulated medium and thus ensure an equivalent stress field inside the slope model, the volumetric mass of each particle was set equal to 5,000 kg/m^3 to counterbalance the porosity of the particle assembly.

In addition, a smooth joint model (SJM) formulation was used to explicitly represent the discontinuities in the numerical medium. The joints are simulated by slip surfaces located between the particles laying on the opposite side of the joint surface (see Scholtès and Donzé (2015); Scholtès and Donzé (2012); Scholtès and Donzé (2013); Harthong et al.

(2012); Bonilla-Sierra et al. (2015) for details). The SJM formulation provides a direct equivalence between the properties of the macroscopic discontinuity and the properties of the inter-particle bonds crossing this discontinuity. Moreover, the SJM ensures that the behaviour of the simulated joint surface is independent of the inherent discretisation or roughness produced by the arrangement of the particles along the interface (Scholtès and Donzé, 2015). The discontinuities, or so-called joints, were chosen to have no cohesion with a friction angle of 20°. Once the properties were set up, the particles were packed inside the closed trapezoidal prism following the procedure described in Bonilla-Sierra et al. (2015) and illustrated in Figure 3.9(a).

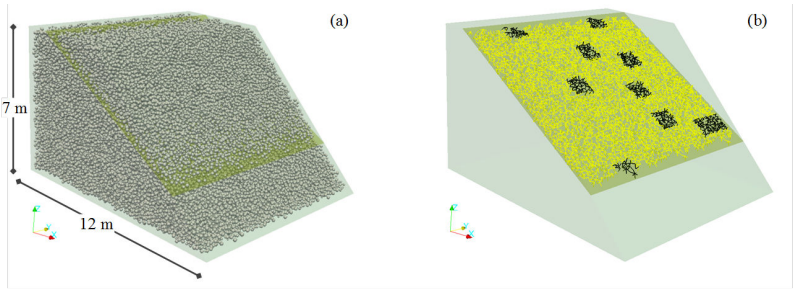

Figure 3.9: (a) DEM model of the slope containing a single sliding plane. (b) 10% of cohesive rock bridges in black and frictional joint area in yellow.

Either the fractal distribution law or the mean uniform distribution law were used to determine the location of the cohesive and frictional zones along the sliding plane. The bonds located within a frictional zone, *i.e.* a joint, were thus assigned the SJM with no tensile strength, no cohesion and a friction angle equal to 20° (Cundall et al. (2008); Mas-Ivars et al. (2011)). The bonds located within a cohesive zone, *i.e.* a rock bridge, were assigned the same properties as the ones located within the rock matrix (tensile strength of 1 MPa, cohesion of 10 MPa and friction angle of 18°). The procedure is illustrated in Figure 3.9(b) for 10% of rock bridges generated following the mean uniform distribution.

3.2.6 Slope stability analysis using a Tensile and Shear Strength Reduction method

Rock slope failure is frequently triggered by the progressive rupture of rock bridges caused by weathering process, *e.g.* Eberhardt et al. (2004). In order to simulate this progressive degradation process, a tensile and shear strength reduction (TSSR) method was used here to promote failure. The TSSR method involves the progressive decrease of the inter–particle bond strength by reducing simultaneously both their tensile and shear components. Although being an oversimplification of the actual weathering process taking place in nature, the method presents the advantage of keeping the same shape for the

failure envelope of the rock material during the degradation process, ensuring therefore a realistic behaviour (Bonilla-Sierra et al., 2015). The TSSR method is controlled through the introduction of a *TSSR* factor, which is applied iteratively to the initial bond strength, until failure occurs. The final *TSSR* factor indicates how much the initial strength needs to be reduced to reach the instability, and it is defined as follows:

$$TSSR = \frac{failure\ strength}{initial\ strength} \tag{3.7}$$

In this study, the degradation was only applied to the bonds located across the sliding surface, in order to trigger failure of the rock bridges preferentially. This choice was made in order to do a direct comparison with Jennings' formulation.

3.3 Numerical results

3.3.1 Failure process analysis

Failure in the numerical model results from the breakage of the inter–particle bonds. These so-called cracks (or micro–cracks) that are induced by the TSSR method can be promoted by both in–plane shear (mode II) and tensile (mode I) failure mechanism.

The respective occurrence of shear and tensile cracking was recorded for different dips of the sliding surface and for different rock bridge percentages. For each case (10%, 50% and 90% of rock bridges), progressive failure occurs when the cohesive bonds making up the rock bridges break, resulting in the irreversible sliding of the block, as shown in Figure 3.10.

However, failure develops in different manners depending on the slope configuration (Figure 3.10. For instance, as expected, the relative number of tensile cracks increases significantly as the dip increases. This tendency highlights the change in the kinematics of failure, from pure shear failure mode for the joint with a 30° dip to a mix shear-tensile failure mode for the joint with a 70° dip. Moreover, shear cracks tends to appear simultaneously over the entire joint surface, while tensile cracks develop in a progressive manner as failure progresses. Tensile cracks can be identified in two distinct zones: those located at the top of the model that result from the toppling tendency of the block; and those observed at the toe of the slope, that propagate inside the rock matrix, within the sliding block. These latter ones are also induced by the slight toppling process which tends to bend the block over its base.

Regarding the modes of failure, the number of tensile and shear cracks varies as a function of the dip angle and depends also on the position of the centre of gravity of the sliding block as shown in Figure 3.11. For the configuration where the centre of gravity

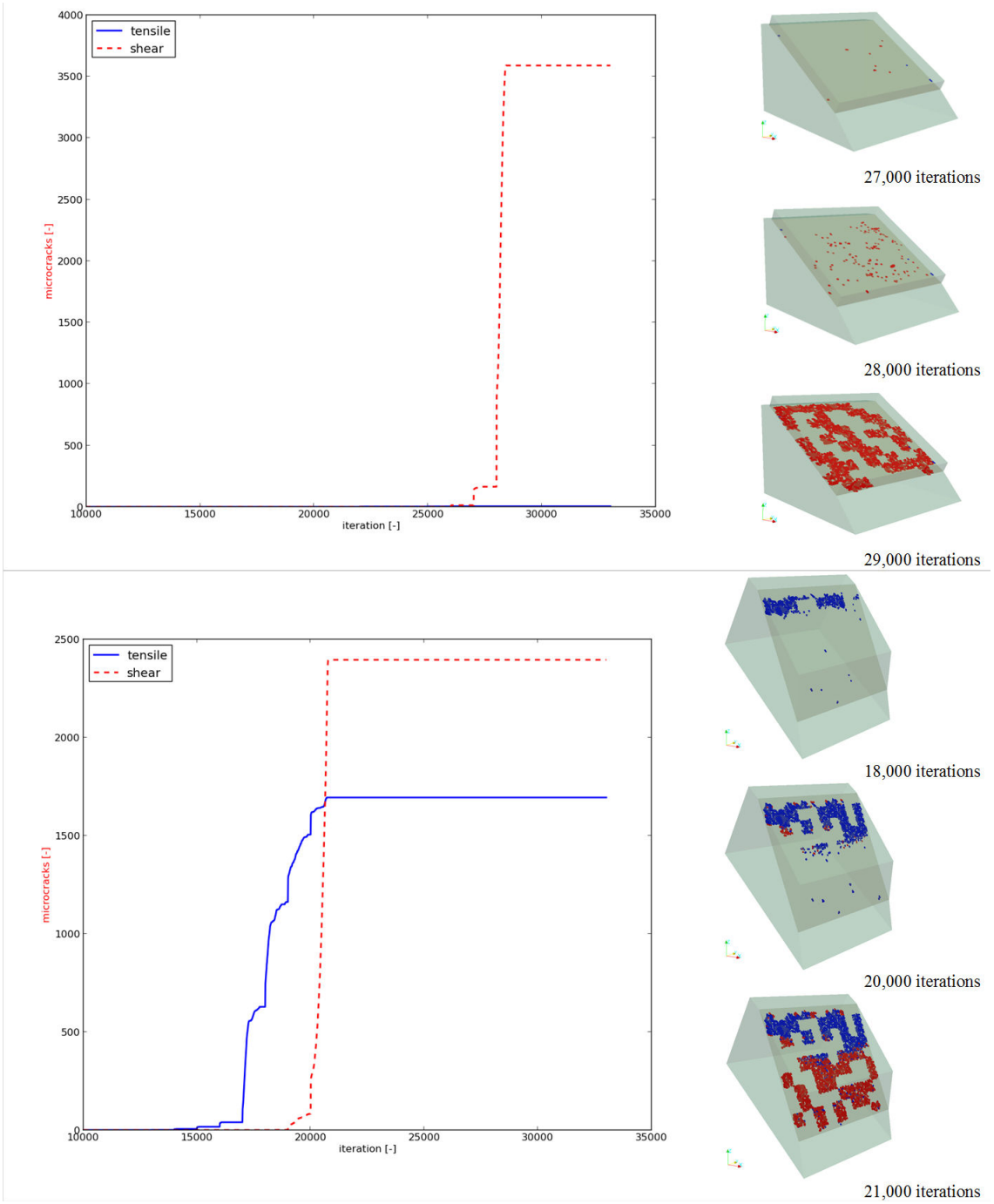

Figure 3.10: Cumulative number of shear and tensile cracks plotted versus time and sequential distributions of tensile (blue) and shear (red) micro-cracks along the failure plane for to cases: *i* top, configuration with a dip angle equal to 30° and 50% of rock bridges, and *ii* bottom, configuration with a dip angle equal to 70° and 50% of rock bridges.

is located on the upper part of the block (Figure 3.7, left), the number of tensile cracks is very low for a dip equal to 30° and remains constant regardless the percentage of rock bridges. On the other hand, the total number of shear cracks increases linearly as the percentage of rock bridges increases. For this configuration, the number of shear cracks is equivalent to the number of initial cohesive bonds, indicating that the rock bridges fail predominantly by mode II (see top of Figure 3.11, continuous green curve and dashed black line). For higher dip angles (50° and 70°), shear cracks remain predominant. Nevertheless, the number of tensile cracks increases as the dip angle increases, particularly when the percentage of rock bridges is higher than 50% (top of Figure 3.11, dashed blue and red curves). As the dip increases, the moment generated from the force couple (weight vector and reaction force on sliding plane) makes the block more susceptible to toppling and thus induces more tensile cracks.

For the case where the sliding block has its centre of gravity located in the lower part of the slope (centre of Figure 3.7), the number of tensile cracks increases as the proportion of rock bridges increases, even when the dip is as low as 30° (centre of Figure 3.11, dashed green curve). Therefore, the number of shear cracks decreases, especially when the dip is 70° for which the number of tensile cracks tends to be equivalent to the number of shear cracks (centre of Figure 3.11, continuous blue line). The more the dip increases, the more the block tends to rotate around its base thus promoting failure of the rock bridges by mode I.

Finally, when the weight of the sliding block is uniformly distributed over the sliding surface, and the dip angles are equal to 30° and 50°, the number of tensile cracks is close to zero. For these dip values in particular, failure occurs almost exclusively by mode II, with a number of shear cracks very close to the number of initial cohesive bonds (bottom of Figure 3.11, continuous green and red lines and dashed black line). When the dip angle is equal to 70°, the number of tensile cracks increases slightly as the percentage of rock bridges reaches 25%, but remains low compared to the cases with lower dip (bottom of Figure 3.11, dashed blue line). As expected, the geometry (shape) of the block constrains the way the rock bridges fail, mode I being non negligible as soon as toppling of the unstable block, even limited, is observed.

Tensile cracks are more likely to appear when rock bridges are located in the upper part of the failure surface due to the proximity of the free surface, which lets the upper part of the block detach and topple. As shown in Figure 3.10, when rock bridges are located in the central part and in the lower part of the failure plane, the failure mode is most likely shear. On the other hand, if the rock bridges are clustered in the upper part of the sliding surface, failure may occur by tensile mechanism.

In the case where the percentage of rock bridges is lower than 50%, the variability in their spatial distribution associated with particular realisations can significantly affect the interpretation of the observed failure mode and the ratio of shear cracks versus tensile

cracks. To study this particular aspect, a clustered configuration, *i.e.* with a fractal exponent D equal to 1, was used to generate three different realisations: one with most of the rock bridges located in the upper part of the plane, a second one with rock bridges in the central part and a third one with rock bridges in the lower part (Figure 3.12). Each of these configurations was also tested for different dip angles. A first confirmation is that in the case where the rock bridges are predominantly located in the upper part of the sliding plane, tensile failure mode becomes significant.

According to Jennings' formulation (Jennings, 1970), shear failure of a slope tends to take place on planes which pass along both pre-existing joints and rock bridges. However, the results obtained in this study show that tensile cracks appear as the dip angle increases even for co–planar joints. These tensile cracks may affect the value of the equivalent cohesion reached at failure (Mejía-Camones et al., 2013).

3.3.2 Critical equivalent cohesion

Using Equation 3.2, the critical cohesion, c_{crit}, for $FoS = 1$ can be calculated for the different dip angles used in this study (30°, 50° and 70°). In Table 3.1 the analytical values calculated from Equation 3.2 are compared to the cohesion obtained numerically for the cases with 100% of rock bridges.

parameter	cohesion for dip=30°	cohesion for dip=50°	cohesion for dip=70°
c_{crit} from Eq.3.2 [kPa]	4	13	19
1^{st} configuration [kPa]	6±25%	13±45%	18±45%
2^{nd} configuration [kPa]	13±25%	32±45%	42±45%
3^{rd} configuration [kPa]	3±25%	13±45%	18±45%

Table 3.1: Critical cohesion values obtained analytically and numerically

Jennings' equivalent cohesion was calculated using Equation 3.4, considering c_j equals to zero. The resulting curve was then plotted and compared to the model predictions for different percentages of rock bridges (Figure 3.13). The variability range of the numerical results is ±25% for the cases with the dip equal to 30°, and increases up to ±45% for the cases when the dip is equal to 50° and 70°. This variability range is observed on several rock bridge realisations generated by the fractal distribution law, given the same D value and the same percentage of rock bridges (6%), which takes into account the difference in the spatial distribution of the rock bridges along the sliding surface.

In general, for the three different geometrical configurations and for a low dip angle, the numerical model is in good agreement with the deterministic approach, as observed

in Figure 3.13. The critical equivalent cohesion obtained for the dip equal to 30° is within the area below the curve generated using Jennings' law (in yellow) for all the percentages of rock bridges considered. However, as the dip angle increases, a combination of tensile and shear failure mechanisms is observed and Jennings' law is no longer verified.

In summary, for cases that involve co–planar joints segments, Jennings' formulation appears to be quite conservative when the dip angle is low (*i.e.* 30°) and when the percentage of rock bridges is lower than 50%. In this case, the critical equivalent cohesion obtained with the analytical model is higher than the value obtained with the DEM model. However, since Jennings' formulation neglects tensile failure, the critical equivalent cohesion obtained numerically for higher angles (*e.g.* 50° and 70°), is significantly higher than the ones predicted by Jennings' formulation.

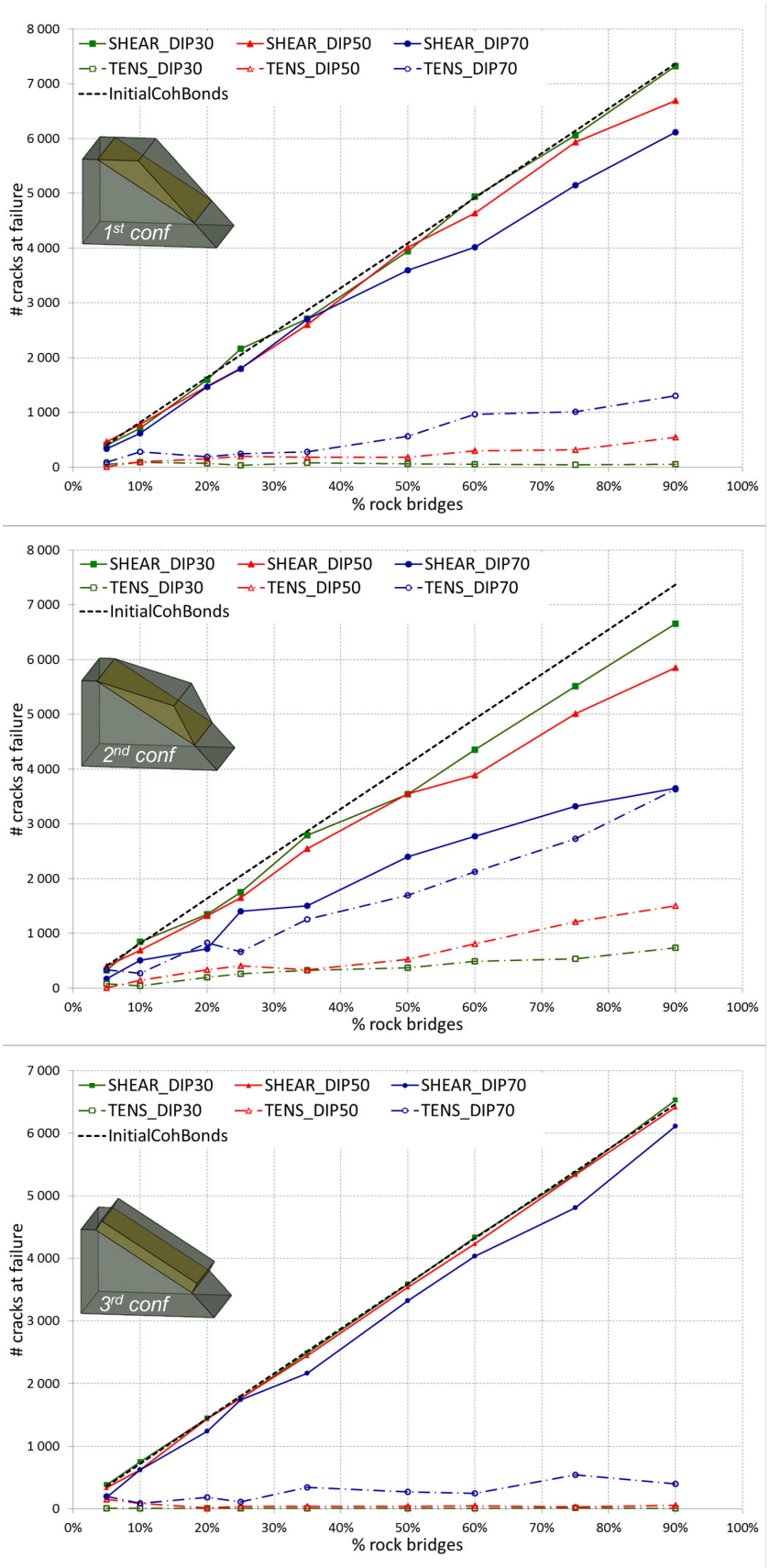

Figure 3.11: Shear and tensile cracks occurrences are represented depending on the percentage of rock bridges for three different geometries of the blocks. The dashed lines represent the tensile cracks whereas the continuous lines represent the shear cracks.

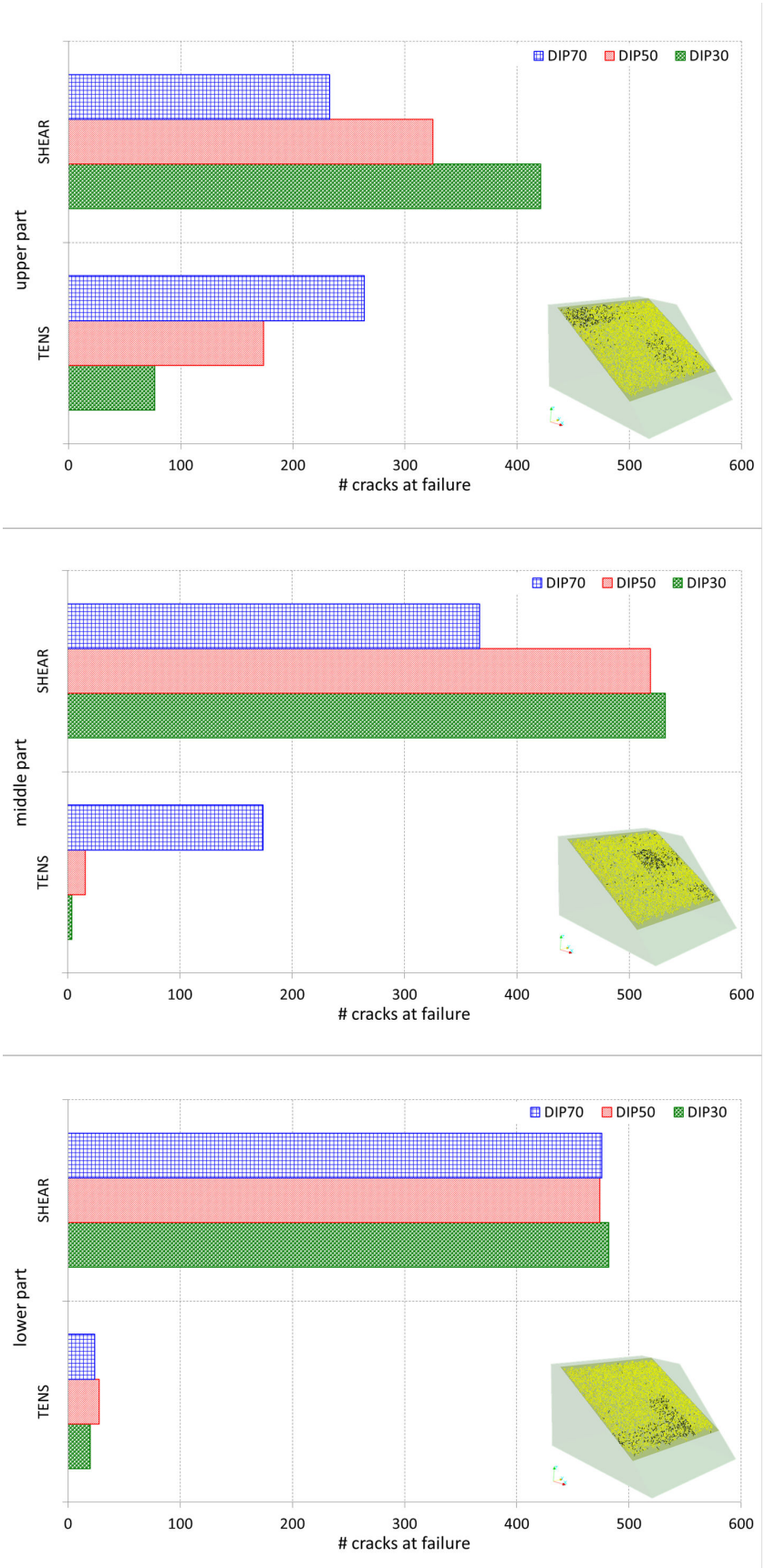

Figure 3.12: Number of shear and tensile cracks registered at failure depending on the spatial distribution of 6% of rock bridges (in black). From top to bottom: rock bridges mainly distributed on the upper, middle and lower parts of the sliding surface, respectively.

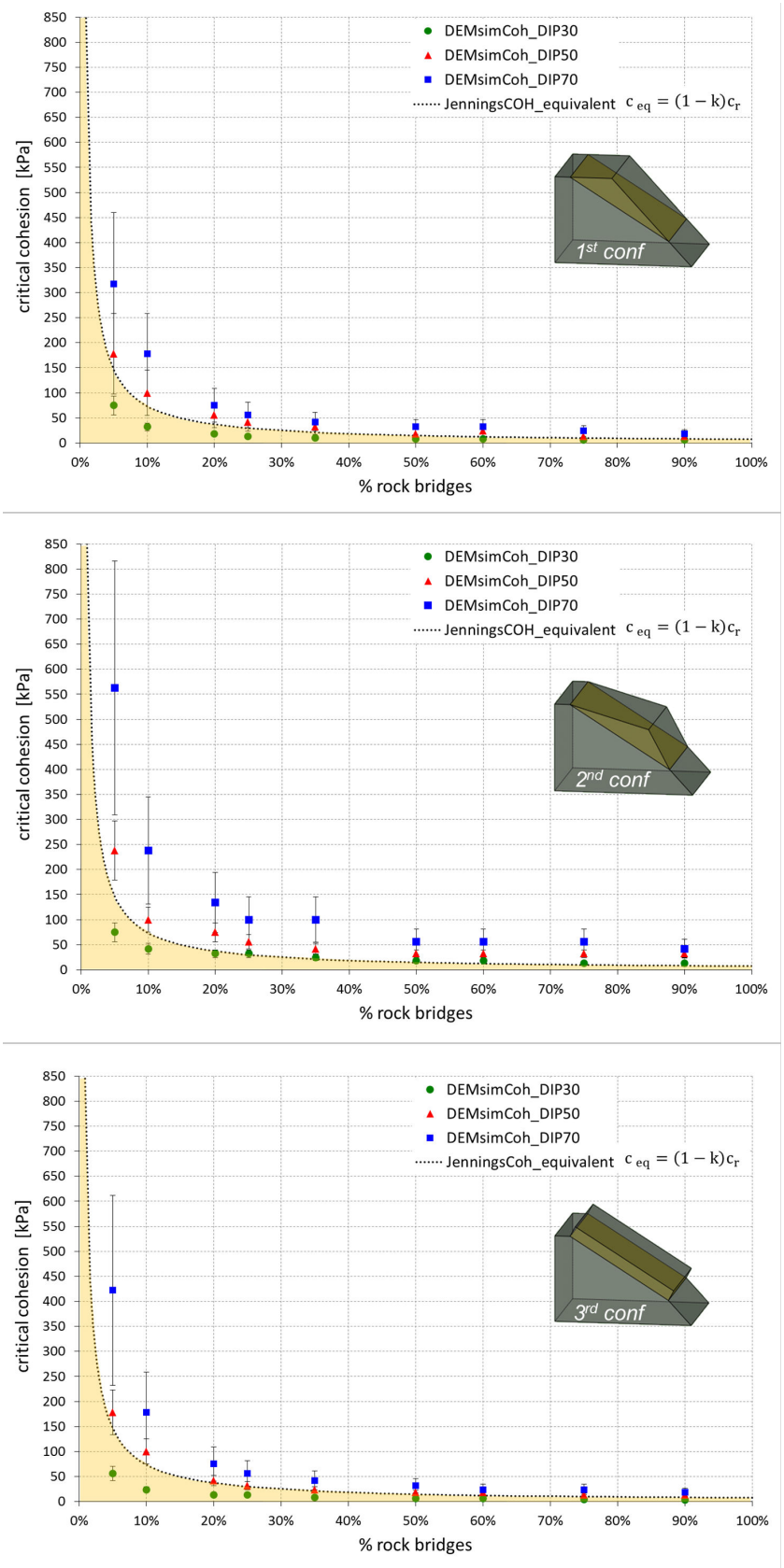

Figure 3.13: Top to bottom: critical equivalent cohesion obtained numerically for different percentages of rock bridges and different shapes of the block compared to Jennings' formulation. The error bars represent the variability found for 6% of rock bridges depending on their distribution (fractal law) along the sliding plane.

3.4 Discussion

From these numerical results, it seems that Jennings' formulation is well adapted to cases where failure predominantly occurs in shear mode, *i.e.* when the sliding surface has a low dip angle (dip $< 50°$). For these low dip angle values, the numerical results are in best agreement with Jennings' equation (Equation 3.4) when the percentage of rock bridges is higher than 50%. However, Jennings' formulation is shown to be conservative when the percentage of rock bridges is lower than 50%. For high dip angles, when failure combines shear and tensile modes, high discrepancy is observed between the critical cohesion obtained numerically and the values obtained analytically (Figure 3.13). Likewise, the discrepancy appears to increase as the dip angle increases as shown in Table 3.1 and Figure 3.13.

The mass distribution of the unstable block and the distribution (localisation and percentage) of the rock bridges on the sliding plane are additional parameters influencing the failure mode, as it can be observed from Figure 3.10 to Figure 3.12, where it can be seen that the evolution in the number of tensile and shear cracks considerably varies depending on these parameters. To sum up, several parameters strongly control the value of the equivalent cohesion and they are not taken into account in Jennings' formulation.

Moreover, when the centre of gravity of the sliding block is located on the lower part of the slope and the dip angle is equal to 70°, the number of tensile cracks is almost equivalent to the number of shear cracks (Figure 3.11, second configuration). In this particular case, the equivalent cohesion may thus relate to the tensile strength of the rock bridges. In order to show this correlation, additional numerical simulations were carried out. The model was rotated so that the unstable block (considering the three different shape configurations) would be pulled outwards in the direction of the gravity (top of Figure 3.14) to estimate the equivalent tensile strength, T_{eq}, as a function of the percentage of rock bridges, such as,

$$T_{eq} = (1 - k)T_r \tag{3.8}$$

where T_r is the tensile strength obtained numerically with 100 % of rock bridges. For the three different configurations, T_r is equal to 27.8 kPa (see the upper part of Figure 3.14). Here, the kT_j term disappears due to the assumption that the joint has a null tensile strength. Additional simulations were run on each configuration for different percentages of rock bridges. The resulting values and their variability are plotted in the upper part of Figure 3.14 along with the curve obtained using Equation 3.8. This equation seems to fit the lower limit of the envelope obtained numerically for percentages of rock bridges lower than 50%. Equation 3.8 may thus underestimate the tensile strength for

that particular condition. For rock bridges percentages higher than 50%, Equation 3.8 is in good agreement with the numerical data.

The values for critical apparent cohesion previously obtained with the second shape configuration and dip equal to 70° are similar to the ones obtained using Equation 3.8 (bottom of Figure 3.14). This latter result shows that, for configurations involving steep dip angles, failure is mainly driven by tensile failure mode.

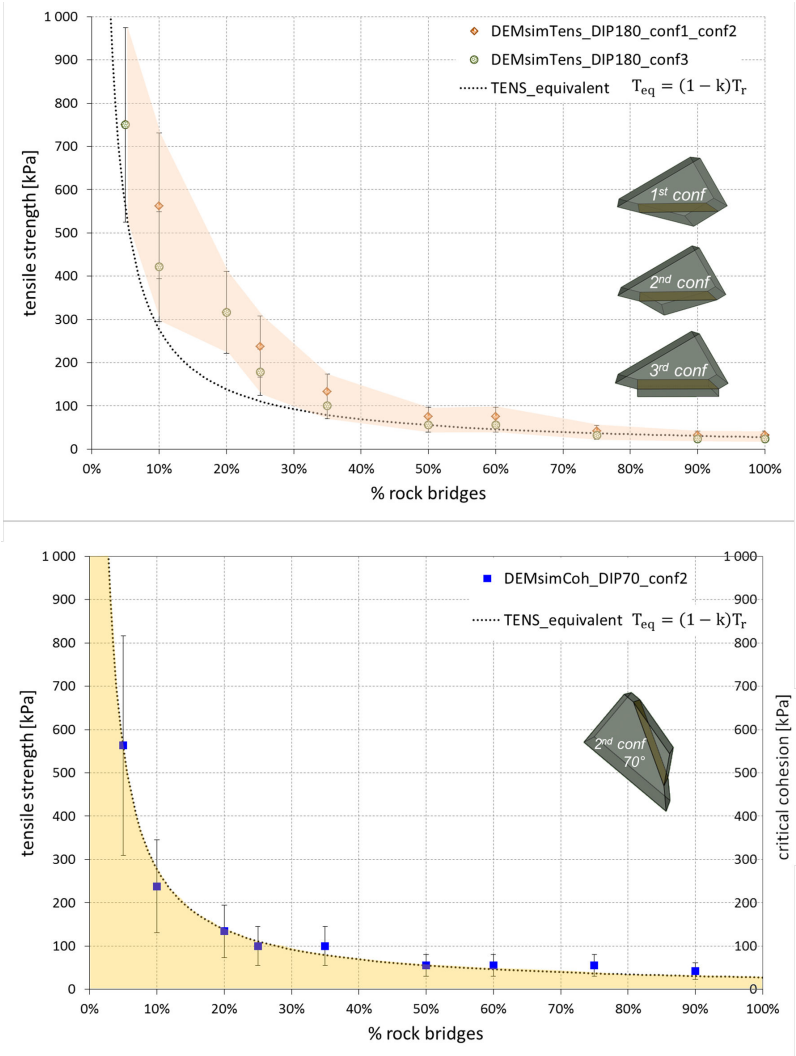

Figure 3.14: Top: critical equivalent tensile strength obtained numerically for different percentages of rock bridges and different shape configuration compared to the critical tensile strength obtained using Equation 3.8. The shaded region is the envelope generated from the tensile strengths and their variability related to the spatial distribution. Bottom: critical equivalent cohesion obtained numerically for the second shape and dip of 70°, compared to the equivalent tensile strength obtained using Equation 3.8.

3.5 Conclusions

The methodology proposed here combines probabilistic techniques and numerical modelling to analyse the translational failure of a jointed rock slope in presence of rock bridges. Numerical simulations were performed using a simplified configuration involving a single failure plane containing both frictional joints surfaces and cohesive rock bridges in order to simulate the progressive failure of the slope and to compute the critical equivalent cohesion needed to ensure stability.

The validity of Jennings' formulation was discussed for different distributions of rock bridges along the failure surface as well as for different locations of the centre of gravity of the block. Despite the simplicity of the geometrical model, it has been shown that Jennings' prediction could be confirmed for failure surfaces with low dip angles, *i.e.* 30°, where failure occurs mainly through shear mode. For joints with higher dip angles (typically superior to 50°) and for which failures occur through a combination of tensile and shear modes, Jennings' formulation underestimates the critical equivalent cohesion value.

Moreover, for cases where the centre of gravity is located in the lower part of the sliding block and for which the dip angle is equal to 70°, failure may be driven by tensile mode. To verify this, additional numerical simulations were carried out and showed that values of critical cohesion obtained numerically fit the equivalent tensile strength calculated with Equation 3.8.

Summarising the obtained results, one can note that the progressive destabilisation process depends on the overall kinematics leading to failure which is not only a function of the dip angle of the sliding surface but also of the spatial distribution of the rock bridges along that surface, as well as of the shape of the unstable block.

The assessment of the distribution of rock bridges along a potentially sliding surface is a difficult task and geophysical methods, such as Ground Penetrating Radar (GPR) (Deparis et al., 2007) can help to locate them. However, the use of such techniques may be impractical and limited. The methodology presented here aims to contribute to refine the stability analyses wherever such data is available or not.

3.6 Acknowledgements

This work has been supported by the IMSRN company through a CIFRE grant N°2012/0710. The laboratory 3SR is part of the LabEx Tec 21 (*Investissements d'Avenir* - grant agreement n°ANR-11-LABX-0030).

CHAPTER 4

Analysis of a composite wedge failure using photogrammetric measurements and DFN-DEM modelling

Analysis and prediction of structural instabilities in open pit mines are an important design and operational consideration for ensuring safety and productivity of the mine. Unstable wedges and blocks daylighting at the surface of the pit walls may be identified through three-dimensional (3D) image analysis combined with the discrete fracture network (DFN) approach. Kinematic analysis based on polyhedral modelling can be used for first pass analysis but cannot capture composite failure mechanisms involving both structurally controlled and rock mass failures. A methodology is proposed here to overcome such limitations by coupling DFN models with geomechanical simulations based on the discrete element method (DEM). Further, the use of high resolution photogrammetric data is used to identify valid model scenarios. An identified wedge failure that occurred in an Australian coal mine is used to validate the methodology. In this particular case, the failure surface was due to the rock mass progressive failure that developed from the toe of the structure inside the intact rock matrix.

4.1 Introduction

Assessment of unstable wedges and blocks daylighting on proposed and operational surface mine excavations is critical for risk management in open pit mining. Discrete fracture networks (DFN) are increasingly being used in the mining and civil engineering communities

for analysis of *in situ* rock mass fragmentation as defined by the presence of individual rock blocks (*e.g.* Wang et al. (2003); Rogers et al. (2007); Elmouttie and Poropat (2012)). The DFN approach combined with polyhedral modelling and kinematic analysis has proven to be useful in providing a first pass and rapid assessment of both the location and likelihood of these potential hazards. This is due to the relatively low computational costs associated with this method supporting probabilistic approaches and multiple modelling scenarios (Elmouttie and Poropat, 2014). However, the method does not account for composite failure mechanisms involving both structurally controlled and rock mass progressive failure.

A complementary approach, coupling DFN with geomechanical modelling, such as the discrete element method (DEM), provides the capability to simulate composite failure mechanisms. This has been demonstrated by studying failures in natural rock slopes, especially when progressive failure mechanisms are involved (Bonilla-Sierra et al., 2015). In particular, the DEM-DFN approach can simulate the spatio-temporal evolution of the micro-cracking occurring within the intact rock as well as the creation of critical failure surfaces through the coalescence of both induced and pre-existing fractures (Scholtès and Donzé (2012); Bonilla–Sierra et al. (2015); Harthong et al. (2012)). The model output can be analysed to identify the development of critical failure surfaces and to estimate the kinematics of the failure.

DEM modelling has been used extensively in the analysis of rock slope instabilities due to its high capability to simulate the fracture propagation inside the rock matrix (Stead et al., 2001). For instance, Eberhardt et al. (2004) and Eberhardt (2008) were among the first to present discontinuum modelling of initiation and development of massive failures in natural rock slopes, focussing more specifically on the effect of rock bridges fracturing. The kinematic mechanisms and fracture propagation in large open pit mines were also investigated (Elmo et al., 2009), assessing the reliability of standard slope stability analysis methods in 2D and 3D. Later, combined remote sensing techniques were combined with 3D discrete element analysis to assess the instabilities on a quarry in Italy (Francioni et al., 2014), presenting and discussing the advantages and disadvantages of using realistic 3D surfaces coupled to a 3D geomechanical model.

In this section, DFN-DEM modelling was applied to study the collapse of a wedge that occurred on an open pit wall in an Australian coal mine. The high wall of the coal mine was surveyed by the CSIRO using stereo photogrammetry although the process here described is compatible with the use any high resolution topographic data (*e.g.* laser). The wedge was first characterised geometrically using digital mapping and imported into the geomechanical model, *i.e.* the DEM. The model was calibrated based upon the available data characterising the joints and the intact rock properties. Failure was then simulated and analysed from the original collapse case, testing two different types of rock, one very weak rock and another one moderately strong rock, according to the classification done by

Hoek and Bray Hoek and Bray (1981). For further reference, they are identified as weak and strong sandstone, respectively. The failure surface as defined in the digital mapping was used to validate the predictions of these models.

For additional analysis, the original DFN was modified and even totally removed to assess the dependence of the failure mechanism on the structure and the mechanical properties of the rock mass.

4.2 Case study

A 3D image of the failure surface was first built from photogrammetric data acquisition performed after the wedge collapse (Elmouttie et al., 2012). Visible geological structures could be identified directly on the 3D image and mapped as polygonal surfaces (4.1). The analysis of the failure surface led to the identification of two distinct joints as being responsible for the wedge formation. The beds on the wall are made up of conglomerates, breccias and pebbly sandstones to siltstones and the dominant material between the coal seams consists of coarse to fine sandstones (Elmouttie et al., 2012).

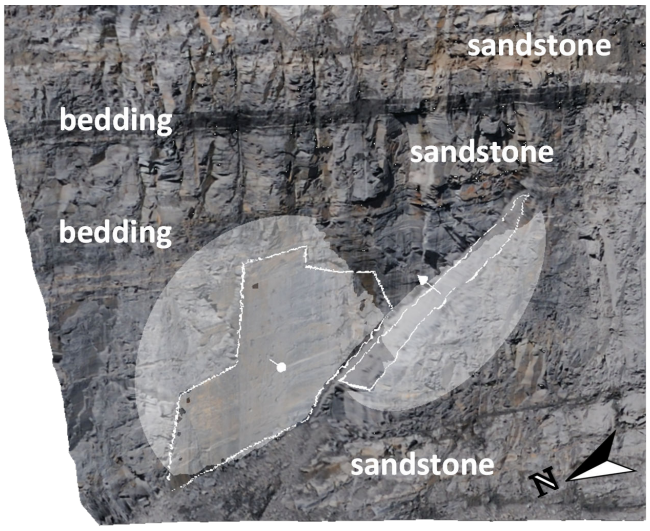

Figure 4.1: Wedge failure in a high wall

Close inspection of the 3D image revealed that this was not a simple wedge failure. Indeed, intact rock failure had occurred towards the bottom of the wedge as suggested by the difference in the rock surface appearance at this location (Figure 4.2). Using a polyhedral model analysis, the presence of the unstable block was correctly identified but did not register as a hazard, since the wedge is kinematically constrained by its intact

rock base, *i.e.* presence of a rock bridge. This example illustrates the limitations of polyhedral models to assess stability when composite failure mechanisms are involved (Elmouttie et al., 2012). In order to overcome this deficiency, a DFN-DEM modelling was thus carried out, focusing on this specific part of the wall.

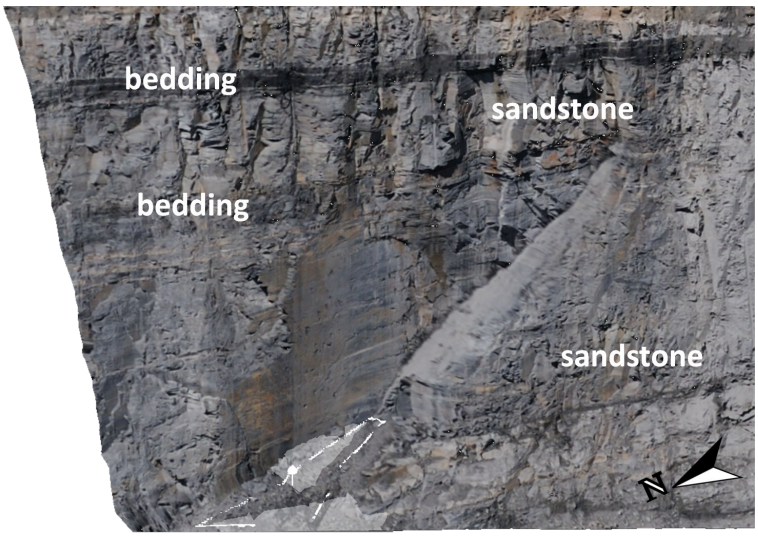

Figure 4.2: Rock failure at the toe of the wedge outlined with a white polygon at the lower part of the figure

The wall, mainly made up of sandstone, has been extensively characterised through laboratory tests (Elmouttie et al., 2012). The database provides the mechanical properties of a large quantity of samples taken in different zones of the wall, presenting a high variability in the mechanical properties between samples. Ideally, this variability can be represented in the modelling either deterministically (through the use of accurately defined domains) or, more likely through stochastic representation for rock mass properties. Given the computational demands of the DEM methods, an alternative approach was carried out here to study a limited number of scenarios.

In this work, the possibility of using the high resolution photogrammetric data representing the failure surface to validate two likely scenarios representing the aforementioned data was investigated. These scenarios represent the weakest sandstone and strongest sandstone respectively. The laboratory-scale properties of both sandstones used in this study are listed in Table 4.1.

parameter	weak rock	strong rock
Density (kg/m^3)	1,900	2,300
Young's modulus E (GPa)	3	10
Poisson's ratio ν(-)	0.2	0.3
Tensile strength (MPa)	1	5
Compressive strength UCS (MPa)	8	50

Table 4.1: Laboratory-scale properties of the rock matrix for weak and strong sandstones

4.3 Structural model

Some geometric simplifications were performed to facilitate the modelling. In particular, the high wall and discontinuities were represented as planar surfaces. The volume used for the numerical model is constrained by the surface built using photogrammetric techniques (Figure 4.3a). The DFN used for the post-failure analysis includes two polygonal surfaces whose orientations were assigned according to the structural analysis (Figure 4.1). Each surface represents a pre-existing discontinuity inside the rock mass. The one on the left has a dip angle of 85° and is oriented N 23 W, the one on the right has a dip angle of 45° and is oriented N 113 E.

This DFN geometry assumes that the persistence of the two discontinuities is sufficiently large to create the hazardous wedge and to constrain its stability to the presence of the rock bridge at its toe. This simplification neglects the presence of other geological structures, such as bedding planes, to focus the analysis on the failure of the rock bridge only. One consequence of this simplification is that heterogeneity in rock strength, both within the wedge and surrounding rock mass, is neglected and the observed fragmentation of the wedge (with part of the structure remaining in the high wall) has not been captured in the modelling process (Figure 4.3b).

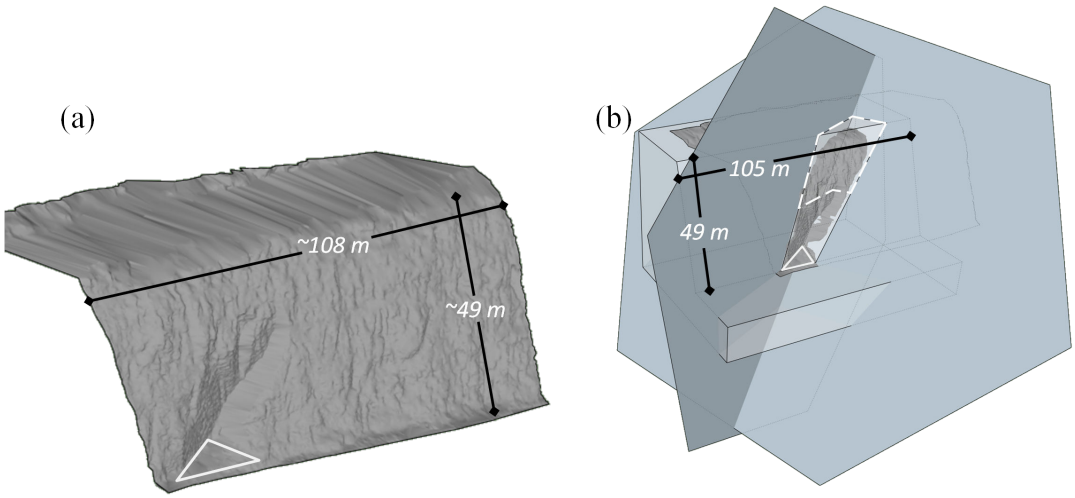

Figure 4.3: 3D geometric model and associated DFN used for the numerical simulations. (a) The surface of the wall built by photogrammetry and (b) the DFN and the volume used for simulations, merged with the surface of the wall, showing the constrained wedge (right). The idealised rock bridge is highlighted with the white triangle

4.4 Numerical model

DEM was chosen in this study for its capability to model the progressive failure of the rock matrix (Donzé and Magnier (1995); Potyondy and Cundall (2004)). The simulations were carried out using Yade Open DEM, an extensible open-source software for discrete numerical modelling (Kozicki and Donzé (2008); Kozicki and Donzé (2009)). The intact rock is represented by an assembly of bonded discrete elements (DE, also referred as particles). Each inter-particle bond obeys elastic-brittle behaviour in both normal and tangential directions. Under external loading, the bonds can break either by tension or shear failure mechanisms following a modified Mohr-Coulomb criterion with a tensile cut off (see Scholtès and Donzé (2013) for details).

The micro-cracks resulting from bond breakage can coalesce one with another to form macro-fractures. The model was calibrated based upon the properties measured by point load index tests and uniaxial compressive tests carried out on-site. Usually, the rock mass strength is assumed to be considerably reduced as the sample size increases. According to Hoek and Brown (1980), the uniaxial compressive strength UCS_d of a rock specimen with a diameter of d mm can be related to the uniaxial compressive strength UCS_{50} of a 50 mm diameter sample by the following relationship:

$$UCS_d = UCS_{50} \left(\frac{50}{d} \right)^{0.18} \tag{4.1}$$

A scaling factor of 0.6 was consequently applied to the strength measured at the laboratory in order to take into account the scale effect at the metre-scale. Consequently, the aforementioned UCS values of 8 and 50 MPa were scaled to obtain the $UCS_{1,000}$ values of 3 and 30 MPa, for the weak and the strong sandstones respectively. The properties of both sandstones are summarised in Table 4.2.

parameter	weak sandstone	strong sandstone
Volumetric mass density (kg/m^3)	1,900	2,300
Young's modulus E (GPa)	3	10
Poisson's ratio ν(-)	0.2	0.3
Tensile strength TS (MPa)	0.6	3
Compressive strength UCS (MPa)	5	30
Cohesion (MPa)	1.4	6.4
Friction angle (°)	31.1	42.5

Table 4.2: Macroscopic properties of the rock matrix for weak and strong sandstones

To reproduce the behaviour of these two sandstones, a calibration of the model was carried out to determine the related DEM parameters. The elastic properties and the strength of the simulated rock are determined by performing uniaxial tensile and compressive tests, as well as triaxial tests simulations.

In the present DEM model, the non-linearity of the failure envelope and the ratio between the tensile strength and the compressive strength of both types of sandstone is controlled by the number of interaction forces per DE, (which controls the degree of interlocking, see Scholtès and Donzé (2013) for details) which can be set by defining a given interaction range coefficient that allows for near neighbour interaction. The larger this coefficient is, the larger the number of interaction forces and the more cohesive the material is. On the contrary, if the coefficient is close to one, the simulated material represents a granular fabric and behaves as a weak rock.

The DEM parameters used to simulate the macroscopic responses of the weak and the strong sandstones are summarised in Table 4.3. The stress-strain curves obtained by uniaxial tensile and compressive tests simulations are plotted in Figure 4.4 for both types of sandstone. The predicted failure envelopes for weak and strong sandstone and the related stress-strain curves are presented in Figure 4.5. A linear fit between the axial stress and the confining stress from the Mohr-Coulomb criterion allows for the estimation of the friction angle of the rock material (Hoek and Brown, 1997).

No experimental data was available for the joint properties. They were described on-site as clay-coated and weak where there has been significant oxidation. A friction angle of 20° was then assumed in the model And such an assumption was deemed acceptable given the goals of this research were to demonstrate the use of high resolution failure surface data to validate model selection. However, discontinuity surface properties can represent a significant source of uncertainty in the geomechanical modelling process.

Discontinuities are explicitly included in the DEM model by using the smooth joint model (SJM), which ensures a constitutive mechanical behaviour of the discontinuities (Cundall et al. (2008); Mas-Ivars et al. (2011); Scholtès and Donzé (2012)). The SJM formulation consists in reorienting each inter-particle interaction intersecting the discontinuity plane, according to its surface orientation, in order to avoid the dependence of the behaviour on the model discretisation and on the DE shape (see Scholtès and Donzé (2012) for details). The joint behaviour was calibrated through direct shear tests simulations. The stress–strain curves obtained for constant normal loads σ_n ranging from 0.25 to 1.5 MPa are shown in Figure 4.6 along with the associated failure envelope. The SJM formulation ensures a direct equivalence between the macroscopic properties and the bond-scale properties. Therefore, a calibrated inter-particle friction angle equal to 20° leads to a macroscopic friction angle of 20°.

parameter	weak sandstone	strong sandstone
DEM density (kg/m^3)	3,390	4,110
Bond normal stiffness (GPa.m)	$6\bar{D}^*$	$18\bar{D}^*$
Bond shear/normal stiffness ratio(-)	0.45	0.35
Bond tensile strength (MPa)	1	3.8
Bond cohesion (MPa)	8	38
Bond friction angle (°)	13	15
Number of contact per DE (-)	8	10
Interaction range coefficient (-)	1.02	1.13

**the harmonic mean of the interacting particles diameters Scholtes and Donze* (2013)

Table 4.3: Bond-scale properties of the rock matrix for weak and strong sandstones

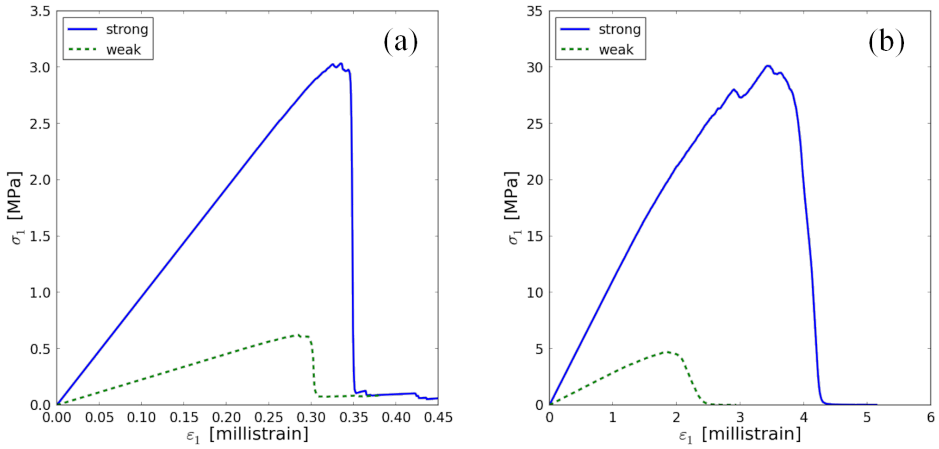

Figure 4.4: (a) stress–strain curves obtained from uniaxial tensile and (b) compressive test simulations performed on the rock matrix for the average and maximum values calibrated to the weak and the strong sandstones respectively

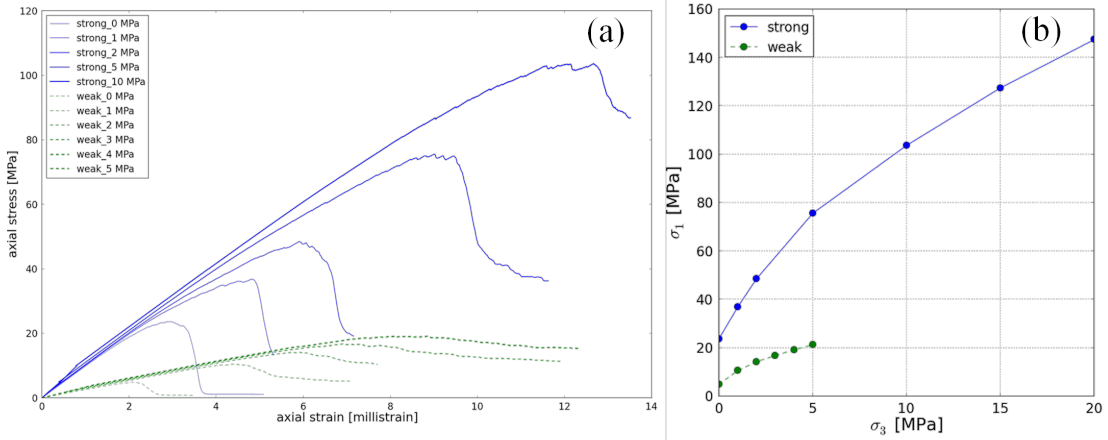

Figure 4.5: (a) stress–strain curves obtained from triaxial test simulations with the corresponding confining stress given on the top left corner and (b) the predicted failure envelopes for the strong and the weak sandstones

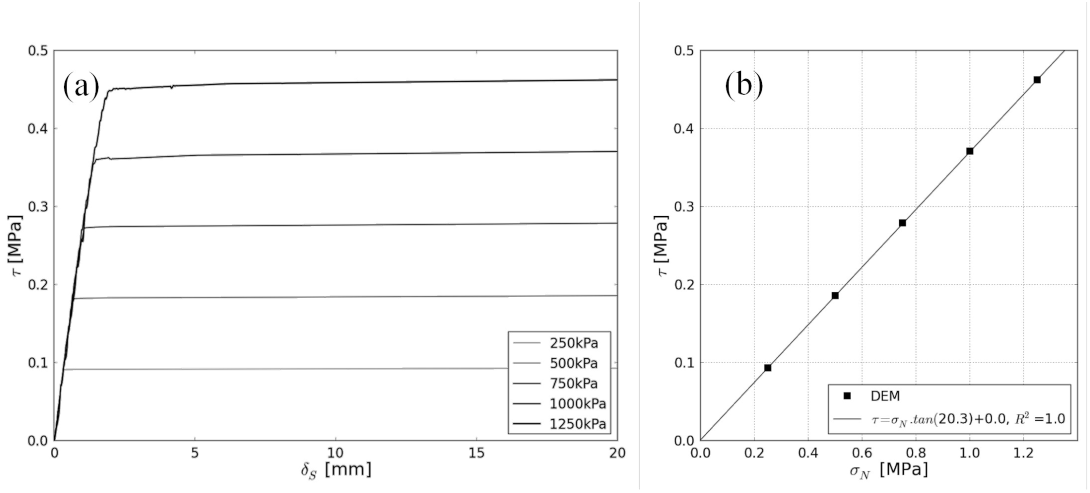

Figure 4.6: (a) Stress–strain curves obtained from direct shear test simulations performed on the calibrated model under a constant normal load σ_n ranging from 0.25 to 1.5 MPa. τ is the shear stress and δ_s is the shear displacement of the joint and (b) the corresponding predicted failure envelope for the rock joint

4.5 Strength reduction method

In the presence of rock bridges, the slope model can remain stable after the application of initial stress conditions induced by gravity loading. In this case, a strength reduction method – the tensile and shear strength reduction (TSSR) method – was performed in order to trigger failure (Bonilla-Sierra et al. (2015); Bonilla–Sierra et al. (2015)). The TSSR method involves the progressive and simultaneous decrease of both the tensile strength and the cohesion of the inter-particle bonds making up the rock matrix while the properties of the joins remain unchanged. Acting at the particle scale, the TSSR method contributes to decrease progressively the macroscopic tensile and compressive strengths of the simulated rock material. Eventually, as a result of this degradation process, failure occurs at locations where the material is no longer able to sustain the loading.

The progressive failure of the rock mass can be tracked by monitoring the spatio-temporal distribution of the micro-cracks, appearing as the material strength decreases. Finally, a failure surface can be determined from the location of the micro-cracks inside the model.

In this study, the slope model was first stabilised by applying gravity in order to initialise the *in situ* stress conditions. It is necessary to adjust the volumetric mass density from the macroscopic scale to the bond-scale (see Table 4.2 and 4.3), based on the difference in porosity between the real rock and the DE assembly, in order to ensure an equivalent stress field inside the model. Then, the rock matrix strength was gradually reduced by iteratively applying the TSSR method every 1,000 iterations until failure occurred. The strength reduction factor is defined as follows (Bonilla-Sierra et al., 2015):

$$TSSR = \frac{current\ strength}{initial\ strength} \tag{4.2}$$

The TSSR factor is decreased iteratively until an unstable DE volume is detected in the model. This unstable volume is calculated at each iteration step and is defined as the volume of particles which experience a velocity higher than 1 cm/s. From the numerical simulations applying the TSSR factor to cases with similar discretisation, it has been observed that the model is irreversibly destabilised once the velocity of the DE exceeds this threshold.

Defining V_p as the volume of a particle, the quantity of $1{,}000V_p$, which is around 10% of the volume of the wedge, has been set as the threshold value, in order to determine a coherent limit for the unstable value and control the simulation. When the volume of particles with velocity higher than 1 cm/s is greater than this threshold, failure is said to occur and the TSSR is no longer applied.

4.6 Results

4.6.1 Stability analysis

In Figure 4.7, the evolution of the unstable volume and the strength reduction factor is plotted as a function of the simulation time, for both types of sandstone. Before the TSSR factor was applied, the system went through a stabilisation phase under the application of the gravity force. Once the entire volume was stabilised, *i.e.* the unstable volume was nil, the TSSR was then iteratively applied until failure occurred (black curve in Figure 4.7). Before failure, indicated by a vertical black dashed line in Figure 4.7, the volume destabilised briefly every time the TSSR was applied. However, the model reached a new equilibrium state before the next strength degradation was applied.

In parallel, the amount of micro-cracks occurring during the simulation was recorded. As soon as the rock strength was reduced to 3.2% and 23.7% of their initial values for the strong and the weak sandstones respectively, the number of micro-cracks located at the toe of the wedge started to increase dramatically and kept increasing as failure occurred (Figures 4.8 and 4.10). For both types of sandstone, notwithstanding the differences in their strengths, the location of the initial fracturing pattern was in a good qualitative agreement with the observation made on field.

As shown in Figure 4.9 and 4.11, failure developed as a result of the coalescence of micro-cracks propagating upward from the toe of the wedge in both cases, with a larger process zone for the strong sandstone because of the greater interlocking effect. The number of micro-cracks was also higher in the strong sandstone model than in the weak sandstone model, due to higher density of initial cohesive bonds. As a consequence, micro-cracks started to appear at the front part of the wall surrounding the wedge. The initiation and further propagation of the micro-cracks at the toe of the wedge triggered the destabilisation of the whole block.

As expected, the total unstable volume corresponded to the entire wedge volume, which is around 3,200 m^3, as seen in the lower right of Figure 4.9 and 4.11.

The failure mechanisms driving the destabilisation of the wedge seem to be comparable for both weak and strong sandstones. To highlight the similarity in the failure pattern for both, a side view of the velocity field is plotted after failure in Figure 4.12, showing the wedge sliding towards its base.

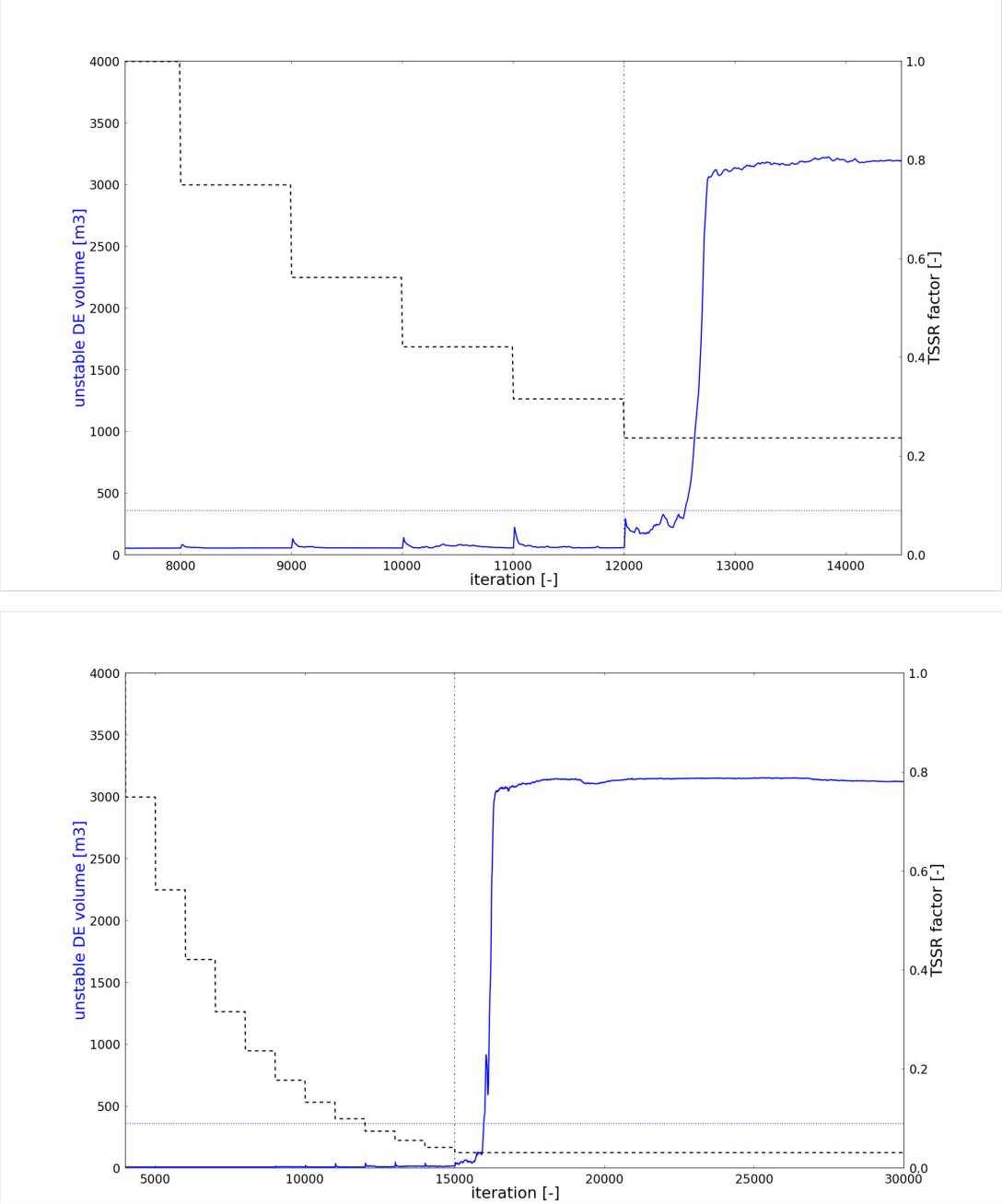

Figure 4.7: The TSSR factor (black dashed curve) and the evolution of the unstable volume (blue continuous curve) as a function of the iteration numbers for the weak sandstone (top) and strong sandstone (bottom). The threshold volume is shown with the horizontal blue dashed line. The vertical black dashed line delimits the iteration at which failure occurred

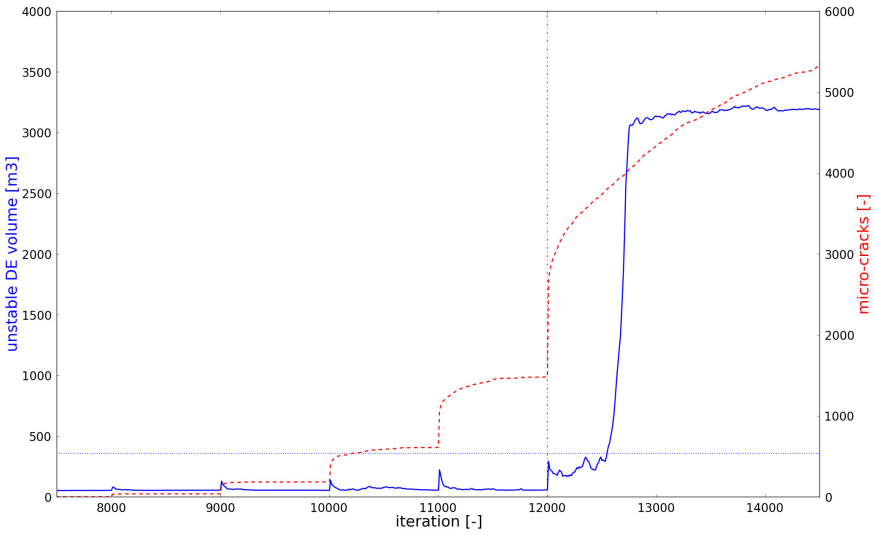

Figure 4.8: For the weak sandstone, the evolution of the unstable volume (blue continuous curve) and the cumulative amount of micro-cracks (red dashed curve) as a function of the iteration numbers. The threshold volume is shown with the horizontal blue dashed line. The vertical black dashed line delimits the iteration at which failure occurred

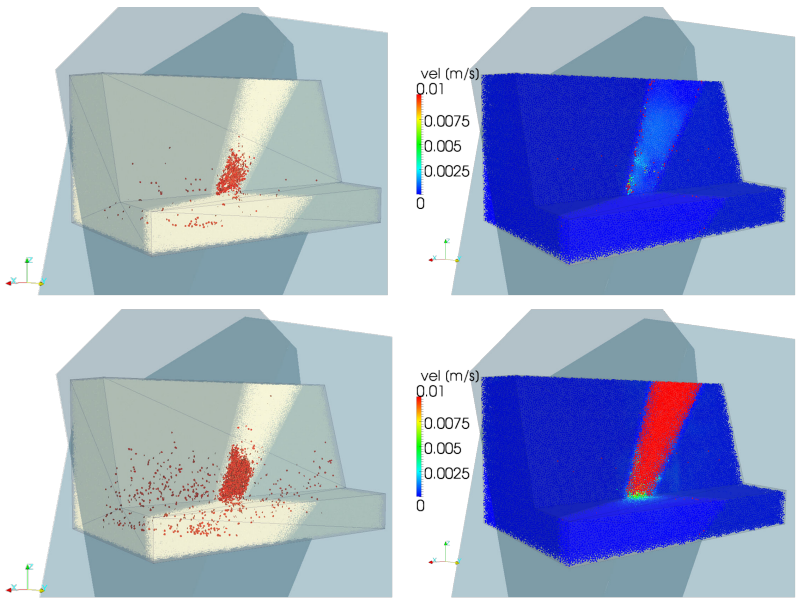

Figure 4.9: 3D view of the weak sandstone model. On the top, the micro-cracks (left) and the velocity field (right) at 12,000 iterations. On the bottom, the micro-cracks (left) and the velocity field (right) at 13,000 iterations

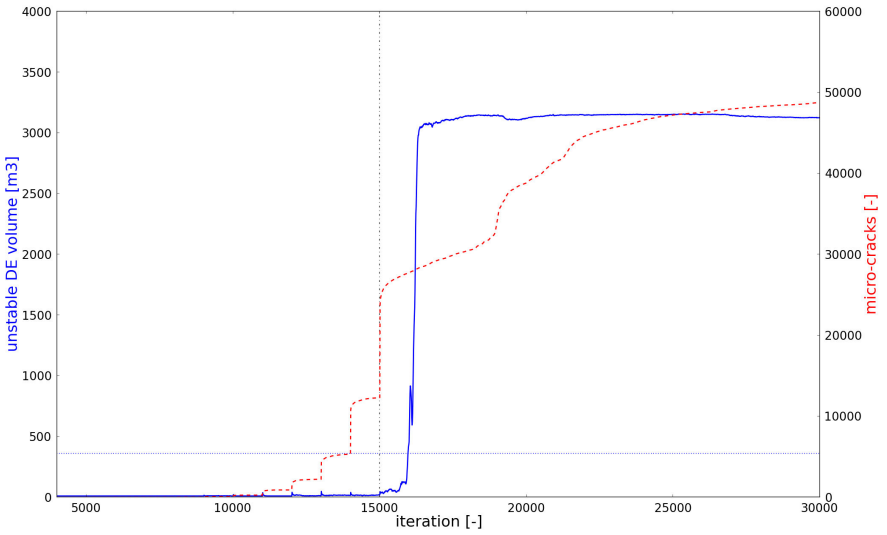

Figure 4.10: For the strong sandstone, the evolution of the unstable volume (blue continuous curve) and the cumulative amount of micro-cracks (red dashed curve) as a function of the iteration numbers. The threshold volume is shown with the horizontal blue dashed line. The vertical black dashed line delimits the iteration at which failure occurred

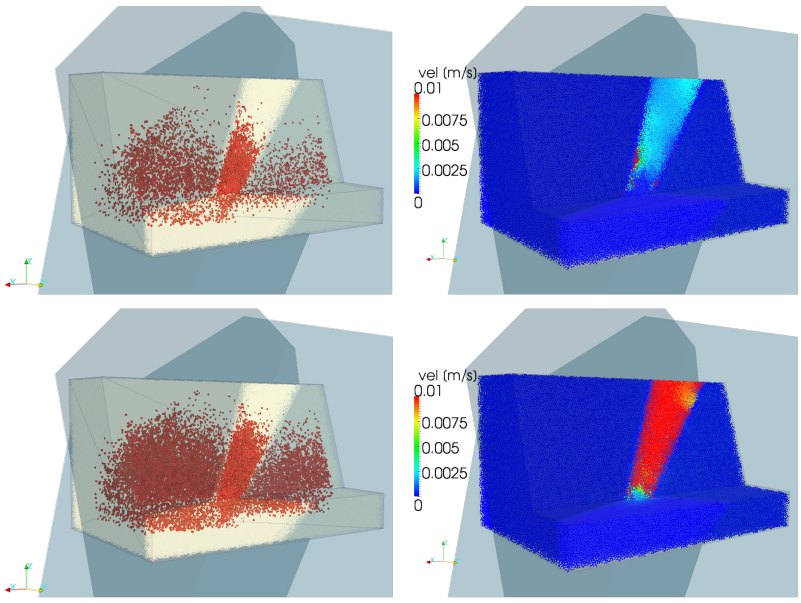

Figure 4.11: 3D view of the strong sandstone model. On the top, the micro-cracks (left) and the velocity field (right) at 15,000 iterations. On the bottom, the micro-cracks (left) and the velocity field (right) at 16,000 iterations

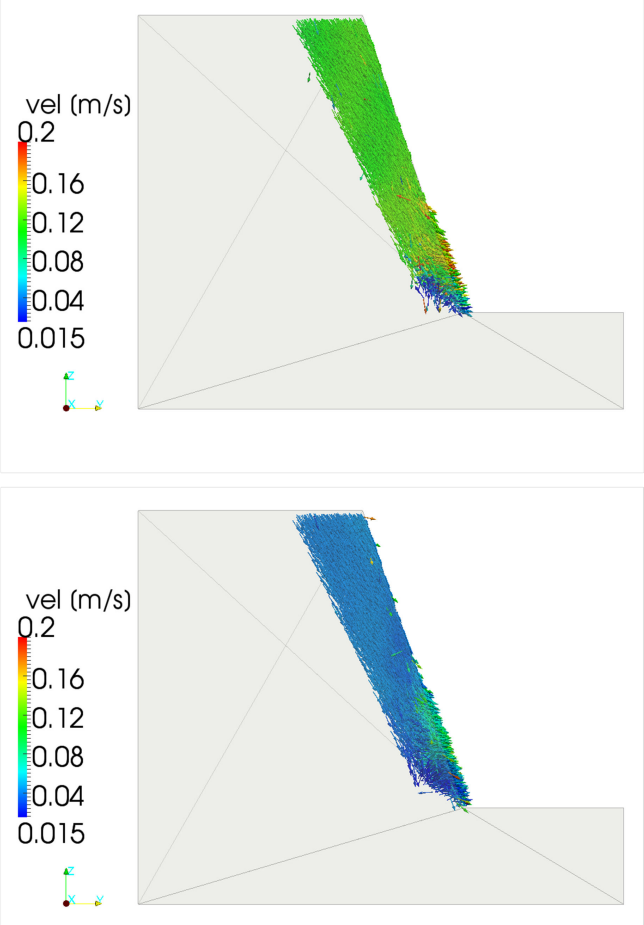

Figure 4.12: Vertical cut of the velocity vector field plotted for the weak sandstone at 14,000 iterations (top) and for the strong sandstone at 17,000 iterations (bottom)

4.6.2 Failure surface identification

In the DFN-DEM model, macro-fractures result from the coalescence of micro-cracks (Scholtès and Donzé, 2015). The micro-cracks located at the toe of the wedge were thus isolated in order to identify only the failure surface (Figure 4.13). As mentioned in the previous section, the number of micro-cracks is lower in the weak sandstone model. The consequence is a difference in the density of the micro-cracks at the toe of the slope for each case. Nevertheless, the localisation of the failure surface was very similar for both cases (Figure 4.13).

The micro-cracks form a point cloud which convex hull can be computed using any mesh-processing software. The convex hull is defined as the boundary of the minimal convex shape that contains the given set of points. In 3D, the convex hull is a convex

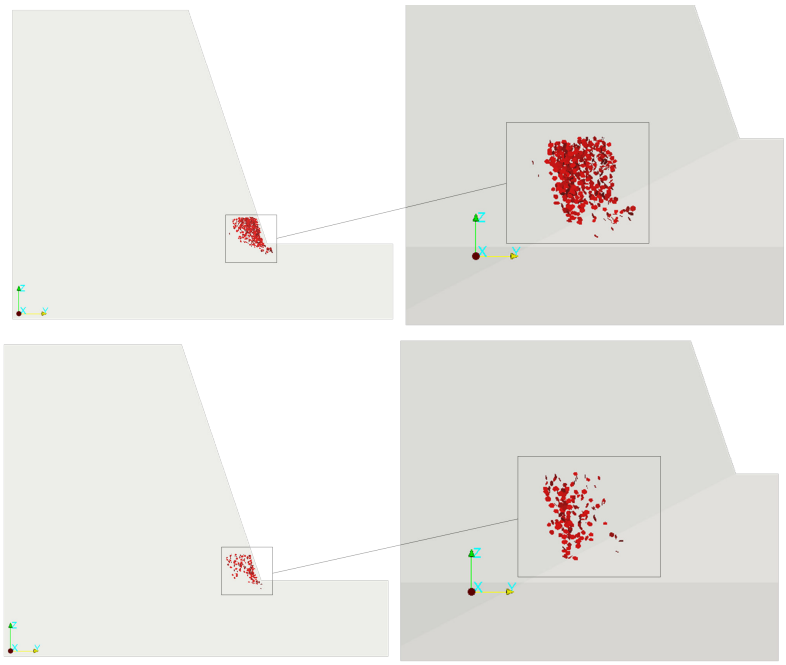

Figure 4.13: Point cloud representing the micro-cracks appearing at the toe of the wedge for the strong sandstone after 14,000 iterations (top) and for the weak sandstone after 11,000 iterations (bottom)

polyhedron (de Berg et al., 2008). The polyhedron can then be meshed using triangulation techniques over its constitutive points.

From the resulting volume, the failure surfaces for both weak and strong sandstones could thus be extracted as the lower boundary of the polyhedron. Since the numerical model was created within the same geo-referencing system used to generate the 3D image, the failure surfaces extracted from the numerical simulations could be directly superimposed on the original 3D surface built using photogrammetry. As observed in Figure 4.14, a good qualitative agreement is found between the numerical predictions and the actual failure surface.

For further analysis, a quantitative comparison between the simulated and observed failure surfaces was performed by calculating the minimum distances between the simulated micro-crack locations and the best-fit plane to the failure surface (Table 4.4). Despite a quantitative agreement, some discrepancy arises in the dip direction of the simulated data. This discrepancy can be observed in Figure 4.15, where the generated micro-cracks (in red) are superposed over the location of the actual failure surface, represented by its contour (in blue). We attribute this to the relatively sparse point cloud used to fit the failure surface in the model. This difference might be reduced by increasing the density of the DE assembly used in the simulations.

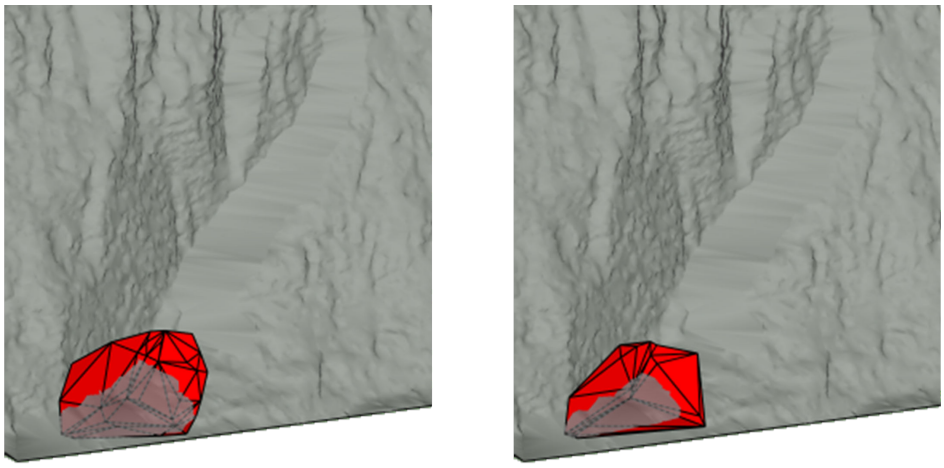

Figure 4.14: Failure surface (in red) superposed to the high wall surface, for the strong sandstone (left) and for the weak sandstone (right)

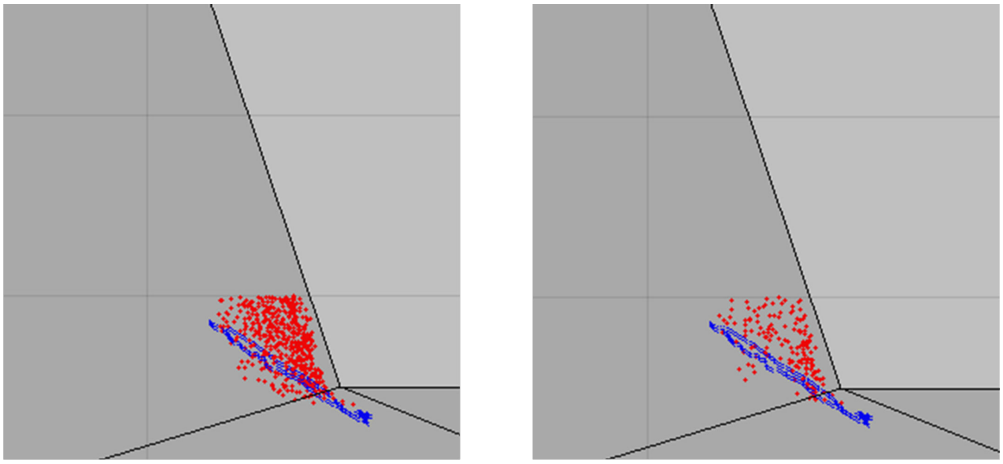

Figure 4.15: Superposition between the simulated micro-cracks (in red) and the observed failure surface (point cloud in blue), for the strong sandstone (left) and for the weak sandstone (right)

parameter	simulated surface (strong sandstone)	simulated surface (weak sandstone)	observed 3D surface
Number of cracks in analysis	16	9	NA
Best-fit-plane orientation (dip/dip direction ±2°)	22/011	24/008	30/005
Exposed area of failure surface ($\pm 5m^2$)*	46	38	50
Average distance of simulated to observed surface (±1m)	0.59	0.36	NA

*$Calculated\ by\ projecting\ simulated\ failure\ surface\ onto\ observed\ best-fit-plane\ and\ computing\ area\ of\ convex\ hull$

Table 4.4: Summary data comparing the simulated and observed failure surfaces

The high resolution photogrammetric data of the failure surface was found to be consistent with both modelled scenarios. The potential to use the surface to discriminate between these scenarios still exists but it would require a higher DEM resolution. This would provide a greater number and more densely spaced micro-crack data to support comparison of observed and simulated failure surfaces.

A back analysis was carried out taking into account two different types of sandstone, respectively weak and strong. The final unstable volume was similar for both sandstones, and was equal to the total volume of the wedge constrained by the discontinuities. Qualitatively, it was observed that the failure mechanism was controlled by the geological structures considered in the model rather than by the mechanical properties of the rock. Note that the local strength (*i.e.* at the bond-scale) at failure was different comparing both cases. The strength of the strong sandstone had to be reduced up to 3.2% of its initial value in order to trigger failure, which is around eight times lower than the TSSR factor needed to destabilise the wedge in the case of the weak sandstone model. For instance, at the bond-scale, the final local tensile strength for the weak sandstone was 0.24 MPa and the final local cohesion was 1.92 MPa which corresponds to a reduction of 23.7% of their initial values. For the strong sandstone, the final local tensile strength was 0.12 MPa and the final local cohesion was 1.2 MPa. These differences at the bond scale can be explained by the difference in the degree of interlocking between the two types of rock; more contacts per DE lead to higher decrease in their strength in order to reach the critical state.

We can therefore confirm that, given the model assumptions and simplifications used in this study, the weak sandstone model provides consistent results with the weathered rock strength properties identified in the field.

4.7 Influence of the rock bridge size

The detachment of the wedge resulted from stress concentration at the toe of the wedge, where the rock bridge was located. In this particular case, the failure mechanism and the associated unstable volume seem to be strongly controlled by the geometry of the discontinuities that constrain the rock bridge to a reduced area located at the toe of the wedge. To investigate the contribution of the DFN on the failure surface geometry, some selected configurations were simulated.

4.7.1 The modified structural model

In the original case study, the area at the toe is estimated to be only 2.5% of the total surface area of the wedge, highlighted in red in Figure 4.16a. In this particular case, it has

been observed that the failure mechanism and the unstable volume were likely controlled by the DFN configuration. By considering a different structural model, and therefore a larger area for the rock bridge, a different mechanical response may be expected. To do so, the DFN was pushed back inside the slope, increasing the area of the rock bridge to 9% of the total surface area of the wedge as observed in Figure 4.16b. The dip and dip direction of the discontinuities were kept unchanged.

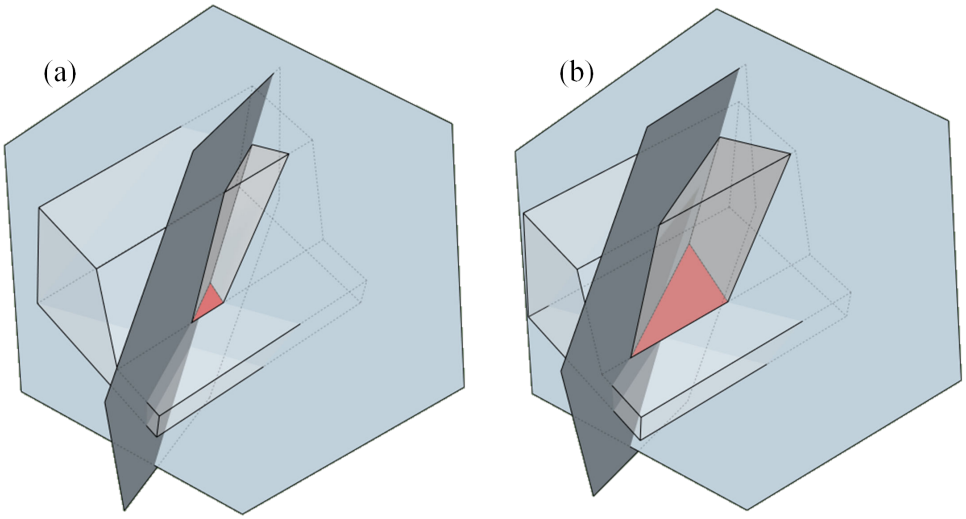

Figure 4.16: Idealised rock bridge surfaces. (a) The original DFN with 2.5% of the total surface of the wedge as rock bridge and (b) the modified DFN with 9% of the total surface of the wedge as rock bridge

4.7.2 Failure mechanism

Simulations were run using the modified DFN for both strong and weak sandstones and the results were compared with the original configuration described previously. The same TSSR method was applied in order to trigger failure.

For both the weak and strong sandstones, the collapsing volume can be identified and located through the velocity field at failure. To visualise the failure mechanisms, a vertical cut of the velocity field is plotted for both sandstones (Figure 4.17).Contrary to the original case study, the mechanical properties of the rock appeared to have here an effect on the failure mechanisms of the wedge. For the weak sandstone, a circular slip surface, typical of weak homogeneous slopes, can be distinguished (Figure 4.17, top). This behaviour results from the mechanical properties of the simulated medium. Indeed, a small degree of interlocking (DE interaction radius equal to 1.02) and a friction angle

equal to 31.1°, correspond to weathered rock masses or soil-like materials which are prone to circular failure (Wyllie and Mah, 2004). On the other hand, the strong sandstone has a larger degree of interlocking (DE interaction radius equal to 1.13), and a friction angle equal to 42.5°. Then, the failure surface looks stepper and deeper than in the case of the weak sandstone, as shown in Figure 4.17 (bottom).

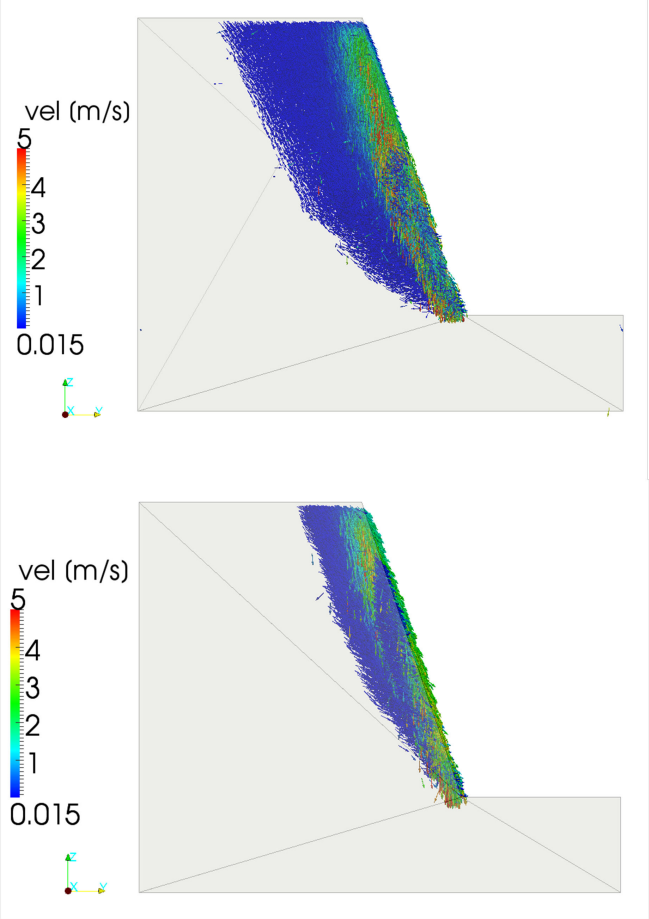

Figure 4.17: Vertical cut of the velocity field plotted for the weak sandstone at 31,000 iterations (top) and for the strong sandstone at 38,000 iterations (bottom)

The influence of the mechanical properties of the rock material on the failure mechanisms was investigated. It was shown that although the structural features constrain the resulting unstable volume, they did not control the failure mechanism. The volume mobilised depends on the strength of the sandstone. For the strong sandstone, the total volume of the wedge was partially destabilised, and its failure surface is shallower and steeper than the one observed for the weak sandstone. For the latter, the entire volume of the wedge failed along a circular failure surface.

4.8 Stability of homogeneous rock masses

The importance of pre-existing structures was studied and it has been found that, depending on the size of the rock bridge, the failure mechanism and the mobilised volume may vary if the mechanical properties of the rock are modified. To conclude the analysis on the mechanical properties of the rock and its effect on rock slope stability, the DFN was removed, in order to study the behaviour of the intact slope as a function of the nature of the rock material.

The TSSR method was applied in the same way as it was applied for the two previous cases. The unstable volume calculated 3,000 iterations after failure for the weak sandstone was around 6,400 m^3 and tended to increase during the simulation time. The velocity field at that moment of the simulation is shown in Figure 4.18a. A curved failure surface can be identified from the vertical cut of the velocity field presented in Figure 4.18b.

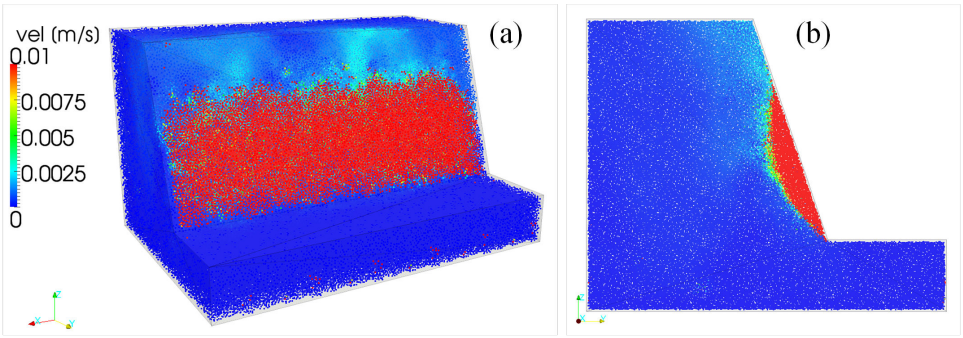

Figure 4.18: For the weak sandstone, the velocity field plotted at 20,000 iterations (a) 3D perspective view and (b) a centred vertical cut

In comparison to the weak sandstone, the unstable volume recorded at 3,000 iterations after failure for the strong sandstone was 3,300 m^3, which is two times lower. In Figure 4.19, the velocity field registered at that moment shows that the unstable volume for the strong sandstone was distributed at an equivalent height on the slope face as for the weak sandstone. Nevertheless, the depth of the failure surface is less important.

In presence of pre-existing discontinuities, failure surface can be controlled by the location and the orientation of the geological features. In the absence of DFN, only the material strength has an impact on the failure mechanism. For both types of sandstone, the unstable volume was homogeneously mobilised along a shallow circular surface, with differences in the depth and height depending on the mechanical properties of the rock. The failure observed for the weak sandstone presents a deep radius surface, in contrast with the shallow surface observed for the strong sandstone.

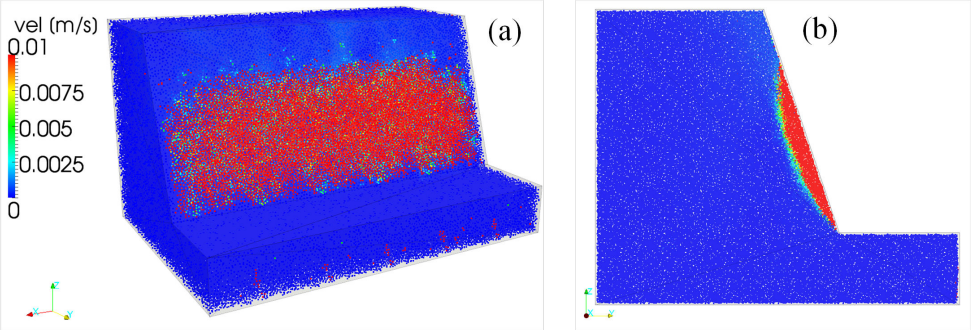

Figure 4.19: For the strong sandstone, the velocity field plotted at 24,000 iterations (a) 3D perspective view and (b) a centred vertical cut

4.9 Discussion on the influence of the rock bridge size

The mechanical response of an open pit wall was studied under three different geometric scenarios, using two types of material respectively calibrated to weak and strong sandstones. In the first scenario, the original DFN configuration constrained the rock bridge to a small area (2.5% of the total surface area of the wedge). In the second scenario, the DFN configuration was slightly modified to increase the size of the rock bridge up to four times its original area. In the third scenario, the DFN was removed and the analysis was done focusing only in the influence of the mechanical properties of the rock matrix.

The ratio between the unstable volume and the total volume of the model (DE volume) is plotted in Figure 4.20, as a function of the ratio between the rock bridge area and the total surface area of the wedge. When the rock bridge is small (original DFN), the entire wedge is mobilised. When the rock bridge is larger or when there is no DFN, the mobilised volume is higher for the weak sandstone than for the strong sandstone. However, in the case of the enlarged rock bridge, the mobilised volume is still constrained by the DFN, as 100% of the wedge volume collapsed for the weak sandstone, whereas 70% of the wedge collapsed for the strong sandstone. Due to the drastic strength reduction needed to trigger failure, areas surrounding the lower left part of the wedge were also destabilised. To summarise, the unstable volume is strongly controlled by the presence of the discontinuities that constrain the size of the rock bridge. As their configuration is modified, increasing the size of the rock bridge, the material properties remain the predominant factor controlling the stability.

Regarding the TSSR factor, *i.e.* the strength reduction needed to be reduced to trigger failure, the strength of the strong sandstone was reduced to lower values than the strength of the weak sandstone in all the cases. At the bond-scale, this is explained by the difference in the degree of interlocking between the two types of rock; more contacts per DE lead

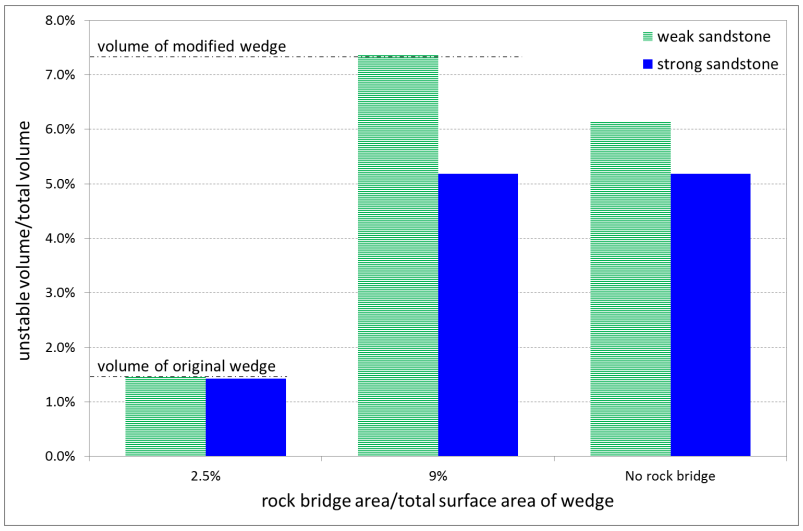

Figure 4.20: Relationship between the unstable volume and the size of the rock bridge at the toe of the wedge

to higher decrease in their strength in order to reach the critical state. For both types of sandstone, the TSSR factor at failure decreased as the size of the rock bridge increased and is similar to the factors obtained in the absence of DFN, as observed in Figure 4.21. This can be explained by the fact that when the size of the rock bridge increases, the proportion of intact rock that assures the stability increases, and thus the rock strength has to be reduced to a lower value in order to destabilise the model. The decrease rate is also higher for the weak sandstone, indicating that mechanically, this one is more affected by the presence of structural features.

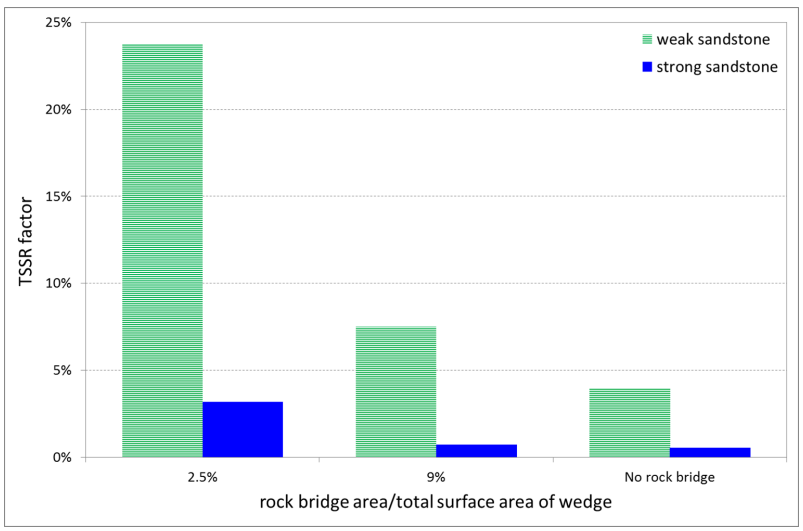

Figure 4.21: The dependence of the TSSR factor on the presence and size of the rock bridge at the toe of the wedge

4.10 Conclusion

The stability of an open pit high wall was assessed considering different scenarios. Each scenario relied on photogrammetric data used to build the structural model of the high wall and for validation of the simulated failure surfaces. The study focused on a particular area of the wall where a wedge collapsed.

A kinematic analysis based on polyhedral modelling showed that the wedge would remain stable because of the presence of a rock bridge at its base. DFN-DEM modelling was thus used to model the progressive failure of this kinematically constrained wedge.

Two types of sandstone were calibrated and used in the model, labelled weak and strong, to take into account the high variability of the on-site characterisation.

A strength reduction method, *i.e.* the TSSR method, was applied to simulate the progressive failure of the wedge. The coalescence of the micro-cracks propagating inside the model provided a simulated failure surface that was compared against the failure surface measured in the field using high resolution photogrammetric data. The difference of strength between the weak and the strong sandstones showed to have no impact on the location or orientation of the simulated failure surface and both were consistent with field measurements. Furthermore, to investigate the effect of the mechanical properties of the rock on the failure mechanism and on the failure surface prediction, the DFN was modified in order to increase the size of the expected rock bridge. In this particular case, the coalescence of the micro-cracks could not provide a specific failure surface either for the weak sandstone or for the strong sandstone. The failure mechanism could be observed by assessing the unstable volume and the velocity field that showed differences in the way the wedge was mobilised depending on the strength of the material. In the case of the weak sandstone, a circular failure surface could be observed. For the strong sandstone, a shallow surface could be identified on the face of the wall. Moreover, it has been seen that the mechanical response of the weak sandstone was more affected by the presence of the structural features than the strong sandstone.

The proposed method has potential to validate modelling parameters such as rock strength models. A limiting factor is the discretisation of the modelling process which can complicate comparison and interpretation of the simulated failure surface. with the use of high resolution topographic data of a failure surface.

4.11 Acknowledgements

The authors are grateful to Philip Soole and Paul Maconochie for the acquisition of the photogrammetric data used in this study. The authors are also grateful to Nathan

Ferdinands and Dave Edwards for providing site access and support at the mine. Brett Poulsen and Andy Wilkins are thanked for their fruitful discussions. This work has been supported by the IMSRN French Company through a CIFRE grant N°2012 / 0710 and CSIRO Energy Flagship, QCAT in Australia. The laboratory 3SR is part of the LabEx Tec 21 (*Investissements d'Avenir* - grant agreement n°ANR-11-LABX-0030).

General conclusion

An advanced method for rock slope stability analysis was proposed based on DEM numerical modelling. This modelling technique can be adapted to gather the actual mechanical behaviour evidenced on natural and engineered rock slopes. Two principal elements were included in the modelling such as *i)* non-persistent discontinuities and *ii)* intact rock bridges. The effect of these elements on the stability of fractured rock masses was investigated.

The DEM formulation was chosen for modelling fractured rock masses due to its ability to reproduce progressive failure mechanisms which are inevitable when non-persistent discontinuity planes are presented in the rock mass. These discontinuity planes can be explicitly taken into account into the numerical model. In consequence, both sliding along pre-existing discontinuities and fracturing of rock bridges located in between these discontinuities can be simulated to reproduce mixed failure mechanisms which cannot be tackled by conventional methods. Mapped discontinuities and slope geometry were generated by photogrammetric techniques. These features were processed to build up the structural model of the rock slope, which was then used as input into the numerical model to carry out the stability analysis.

The proposed method introduces the tensile and shear strength reduction (TSSR) method. The TSSR method can be applied to simulate the strength reduction of the rock matrix, in order to trigger the failure of the slope. The coalescence of the micro-cracks propagating inside the rock matrix enable to simulate failure surfaces, which can be compared to actual failure surfaces observed on site. Furthermore, the effect of the mechanical properties of the rock on both the failure mechanism and the failure surface prediction could be investigated. This numerical analysis can quantify the significance of the DEM discretisation for the interpretation of micro-cracks generation in the context of

failure surface prediction.

Differences have been observed regarding the mobilised volumes depending on both the initial mechanical properties of the rock and the size of the rock bridge. When the rock bridge corresponded to a small area compared to the total unstable volume, the failure surface as well as the mobilised volume could be relatively well predicted. On the contrary, when the rock bridge increased in size, the coalescence of micro-cracks could not be used to identify a well defined failure surface. In addition, it was shown that the mechanical properties played a major role in the failure mechanism. Indeed, a soil-like failure surface could be observed for the case of a weak rock, whereas a shallow planar surface appeared on the slope face for a more competent rock. To summarise, the pertinence of the proposed DFN-DEM modelling for prediction of failure surfaces under configurations observed in natural slopes and open pit mines could be confirmed. The method shows promise as a tool for the numerical modelling of slope stability phenomena, specially when progressive failure mechanism are involved.

Furthermore, probabilistic techniques were combined with numerical modelling to analyse the translational failure of a jointed rock slope in presence of rock bridges. Numerical simulations were performed using a simplified configuration involving a single failure plane containing both frictional joints surfaces and cohesive rock bridges in order to simulate the progressive failure of the slope and to obtain the critical equivalent cohesion needed to ensure stability. The validity of Jennings' formulation was discussed for different distributions of rock bridges along the failure surface as well as for different locations of the centre of gravity of the block. Despite the simplicity of the geometrical model, it has been shown that Jennings' prediction could be retrieved for failure surfaces with low dip angles, *i.e.* 30°, where failure occurs mainly through shear mode. For joints with higher dip angles (typically superior to 50°) and for which failures occur through a combination of tensile and shear modes, Jennings' formulation underestimates the critical equivalent cohesion value. Indeed, for specific cases where the centre of gravity is located in the lower part of the sliding block and for dip angle equal to 70°, failure is mainly driven by tensile mode. In consequence, it could be shown that the validity of Jennings' formulation is limited as soon as tensile failure becomes predominant and an alternative formulation was then proposed to assess the equivalent strength.

Based on the results obtained from this research project, further work is suggested to investigate more complex probabilistic distribution of rock bridges and their impact on the stability of rock masses. In this context, the stochastic generation of discontinuities can be included in the DEM model. Enhanced probabilistic techniques may strengthen the DFN-DEM methodology applied for real rock slope stability analysis, providing more reliable results. The output could be considered as a valuable tool for geotechnical and geomechanical analysis.

The potential of DFN-DEM approach to predict failure surfaces should be further in-

vestigated. This particular result may provide an important insight on both the involved failure mechanisms and the identification of unstable blocks. Alternative methodologies could be proposed to reconcile better discretisation of DEM models (*i.e.* highest DE resolution) with interpretation of finer resolution field photogrammetric data for the validation of numerical failure surface predictions.

Annexe A: Testing photogrammetry packages for rock slope reconstruction

Abstract

Photogrammetry has become a valuable technique to build up models of rock slope used in structural analysis. Recent software packages have greatly improved the algorithms for data extraction and image reconstruction, providing an straightforward method to create realistic and accurate three-dimensional (3D) surfaces from good quality overlapping two-dimensional (2D) photographs. The objective of this work was to assess the performance of some representative 3D reconstruction software applied to topographical 3D modelling. The scope was to identify the main features, accuracy advantages and limitations of each package and to compare the results obtained from a set of photographs taken under controlled conditions. Two dataset were collected from digital photographs taken from a chosen slope situated in the Bastille hill, in Grenoble (France). The photographs were taken with a digital camera Canon EOS 5D Mark II using a lens Canon EF 50 mm $f/1.4$ USM. This evaluation evidenced the relative simplicity of using some commercial and non-commercial packages, as well as it explained the importance of gathering quality images under controlled light conditions and accurate metric measurements.

Introduction

Three-dimensional (3D) models have become a valuable tool for geotechnical and geomechanical analysis, due to their capability to provide a realistic representation of rock slopes. There are several methods for creating 3D models, such as 3D scanning, 3D rendering and

image-based modelling. This latter is also known as photogrammetry. Photogrammetric technique is able to generate accurate 3D models from a set of static two-dimensional (2D) images.

Several commercial photogrammetry packages are available for non-expert users to create automatically 3D models from 2D images. With such software, 2D photographs from a chosen scene are processed, following an automatic workflow. That workflow generally includes the 3D reconstruction done by plotting out key points on the photograph to give the software a sense of scale and proportion within the 3D image. Afterwards, these points and data can be exploited by the program to create a realistic 3D model of the object (Wiesen and Bailey, 2013).

An evaluation of selected software, which provide facilities to create 3D models oriented to geological and geotechnical analysis, is presented in this report. A 10×10 m^2 zone of rock slope was chosen, based on the possibility to find good light conditions and visibility. This test site is located in the Bastille hill, in Grenoble (France).

Short overview on the tested software

Two type of photogrammetry software were tested, regarding their availability. First, stand-alone commercial packages such as Agisoft PhotoScan Pro (Agisoft, 2013), Pix4UAV Desktop (Pix4D, 2012), Smart3D Capture (Acute3D, 2012) and Sirovision (Sirovision, 2010). Second, web-based software such as Autodesk 123D Catch (Autodesk, 2013) or Cubify Capture (3DSystems, 2013).

Autodesk 123D Catch, Cubify Capture Beta, Smart3D Capture and Agisoft PhotoScan Pro are software that use the so-called structure from motion (SFM) approach. This image-based approach, derived from computer vision (CV), is capable to automatically perform the whole pipeline process reducing time both of images orientation and also 3D reconstruction (Favalli et al., 2012). With the SFM approach, a significant number of images can be oriented without any knowledge of the camera parameters and model geometry. The images orientation is performed by identifying the common feature points through appropriate recognition operators. The scale invariant feature transform (SIFT) is a common operator used in CV due to its capability to provide the correspondence between images taken from different positions, with different scales and different illuminations. The camera parameters can be estimated during the matching phase, or self–calibration process.

On the other hand, Sirovision is the only software that performs pair-wise approach to determine the spatial location of a cloud point from two or more 2D overlapping images, to create then the 3D image by integrating visual data. Additionally, the software includes a helpful system for interpreting structures directly on the generated 3D surface.

It is known that CV technique targets preferentially on process automation rather than on precision and accuracy (Barazzetti et al., 2010). This condition can be disadvantageous when the purpose of the 3D survey is modelling with good metric accuracy and associated orientation (georeferencing). This point was discussing by comparing the only two software that support georeferencing process: Sirovison and Agistoft PhotoScan Pro.

Agisoft PhotoScan Pro

Agisoft PhotoScan Pro is a 3D reconstruction software, which operates with arbitrary images and it can be efficient in both controlled and uncontrolled conditions (e.g. light, position, amount of images). The program provides robust photo alignment, although the images are taken from any position, providing a fair 3D model from at least two photos. Both image alignment and 3D model reconstruction are fully automated. This software presents the following processing steps (Agisoft, 2013):

1. Feature matching across the photos: at the first stage Agisoft Pro detects points in the source photos that are stable under viewpoint and lighting variations. Then it generates a descriptor for each point based on its local neighbourhood. These descriptors are used later to detect correspondences across the photos. This is similar to the SIFT approach, but uses different algorithms for higher alignment quality.

2. Solving for camera intrinsic and extrinsic orientation parameters: Agisoft Pro uses an algorithm to find approximate camera locations and refines them later using a bundle-adjustment algorithm.

3. Dense surface reconstruction: at this step several processing algorithms are available. *Exact*, *Smooth* and *Height-field* proposed methods are based on pair-wise depth map computation, while fast method utilises a multi-view approach.

4. Texture mapping: at this stage Agisoft Pro parametrises a surface possibly cutting it in smaller pieces, and then blends source photos to form a textured surface.

Autodesk 123D Catch (Former Photofly)

123D Catch is a beta online program from Autodesk that allows the use to upload images to Autodesk servers where the data is processed, providing then a fair 3D model to the user. This web service is based on the program Smart3D Capture (Kersten and Lindstaedt, 2012). All the models created are property of Autodesk, therefore, they are not

supposed to be used for commercial purposes. Nguyen et al. (2012) defines the reconstruction approach, whereas Courchay et al. (2010) describes the fundamental algorithms of this software.

Cubify Capture Beta (Former Hypr3D)

Cubify Capture is a beta version of the former online program Hypr3D, which generates 3D images by analysing multiple 2D photographs of the same object, taken from different angles. Cubify Capture is able to digitally reconstruct the 3D object and produce a 3D scene Nguyen et al. (2012). It requires several images of the same object from different perspectives with sufficient overlap.

Pix4UAV Desktop 3D

Pix4UAV is a software package with an emphasis on automatic digital elevation model (DEM) and ortophoto production that combines thousands of aerial images into professional accurate 2D maps and 3D models (Petrie, 2013). It is principally used to provide aerial photography in the mining industry, for civil engineering, precision farming and urban areas modelling. The processing is done on the desktop and creates 2D and 3D models. It contains a post-processing mosaic editing and a measurement tool. Strecha (2011) presents the following processing steps:

1. The software searches for matching points by analysing all images. An improved version of binary descriptors proposed in Strecha et al. (2012) is used. The descriptors are powerful enough to match key points quickly and accurately.

2. The matching points, as well as the approximate values of the image position and the orientation, are used in a bundle block adjustment to reconstruct the exact position and orientation of the camera for every acquired image.

3. Based on the position and orientation reconstruction, the matching points are verified and their 3D coordinates calculated. The reference is the world geodesic system 84 (WGS84), based on global positioning system (GPS) measurements.

4. The 3D points are interpolated to form a triangulated irregular network in order to obtain a DEM.

5. The DEM is then used to project every image pixel and to calculate the georeferenced orthomosaic (also called true orthophoto).

Sirovision

Sirovision is a geological and geotechnical mapping tool integrated to an analysis system designed to generate accurate, scaled 3D images of rock faces from stereo-photographs. It was developed to supply support to open pit and underground environments operations. Sirovision is the only photogrammetry software, among the ones here tested, that supports the mapping and analysis of structural features, useful to geologists, geotechnical engineers, surveyors and mine engineers. Sirovision implements 3D imaging using passive stereo-photogrammetry based on triangulation (Poropat, 2001).

Smart3D Capture

The acquisition step with Smart3D Capture has almost none shooting constraints, and the processing step can be performed within minutes or hours. The technique is based mainly on correspondence image details and focus producing models that resemble the original 3D scene from a sequence of calibrated or non-calibrated photographs. The concept supporting this technique, is the extraction and combination of information from several overlapping images taken from distinct locations at different instants to produce the relations between those images, *i.e.* SFM approach. The software performs the following steps (Acute3D, 2012):

1. Photo-groups generation: the software organises the photographs into one or several photo-groups, considering shots under the exact same conditions, for example same physical camera, same focal length, *etc.*

2. Aerotriangulation: this is the process of determining the relative and absolute position of each photograph in a dataset, based on photogrammetry algorithms.

3. Control points: may be included if the exact GPS coordinates of remarkable points in the scene, with their respective position, were surveyed in at least two photographs. In absence of control points, the reconstruction processing can continue normally.

Automatic vertical orientation of 3D models

A Canon EOS 5D Mark II camera was used to perform this software test. Indistinctly of which software was used to process the data, the resulting 3D models were vertically well oriented. The software were able to recognise automatically the natural position of the object modelled due to the accelerometer that is included inside the camera.

The principal function of the accelerometer is to map the device position, *i.e.* the reference axis, in relation to the real world. It measures the gravitational forces applied

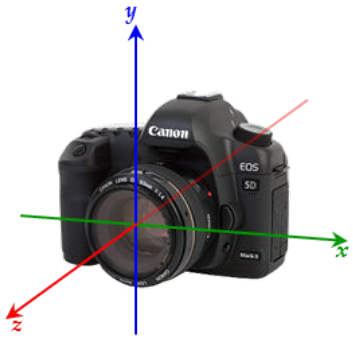

Figure A.1: Three axis system in a device

in the three axis (Figure A.1), which are expressed in terms of the gravitational constant (G unit). The acquired data provides support to determine the camera position, for example whether is leaning forwards facing the ground or leaning backwards and facing the sky (Graça et al., 2012). The orientation information is saved into the exchangeable image file format (EXIF), which stores the photograph attributes Hass (2008).

Data acquisition

All images were taken in an outdoor environment, under natural light conditions. The lens used was a Canon EF 50 mm $f/1.4$ USM without any filter. The size of the image is 11 megapixels and was registered as JPEG format.

Dataset 1 is the initial set of images, shown in Figure A.2. It consists of five photographs taken along the slope with one meter of separation distance, focusing and centring on the same reference point (point 1, see Figure A.4) and keeping the same distance to the slope. A tripod was used to control the steadiness of the camera. Besides that, the shooting mode was set in manual to control all the characteristics of the image.

Initially, the right reference photograph, **Rphoto192**, was positioned and taken, and then one meter to the left, the left reference, **Lphoto202**. Additional photographs, **Bphoto204** and **Cphoto203**, were located at one and two meters respectively to the left of **Lphoto202**; photograph **Aphoto205** was positioned one meter to the right of image **Rphoto192**. Refer to A.2 to see the photographs distribution.

Dataset 2 (Figure A.3) consists of photographs taken randomly, also along to the slope, but under uncontrolled conditions, *i.e.* no tripod support, automatic shooting mode was chosen, random centre of the image was used and unmeasured distances between shots and also to the slope.

The following camera settings are resumed for each photograph in Figure A.2 and A.3:

Size, which is the photograph dimensions given in pixels. **FL** is the focal length. **ISO** is the ISO Speed, which is a measurement of sensitivity. **Tv** is the shutter speed. **Av** is the aperture priority.

	C_photo_203	B_photo_204	L_photo_202	R_photo_192	A_photo_205
	C_photo_203	B_photo_204	L_photo_202	R_photo_192	A_photo_205
Size	4080x2720	4080x2720	4080x2720	4080x2720	4080x2720
FL	50 mm	50 mm	50 mm	50 mm	50 mm
ISO	800	800	800	800	800
Tv	1/160	1/160	1/160	1/160	1/160
Av	8.0	8.0	8.0	8.0	8.0

Figure A.2: Dataset 1 of the slope



photo 194		photo 195	photo 196
Size	4080x2720	4080x2720	4080x2720
FL	50 mm	50 mm	50 mm
ISO	100	100	100
Tv	1/50	1/60	1/60
Av	3.2	3.5	3.5



photo 197		photo 198	photo 199
Size	4080x2720	4080x2720	4080x2720
FL	50 mm	50 mm	50 mm
ISO	100	100	100
Tv	1/60	1/60	1/60
Av	3.5	3.5	3.5

Figure A.3: Dataset 2 of the slope

Five points were identified on the cliff with an assigned number for each one. Distances from the camera positions to each point on the cliff were measured, using both tape and laser range-finder TruPulse 200B. The measurements accuracy made using the tape, is estimated to ± 5 cm. For the laser, the constructor specifications guarantees a maximum error of ± 30 cm at 1,000 m. Nevertheless, a study carried out by Farve (2010), has shown that for a distance of around 12 m, the accuracy of the TruPulse was ± 5 cm. In the presented case, the distance between the measurement point and the target is in average 6 m, the laser accuracy is then sufficient and comparable to the tape accuracy. The measured distances and the comparison between measurement methods are presented in Figure A.4.

To scale the 3D image created using Autodesk 123D Catch and Smart3D Capture, distances between the reference points were measured and are shown in Figure A.5. These distances were used also to verify the accuracy of the 3D models. The verification is later explained in this report. Since models generated using Sirovision and Agisoft PhotoScan Pro could be georeferenced, they were automatically scaled.

Georeferencing method requires at least three ground control points (GCP), expressed in a consistent georeference system. The position of the right reference photograph was used to take the measurements with the laser, pointing straight to each point on the cliff. The GCP coordinates were later calculated using the gathered data (Table A.1), as well as the tape measurements (Figure A.5). In Table A.1, HD is the horizontal distance, VD is the vertical distance and SD is the slope distance, expressed all in m.

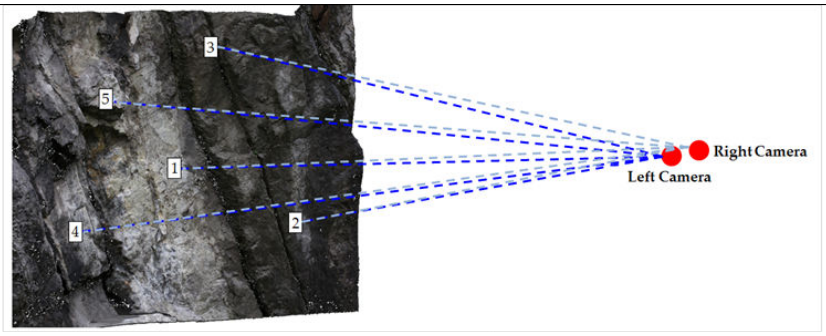

Distance	Right Camera			Left Camera		
	Decameter [m]	Laser [m]	Difference [%]	Decameter [m]	Laser [m]	Difference [%]
C-1	5.93	6.1	3%	6.10	6.1	0%
C-2	5.84	5.9	1%	6.30	6.2	2%
C-3	5.91	6.0	2%	5.98	6.1	2%
C-4	6.21	6.3	1%	6.70	6.1	10%
C-5	5.98	6.1	2%	5.70	6.0	5%

Figure A.4: Distances measured from camera position to the points on the slope surface

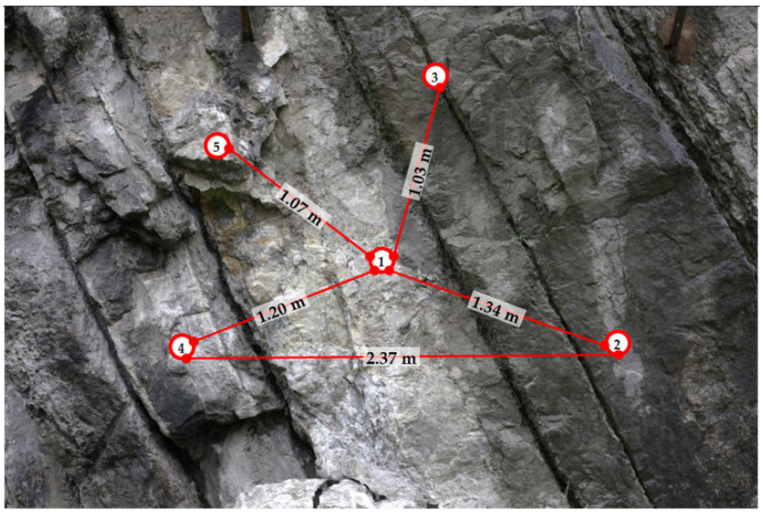

Figure A.5: Distances measured between points on the slope surface

GCP	HD [m]	VD [m]	SD [m]
1	6.0	0.5	6.1
2	5.9	0.1	5.9
3	5.8	1.5	6.0
4	6.3	0.1	6.3
5	6.0	1.2	6.1

Table A.1: Distances from the camera position to the GCP measured with the laser range-finder

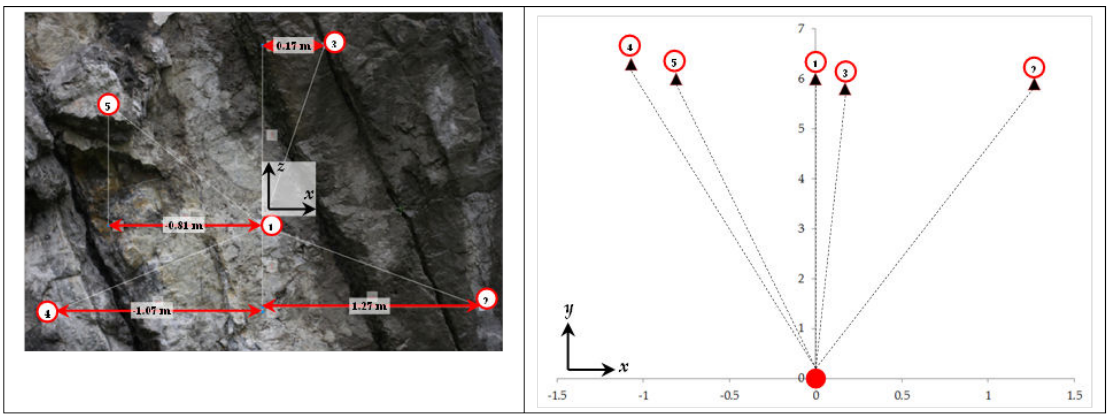

Figure A.6: Distances measured between points on the slope surface and their projections in local axis

To determine the geoposition of each point, a local system was first defined. A single 2D photograph was imported to Autocad software in order to scale the image, based on the distance between points 2 and 4 (Figure A.5). Then, it was possible to calculate the local coordinates along the x-axis (Figure A.6, left). The horizontal distances (HD) measured by the laser range-finder were used to place the points in the y-axis, with respect to the camera position (Figure A.6, right). Finally, the height in the z-axis was calculated with the measured vertical distances (VD). The calculated local coordinates are listed in Table A.2.

The geoposition of the reference right camera was measured using a GPS device, providing data with ± 10 m precision. This considerable poor accuracy may be result of the close position to a high vertical rock slope that could obstruct satellite signals. To overcome this problem, Google Earth was used to adjust the geoposition. The resulting coordinates were given in WGS84 system format (decimated degrees), and then converted into Lambert II system (metric units). The coordinates in Lambert II system are expressed in terms of *Easting*, *Northing* and *Height*, which are compatible with the Sirovison georeference system. The calculated geoposition of the reference right camera

GCP	x [m]	y [m]	z [m]
1	0.00	6.00	0.00
2	1.27	5.90	-0.40
3	0.17	5.80	1.00
4	-1.07	6.30	-0.40
5	-0.81	6.00	0.70

Table A.2: GCP coordinates in the local system

is:

- $Easting_{rightC} = 865,903.807\ m$
- $Northing_{rightC} = 2,027,346.378\ m$
- $Height_{rightC} = 217.46\ m$

The geoposition of the GCP were calculated adding the local coordinates of each point to the to the coordinates of the reference right camera, as follows:

$$Easting_{GCPn} = Easting_{rightC} + x_{GCPn} \tag{A.1}$$

$$Northing_{GCPn} = Northing_{rightC} + y_{GCPn} \tag{A.2}$$

$$Height_{GCPn} = Height_{rightC} + z_{GCPn} \tag{A.3}$$

where the subscript $GCPn$ refers to each GCP (Table A.2), and the subscript $rightC$ refers to the right camera reference position. The obtained Lambert II coordinates are listed in Table A.3.

GCP	*Easting* [m]	*Northing* [m]	*Height* [m]
1	865,903.807	2,027,352.378	217.46
2	865,905.077	2,027,352.278	217.06
3	865,903.977	2,027,352.178	218.46
4	865,902.737	2,027,352.678	217.06
5	865,902.997	2,027,352.378	218.16

Table A.3: GCP coordinates in Lambert II system

Workflow and results

The main steps to perform 3D reconstruction in order to build up accurate 3D models are presented for the different tested software. For some of them, occasional user intervention was required to choose, for example, features like mesh quality and georeferencing process.

Agisoft PhotoScan Pro

1. Adding photos: at this stage the user chose the images used to build the 3D model. At least two photographs were required.

2. Aligning photos: the program found automatically the position of the camera for each photograph and refined camera calibration parameters. Processing included detection and matching points for estimating the scene structure, resulting in a point cloud model.

3. Building geometry: the software performed the reconstruction quality parameters, *i.e.* mesh quality (total faces and hole filling improvement).

4. Building texture: After the 3D mesh was created, the program assigned intensity of texture and colour depth, to obtain a 3D model.

5. Scaling: there are two methods to scale a model. The first one is done by georeferencing using *Create Markers* tool: it is possible to identify the points on the cliff and then assign them the coordinates for each one, either using the WGS84 or metric system. The second one consists in selecting two points on the cliff and set a reference distance in m. For the present study, five Lambert II coordinate (see Table A.3) were placed on the correspondent points on the cliff (see Figure A.5), obtaining a 3D model scaled and georeferenced.

Autodesk 123D Catch

1. Creating a new photo scene: an Autodesk user account was created in their website. A minimum of three images were requested.

2. Computing photo scene: this process was completely automatic and the duration depended on the quantity of images and the quality of the internet connection.

3. Scaling: it was made by selecting two points on the cliff and determining a reference distance between them. Here, points 2 and 4 (see Figure A.5) were selected and their distance set as the reference.

4. Exporting the mesh: in order to edit and exploit the 3D model in MeshLab (open source package for mesh edition), it was necessary to export the result obtained into $*.obj$ file, which is a textured 3D mesh.

Cubify Capture Beta

1. Selecting and uploading images: an user account was created in their website. At least ten images were required.

2. Creating the model: the images were submitted. The processing time depended on the quantity of the photographs and internet speed connection.

3. The result: a $*.zip$ file was automatically created, which included the 3D mesh and its texture. Then, the model was opened in MeshLab and to be scaled. However, doing so, it lost its texture.

Pix4UAV Desktop 3D

1. Adding photos: at least three images were requested. The centre of each photograph needed to be referenced in a geodetic coordinate system, *e.g.* WGS84. Coordinates of the right image were transformed into WGS84 system and used to set up the relative positions to the other photographs.

   Unfortunately, after performing the proposed automatic workflow (point cloud densification and orthomosaic and DEM generation), the program stops and produce an incoherent model (see Figure A.7, PIX4UAV Desktop 3D model). The process was launched again, changing the latitude data with respect to the height above mean sea level (MAMSL) by the distance to the cliff (*i.e.* 6 m instead 216 MAMSL). This was done to reproduce the configuration met for a drone looking perpendicularly to the slope surface, but it did not work either.

Sirovision

1. Adding image data: the pair of photographs taken with a difference between them of 1/6 of the distance to the slope were used. In this case, the stereo-pair is composed by **Lphoto202** and **Rphoto192** (Figure A.2).

2. Building 3D image: the program automatically matched common points in the left and right images of the stereo-image pair (*Definition of task setup* and *Matching* processes), which allows subsequently the 3D image generation.

3. Georeferencing: scaling processing was made by georeferencing. 3D image was georeferenced using the data (Table A.3) obtained for the five points identified on the cliff (see Figure A.5), this process is called *Reposition using at least three GCP*.

4. Creating mosaic: in order to compare results obtained using others software, four stereo-pairs were selected for building a mosaic using the five images from dataset 1 (Figure A.2). First, four 3D images had to be created and then the program automatically merged them into a mosaic which needed to be georeferenced again, following the same process explained in step 3., *Reposition using at least three GCP*.

5. Exporting the 3D model: a high-density mesh was exported as $*.dxf$ file without texture.

Smart3D Capture

This software is subdivided into three packages as follows: Smart3D Capture Master, Smart3D Capture Engine, and Smart3D Capture Viewer.

1. Selecting input photographs: a minimum of three images were uploaded in Smart3D Capture Master.

2. Editing control points: the Master interface provided the possibility to edit control points (GCP) in order to georeference and scale the 3D model. However, this step can be skipped and continue creating the model without scale.

3. Creating aerotriangulation: the relative and the absolute position of each photograph in a dataset was determined based on photogrammetry algorithms, described in Acute3D (2012). It automatically performed a *key point extraction*, then an *initialisation of orientation* followed by the *tie points matching* and finally a *bundle adjustment*. The whole process is called (*3D coordinates refining*).

4. Job submission: this last step proposed in the Masters interface, proposed the desired format for the resulting model: $*.obj$ or $*.s3c$ file, as well as the model quality and the precision level. Once the choice was done, the Engine interface was launched and the creation process began automatically.

5. Visualising the 3D mesh: the model was generated as a $*.s3c$ file, which could be visualised using the Viewer interface. For obtaining a $*.obj$ file, it could be created in the Master interface. Then, this format could be visualised and edited using MeshLab.

Software	2 images[1]	5 images	11 images
Agisoft PhotoScan Pro			
Autodesk 123D Catch		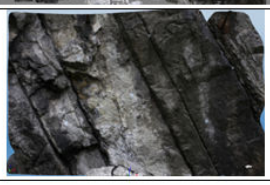	
Cubify Capture BETA	N/A	N/A	
Pix4UAV Desktop 3D	N/A		N/A
Sirovision		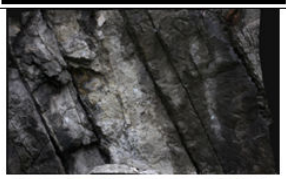	N/A
Smart 3DCapture			N/A
[1] Three images in the case of Autodesk 123D Catch and Smart 3DCapture			

Figure A.7: 3D reconstruction results

In Figure A.7, the obtained 3D models for three possible configurations are presented: *i)* using two images (three images in the case of Autodesk 123D Catch and Smart3D Capture), *ii)* using five images, *iii)* and using eleven images (dataset 1 and 2).

In Figure A.8 presents the comparisons between the texture qualities obtained for each model. Taking into account the potential interest for modelling deposit zones of rock masses in moderate slopes (low angle), detailed scenes of the observed "deposit zone" from the models built with eleven photographs (Dataset 1 and 2) are presented in Figure A.9. Here, Cubify Capture Beta produced a quite complete representation of the rock blocks.

Software	2 images[1]	5 images	11 images
Agisoft PhotoScan Pro			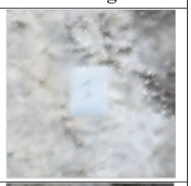
Autodesk 123DCatch			
Cubify Capture BETA	N/A	N/A	
Sirovision			N/A
Smart 3DCapture			N/A
[1] Three images in the case of Autodesk 123D Catch and Smart 3DCapture			

Figure A.8: Resolution texture detail

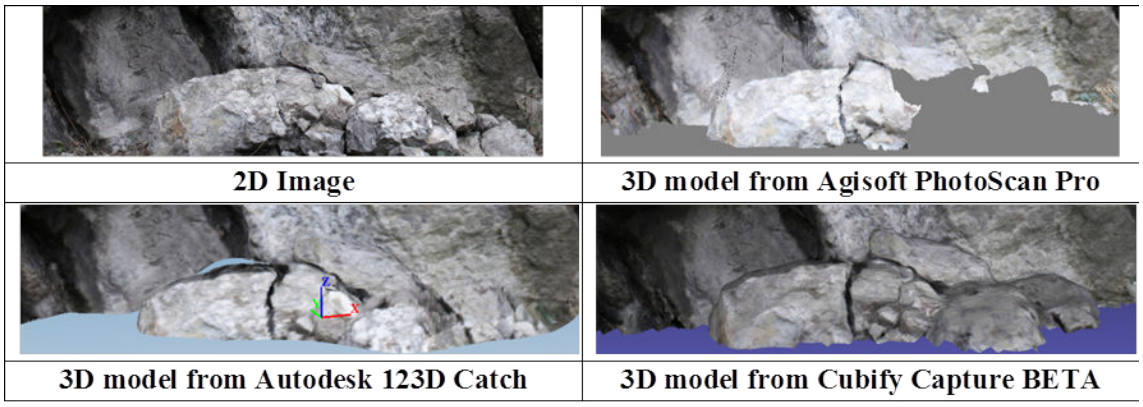

Figure A.9: Detail of the "deposit zone"

Checking the scaling process

The process of scaling the 3D models created during this test was divided in two groups. The results are summarised in Figure A.10:

1. Reposition using five ground control points (GCP), for models generated using Agisoft PhotoScan Pro, Sirovision and Smart3D Capture (three images model).
2. Setting a reference distance, for models built with Autodesk 123D Catch and Smart3D Capture (five images model). In this case, the distance between points 2 and 4 was used as the reference.

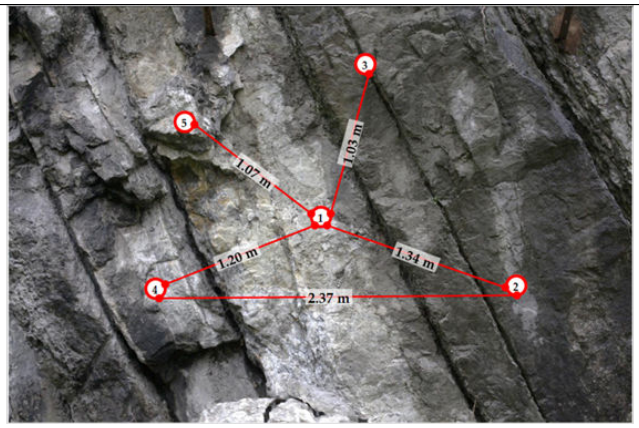

Software	Dist.	2 images[1]			5 images		
		Tape [m]	Model [m]	% diff	Tape [m]	Model [m]	% diff
Agisoft PhotoScan Pro	1-2	1.34	1.31	2.24%	1.34	1.31	2.24%
	1-3	1.03	1.02	0.97%	1.03	1.02	0.97%
	1-4	1.20	1.20	0.00%	1.20	1.20	0.00%
	1-5	1.07	1.06	0.93%	1.07	1.06	0.93%
	2-4	2.37	2.34	1.27%	2.37	2.33	1.69%
Autodesk 123D Catch	1-2	1.34	1.33	0.75%	1.34	1.33	0.75%
	1-3	1.03	1.04	0.97%	1.03	1.04	0.97%
	1-4	1.20	1.21	0.83%	1.20	1.21	0.83%
	1-5	1.07	1.08	0.93%	1.07	1.08	0.93%
	2-4	2.37	2.37	0.00%	2.37	2.37	0.00%
Sirovision	1-2	1.34	1.32	1.49%	1.34	1.33	0.75%
	1-3	1.03	1.02	0.97%	1.03	1.02	0.97%
	1-4	1.20	1.19	0.83%	1.20	1.18	1.67%
	1-5	1.07	1.06	0.93%	1.07	1.05	1.87%
	2-4	2.37	2.33	1.69%	2.37	2.34	1.27%
Smart 3DCapture	1-2	1.34	1.35	0.75%	1.34	1.32	1.49%
	1-3	1.03	1.05	1.94%	1.03	1.03	0.00%
	1-4	1.20	1.22	1.67%	1.20	1.22	1.67%
	1-5	1.07	1.09	1.87%	1.07	1.07	0.00%
	2-4	2.37	2.42	2.11%	2.37	2.37	0.00%

[1] Three images in the case of Autodesk 123D Catch and Smart 3DCapture

Figure A.10: Measurements and scale verification

Advantages and limitations

Some software characteristics are summarised taking into account the experience acquired during the test, the data found on the Internet (Wiesen and Bailey (2013), forums, Wikipedia) and also information exchanged with Pix4UAV and Smart3D Capture development representatives.

Software	Price	Camera	Photos	Ease of use[2]	Scaling procedure	Processing time[3]	Test Accuracy	Dimensionless Accuracy[4]	Field of application
Agisoft PhotoScan Pro	2 700 €	Any digital camera	≥2	Very easy	Georeferencing/ Ref. Distance	+/- 30 min	+/- 5 cm	+/- 8x10^{-3}	Archaeology, architecture, mining, animation, medicine, topographic surveys
Leica XPro	10 300 €	Leica RCD30	≥2	Not tested	Georeferencing	N/A	N/A	N/A	Mining, topographic surveys
Photomodeler Scanner	2 000 €	Any digital camera	≥2	Not tested	Reference targets	N/A	N/A	N/A	Archaeology, architecture, industrial measurements, mining, animation, medicine, topographic surveys
Sirovision	23 000 €	Specific DSLR cameras	≥2	Very easy	Georeferencing	+/- 20 min	+/- 5 cm	+/- 8x10^{-3}	Mining, topographic surveys, structural analysis included
Autodesk 123D Catch	Free	Any digital camera, smartphone[1]	≥3	Straightforward	Ref. Distance	+/- 30 min	+/- 5 cm	+/- 8x10^{-3}	Archaeology, architecture, animation, topographic surveys
Smart 3DCapture	7 500 €/year	Any DSLR cameras	≥3	Easy	Georeferencing/ Ref. Distance	+/- 30 min	+/- 5 cm	+/- 8x10^{-3}	Archaeology, architecture, industrial measurements, mining, animation, topographic surveys
Pix4UAV Desktop 3D	15 500 €	Any digital camera, smartphone[1]	≥10	Easy	Georeferencing	+/- 1 hour	N/A	N/A	Mining, topographic surveys
Cubify Capture Beta	Free	Any digital camera, smartphone[1]	≥10	Straightforward	Ref. Distance	+/- 1 hour	N/A	N/A	Archaeology, architecture, animation, topographic surveys (?)
Elcovision 10	1 500 €	Specific DSLR cameras	2-100	Not tested	Georeferencing/ Ref. Distance	N/A	N/A	N/A	Archaeology, architecture, industrial measurements, landscape planning

[1] > 5 Mpx camera.
[2] Straightforward: Upload and wait; Very easy: Intuitive and simple workflow; Easy: simple workflow.
[3] Average time from this test. Strongly depends on the quantity of images.

Figure A.11: Advantages and limitations of some photogrammetry software

Mesh superposition for 3D model comparison

Using the open-source software CloudCompare, which provides facilities to calculate distances between two point clouds, it was possible to compare the different 3D models. First, the meshes that were selected for comparison needed to be aligned using MeshLab. Here, seven common points were identified and used to align the meshes (see Figure A.12). The superposed meshes were thus exported to be sampled as a point cloud using the *Sample points on a mesh* tool provided by the software. The tool required as input data, either the number of points decided by the user or the point cloud (PC) density. The PC density was chosen to process the point cloud.

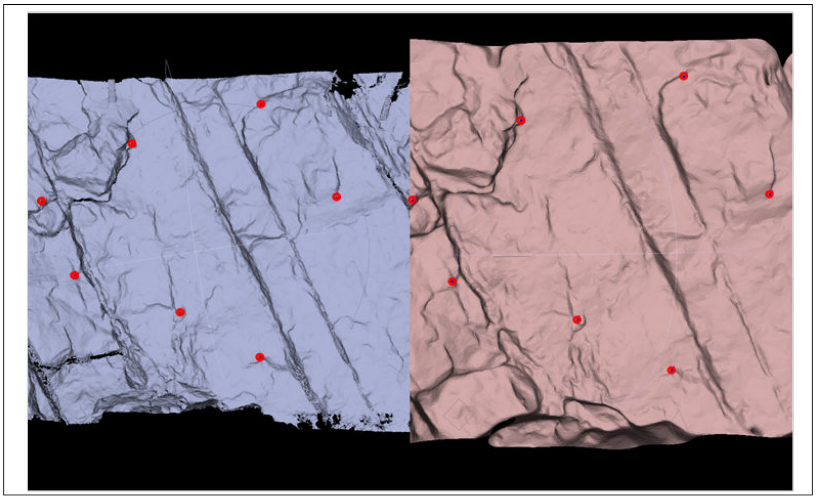

Figure A.12: Identified common points identified used to align the meshes

In CloudCompare, the PC density is calculated as a function of the mesh surface and the mean triangle surface, (*Measure surface* tool), as follows:

$$PC_{density} = \frac{mesh\ surface}{mean\ triangle\ surface} \tag{A.4}$$

Two 3D models obtained with the same software (123D Catch), but with a different quantity of images, were first compared (see Figure A.13). The accuracy was considerably good, with a mean distance between both point clouds of 1 mm.

Model	Compared	Reference
Name	VF 3 photos 123D Catch	VF 11 photos 123D Catch
Mesh surface	12.61 m^2	20.36 m^2
Mean triangle surface	3.15 E-04 m^2	7.36 E-05 m^2
PC Density	40 032	276 630
Max. Distance	0.055 m	
Mean Distance	0.001 m	

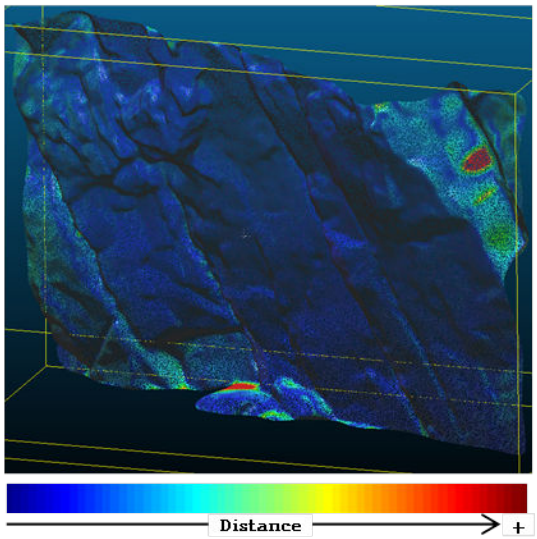

Figure A.13: Measured distances between 123D Catch models with three photos and eleven photos

In order to assess the accuracy between two software that use different scaling methods, *i.e.* reference distance and georeferencing, 3D models created with the same quantity of images were used. The comparison between 123D Catch and Agisoft PhotoScan Pro is presented in Figure A.14, and the comparison between Smart3D Capture and Agisoft PhotoScan Pro is presented Figure A.15. The calculated mean distances were around 1 cm and the maximum distances between 17 cm and 11 cm. These maximum discrepancies were localised mainly at the mesh borders and hidden areas that were not registered on the 2D image due to the camera position during the shot (See right sides of Figure A.14 and A.15).

Model	Compared	Reference
Name	VF 5 photos 123D Catch	VF 5 photos Agisoft Pro
Mesh surface	14.98 m^2	14.73 m^2
Mean triangle surface	2.59 E-04 m^2	7.36 E-05 m^2
PC Density	57 838	200 136
Max. Distance	0.17 m	
Mean Distance	0.01 m	

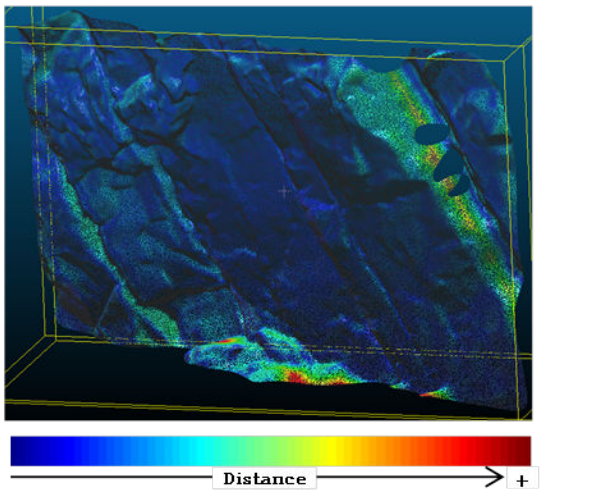

Figure A.14: Measured distances between 123D Catch model with five photos and Agisoft PhotoScan Pro model with five photos

Model	Compared	Reference
Name	VF 5 photos 3D Capture	VF 5 photos Agisoft Pro
Mesh surface	13.82 m^2	14.73 m^2
Mean triangle surface	7.45 E-05 m^2	7.36 E-05 m^2
PC Density	185 503	200 136
Max. Distance	0.11 m	
Mean Distance	0.009 m	

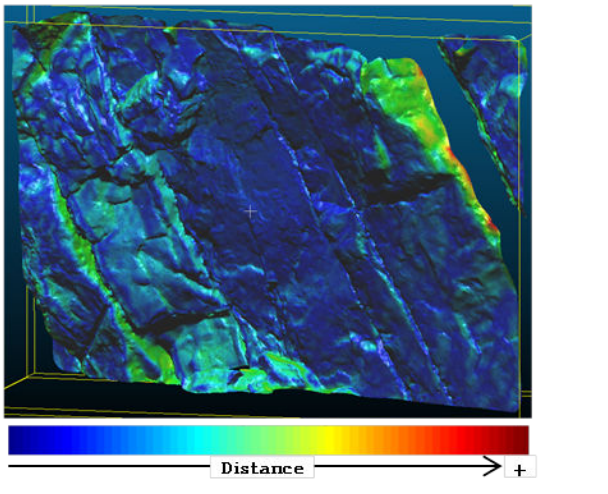

Figure A.15: Measured distances between Smart3D Capture model with five photos and Agisoft PhotoScan Pro model with five photos

Using a set of eleven photos, the comparison between Cubify Beta and 123D Catch showed a similar range of differences (Figure A.16) with a maximum distances still localised at the borders.

Model	Compared	Reference
Name	VF 11 photos Cubify BETA	VF 11 photos 123D Catch
Mesh surface	17.72 m^2	20.36 m^2
Mean triangle surface	1.89 E-04 m^2	7.36 E-05 m^2
PC Density	93 757	276 630
Max. Distance	0.06 m	
Mean Distance	0.003 m	

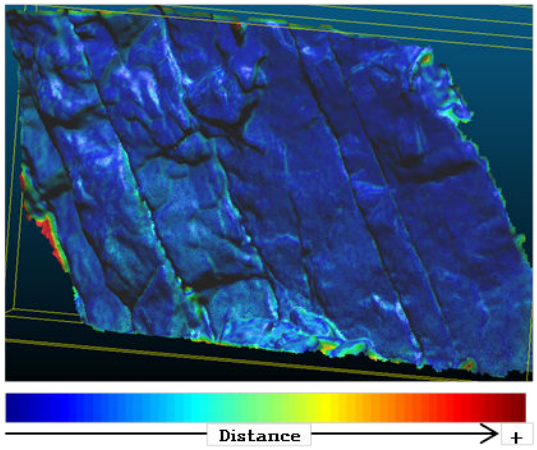

Figure A.16: Measured distances between Cubify Beta model with eleven photos and 123D Catch model with eleven photos

Comparing two software using the same reconstruction processing, such as 123D Catch and Smart3D Capture, the differences were relatively small (Figure A.17). This result provided an indirect way to validate the processing similarity between this two software.

Model	Compared	Reference
Name	VF 5 photos 3D Capture	VF 5 photos 123D Catch
Mesh surface	13.82 m^2	14.98 m^2
Mean triangle surface	7.45 E-05 m^2	2.59 E-04 m^2
PC Density	185 503	57 838
Max. Distance	0.04 m	
Mean Distance	0.0006 m	

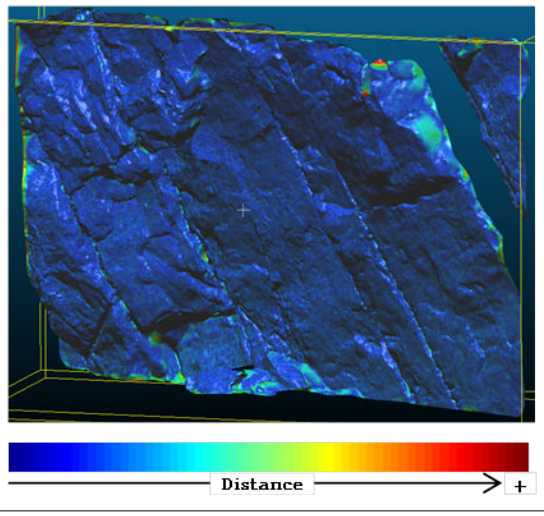

Figure A.17: Measured distances between Smart3D Capture model with five photos and 123D Catch model with five photos

In order to assess the accuracy between Sirovision, which uses georeferencing as scaling

method, and 123D Catch, that scale the model by a reference distance, 3D models created with the minimum quantity of images were used. The comparison is presented in Figure A.18. The mean distance calculated between both point clouds is 2 cm.

Model	Compared	Reference
Name	VF 2 photos Sirovision	VF 3 photos 123D Catch
Mesh surface	11.96 m^2	12.61 m^2
Mean triangle surface	1.32 E-4 m^2	3.15 E-04 m^2
PC Density	90 606	40 032
Max. Distance	0.08 m	
Mean Distance	0.02 m	

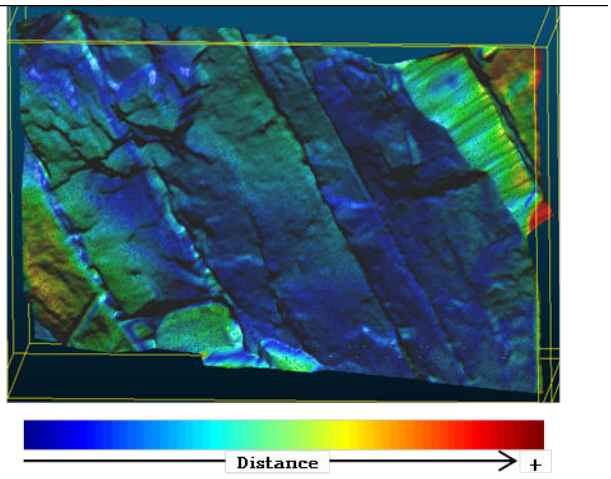

Figure A.18: Measured distances between Sirovision model with two photos and 123D Catch model with three photos

The comparison between Sirovision and Agisoft PhotoScan Pro is presented Figure A.19, which are software using the georeferencing process as scaling method. The calculated mean distance was 3 cm and the maximum distance was 18 cm. This discrepancy was localised mainly at the hidden areas that were not registered on the 2D image due to the camera position during the shot (see right side of Figure A.19).

Model	Compared	Reference
Name	VF 2 photos Sirovision	VF 5 photos Agisoft Pro
Mesh surface	11.96 m^2	14.73 m^2
Mean triangle surface	1.32 E-4 m^2	7.36 E-05 m^2
PC Density	90 606	200 136
Max. Distance	0.18 m	
Mean Distance	0.03 m	

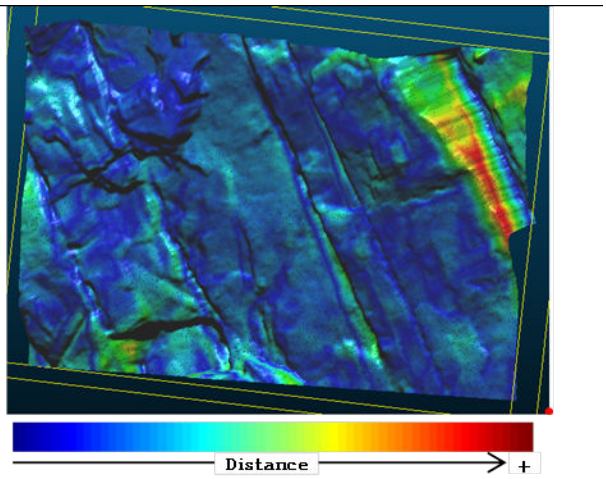

Figure A.19: Measured distances between Sirovision model with two photos and Agisoft PhotoScan Pro model with five photos

The 3D model created using Sirovision was compared with the model obtained using Smart3D Capture. The maximum distances were still localised at the hidden areas, as observed in Figure A.20.

Model	Compared	Reference
Name	VF 2 photos Sirovision	VF 5 photos 3D Capture
Mesh surface	11.96 m^2	13.82 m^2
Mean triangle surface	1.32 E-4 m^2	7.45 E-05 m^2
PC Density	90 606	185 503
Max. Distance	0.07 m	
Mean Distance	0.02 m	

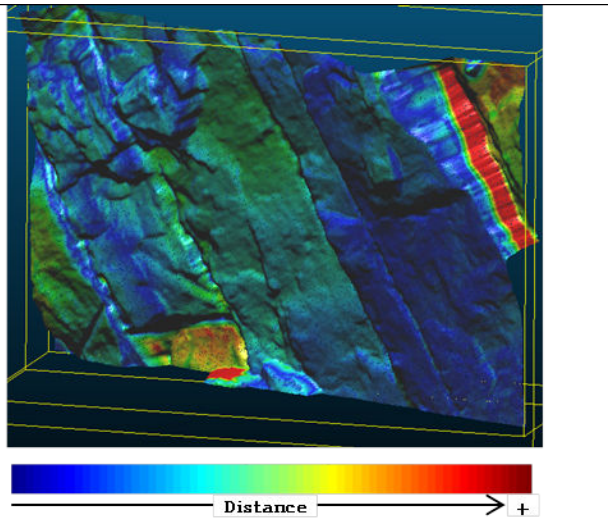

Figure A.20: Measured distances between Sirovision model with two photos and Smart3D Capture model with five photos

When comparing two models using the minimum and the maximum quantity of pho-

tographs used during this test, two and eleven respectively, the mean distance was 2 cm.

Model	Compared	Reference
Name	VF 2 photos Sirovision	VF 11 photos 123D Catch
Mesh surface	11.96 m^2	20.36 m^2
Mean triangle surface	1.32 E-4 m^2	7.36 E-05 m^2
PC Density	90 606	276 630
Max. Distance	0.05 m	
Mean Distance	0.02 m	

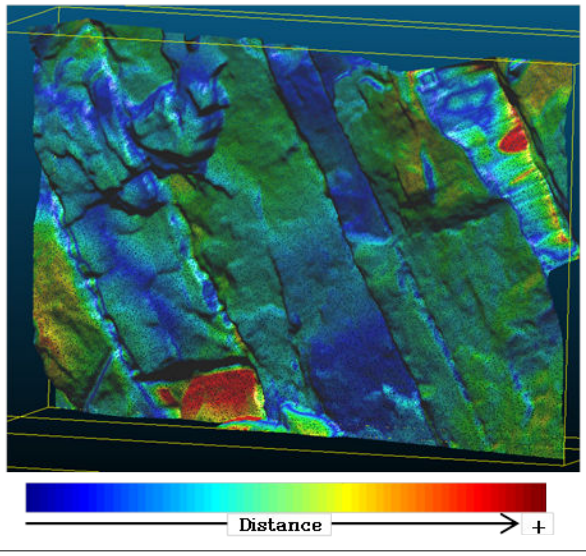

Figure A.21: Measured distances between Sirovision model with two photos and 123D Catch model with eleven photos

Structural analysis using Sirovision and magnetic portable compass

In the framework of this test, we obtained several 3D models of a 10×10 m^2 vertical portion of rock slope, localised at the Bastille hill in Grenoble (France). Between the software used, there is Sirovision, which is the single one among the others that facilitates the structural analysis of the slope.

Data acquisition and comparison

Once the 3D image is created, digital identification of structural features on the slope was carried out manually. *Trace* and *Plane* tools were used to identify and characterise the vertical joint planes and the rock face, respectively (see Figure A.22a and A.22b).

In order to compare the accuracy of structural data such as dip angle and dip direction (DDN) obtained from Sirovision 3D image, the same data were surveyed using a magnetic portable compass. The Boussoles universelle CHAIX compass has a precision of $\pm$ 2°. The

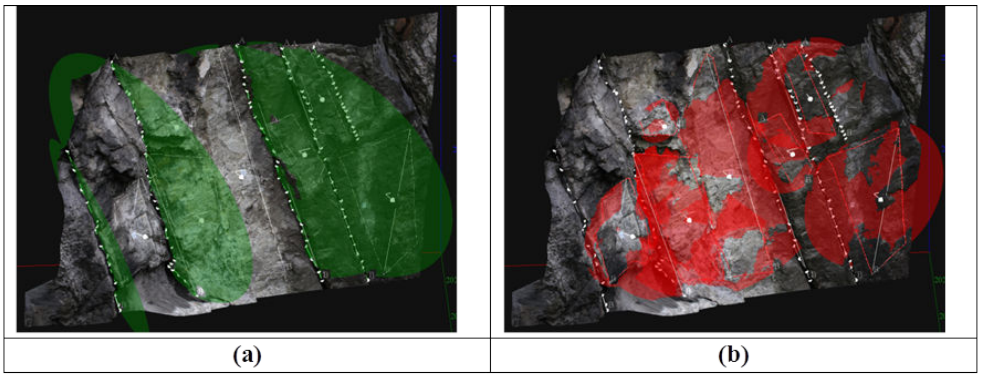

Figure A.22: Digital identification of structural features. (a) vertical joint planes. (b) rock face planes

results are presented in Figure A.23; here, the principal and easily accessible features were measured and compared.

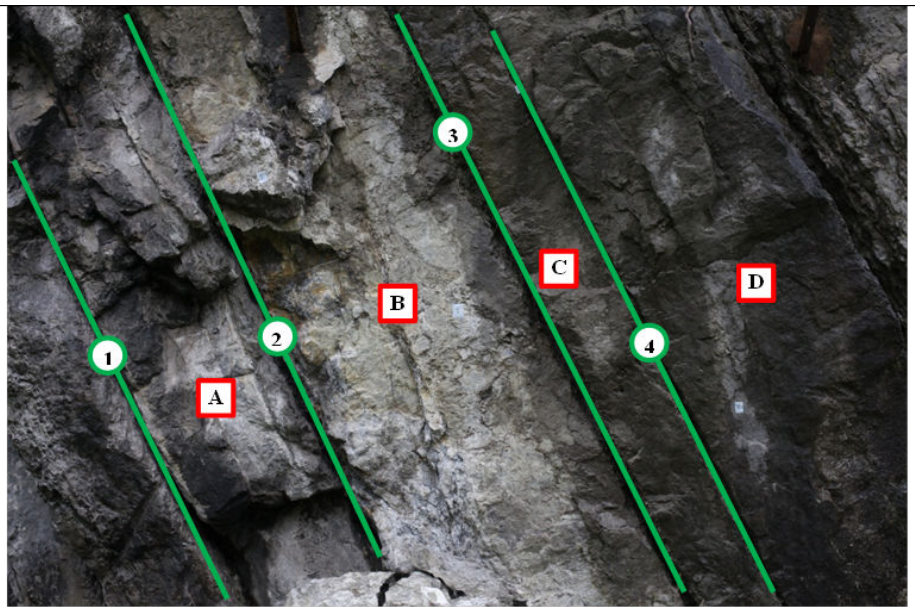

Modeled data			Surveyed data		
Plane	**Dip [°]**	**DDN [°]**	**Plane**	**Dip [°]**	**DDN [°]**
1	72.4	253.6	1	69.0	215.0
2	74.1	233.2	2	72.0	200.0
3	76.1	211.8	3	71.0	193.0
4	74.6	217.2	4	73.0	211.0
A	84.5	317.1	A	84.0	284.0
B	87.2	336.4	B	88.0	300.0
C	79.2	336.6	C	81.0	294.0
D	90.0	333.5	D	85.0	291.0

Figure A.23: Structural data comparison between Sirovision and a magnetic compass

In Figure A.24, dip values obtained by modelling and surveying were plotted for comparison. The differences oscillates between 0.5° (Plane A) and 5.1° (Plane 3).

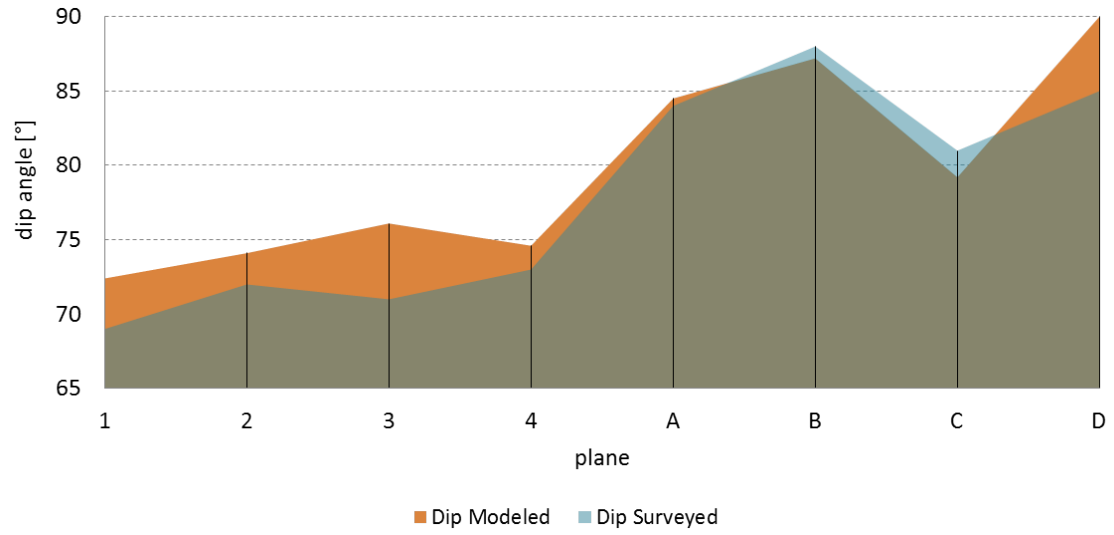

Figure A.24: Dip angle comparison

The dip direction (DDN) were compared and plotted in Figure A.25. Here, the differences are considerable, oscillating between 6.2° (Plane A) and 42.6° (Plane C).

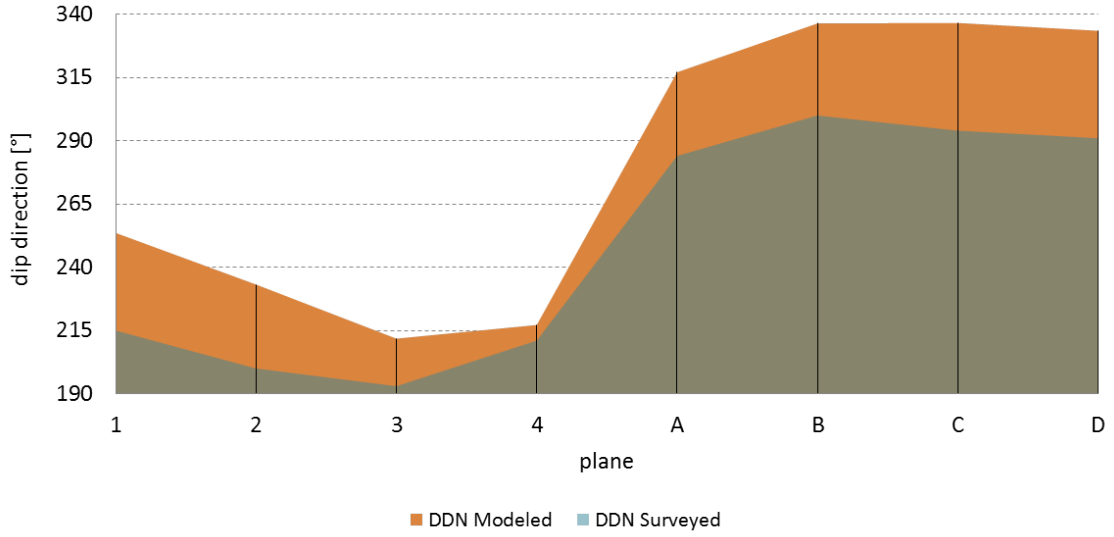

Figure A.25: Dip direction (DDN) comparison

Discussion

The main objective of this work was to assess the respective performance of the different software and their associated methodologies, to build up 3D slope surfaces used to calculate volumes and perform structural analysis.

According to the test configuration used, the CV-based techniques which perfoms a process automation that provides a precision comparable to the software specifically developed for 3D survey, *e.g.* Sirovision. Autodesk 123D Catch proved to be an interesting tool to perform 3D reconstruction. It provides a good quality 3D model from a set of good quality 2D images (good overlapping and resolution). Cubify Capture Beta, which is another automatic solution for 3D reconstruction, was successful only once during this test and several attempts to obtain the model using more than eleven images, gave no results.

The difficulties encountered to get results using using Pix4UAV Desktop 3D, suggest that the number of images (here, a maximum of eleven photos were used) were not enough. It is possible that hundreds of photographs may be required to create a good quality 3D model using this software.

3D models that were scaled by georeferencing, such as Agisoft PhotoScan Pro, Smart3D Capture (three images model) and Sirovision, were good quality 3D models, with an accuracy of $\pm$ 5 cm, which was expected for a distances to the target ranging from 6 to 7 m.

Note that Sirovision provides different methods to perform the georeferencing process: geoposition data from both or a single 2D image + GCP data, geoposition data from both 2D images, or just GCP data. The best results were obtained using just the five GCP surveyed. Using the others methods, the differences between the distances measured and modelled were about 12% and 15%. This error may be produced by the geolocalisation of the cameras, which was not precise enough to use these options successfully.

The mean difference between dip angle surveyed with a magnetic compass and modelled using Sirovision was 2.5°. Moreover, for the dip direction (DDN), the average difference was 31.4°, which was expected due to the poor geolocalisation of the cameras was not precise enough to achieve an accurate georeferencing process. Nevertheless, the structural data obtained from Sirovision are comparable with the surveyed structural data taking into account the inherent precision of the compass and the user measuring skills.

Bibliography

3DSystems (2013). Cubify Capture Beta. http://cubify.com/products/software?tb_create_capture. Online; accessed 02-April-2013.

Acute3D (2012). *Smart3DCapture Evaluation: Getting Started*. 06560 France: Acute3D.

ADAM-Technology, I. (2007). 3DM Analyst 2.1, 3DM CalibCam 2.1. http://www.adamtech.com.au/.

Agisoft (2013). Agisoft PhotoScan Professional edition. http://agisoft.ru/products/photoscan/professional/. Online; accessed 02-April-2013.

Autodesk (2013). 123D Catch - Autodesk 123D Applications. http://www.123dapp.com/catch. Online; accessed 02-April-2013.

Baczynski, N. et al. (2000). STEPSIM4 step-path methods for slope risks. In *Proceedings of the International Conference on Geotechnical and Geological Engineering (GeoEng 2000), Melbourne, Australia*, pp. 86–92.

Barazzetti, L., F. Remondino, and M. Scaioni (2010). Automation in 3D reconstruction: Results on different kinds of close-range blocks. In *ISPRS Commission V Symposium Int. Archives of Photogrammetry, Remote Sensing and Spatial Information Sciences, Newcastle upon Tyne, UK*, Volume 38.

Beale, G., J. Read, et al. (2014). *Guidelines for Evaluating Water in Pit Slope Stability*. CSIRO.

Belheine, N., J. Plassiard, F. V. Donzé, F. Darve, and A. Seridi (2009). Numerical simulation of drained triaxial test using 3D discrete element modeling. *Computers and Geotechnics 36*(1–2), 320 – 331.

Birch, J. (2006). Using 3DM analyst mine mapping suite for rock face characterization.

In *Laser and Photogrammetric Methods for Rock Face Characterization Workshop*, pp. 13–32.

Bonilla-Sierra, V., L. Scholtès, F. V. Donzé, and M. Elmouttie (2015). Rock slope stability analysis using photogrammetric data and DFN–DEM modelling. *Acta Geotechnica 10*(4), 497–511.

Bonilla–Sierra, V., L. Scholtès, F. Donzé, and M. Elmouttie (2015). DEM analysis of rock bridges and the contribution to rock slope stability in the case of translational sliding failures. *International Journal of Rock Mechanics and Mining Sciences 80*, 67 – 78.

Bonnet, E., O. Bour, N. E. Odling, P. Davy, I. Main, P. Cowie, and B. Berkowitz (2001). Scaling of fracture systems in geological media. *Reviews of geophysics 39*(3), 347–383.

Bottelin, P., D. Jongmans, D. Daudon, A. Mathy, A. Helmstetter, V. Bonilla-Sierra, H. Cadet, D. Amitrano, V. Richefeu, L. Lorier, et al. (2014). Seismic and mechanical studies of the artificially triggered rockfall at the Mount Néron (French Alps, December 2011). *Natural Hazards and Earth System Sciences Discussions 2*, 1505–1557.

Bour, O. and P. Davy (1999). Clustering and size distributions of fault patterns: Theory and measurements. *Geophysical Research Letters 26*(13), 2001–2004.

Brideau, M.-A., M. Yan, and D. Stead (2009). The role of tectonic damage and brittle rock fracture in the development of large rock slope failures. *Geomorphology 103*(1), 30–49.

Courchay, J., J.-P. Pons, P. Monasse, and R. Keriven (2010). Dense and accurate spatio-temporal multi-view stereovision. In *Computer Vision–ACCV 2009*, pp. 11–22. Springer.

Cundall, P., M. Pierce, and D. Mas-Ivars (2008). Quantifying the size effect of rock mass strength. In *Proceedings of the 1st Southern Hemisphere International Rock Mechanics Symposium*, pp. 3–15. Australian Centre for Geomechanics (ACG).

Cundall, P. A. and R. D. Hart (1992). Numerical modelling of discontinua. *Engineering computations 9*(2), 101–113.

Damjanac, B., P. Cundall, et al. (2013). Validation of lattice approach for rock stability problems. In *47th US Rock Mechanics/Geomechanics Symposium*. American Rock Mechanics Association.

Darcel, C., O. Bour, P. Davy, and J. De Dreuzy (2003). Connectivity properties of two-dimensional fracture networks with stochastic fractal correlation. *Water resources research 39*(10).

Davy, P., R. Le Goc, C. Darcel, O. Bour, J.-R. De Dreuzy, and R. Munier (2010). A likely universal model of fracture scaling and its consequence for crustal hydromechanics. *Journal of Geophysical Research: Solid Earth (1978–2012) 115*(B10).

de Berg, M., O. Cheong, M. van Kreveld, and M. Overmars (2008). *Computational Geometry: Algorithms and Applications*. Springer Science & Business Media.

Deparis, J., S. Garambois, and D. Hantz (2007). On the potential of ground penetrating radar to help rock fall hazard assessment: A case study of a limestone slab, Gorges de la Bourne (French Alps). *Engineering Geology 94*(1), 89–102.

Dershowitz, W. S. (1984). *Rock joint systems*. Ph. D. thesis, Massachusetts Institute of Technology, USA.

Donzé, F. V., V. Richefeu, and S.-A. Magnier (2009). Advances in discrete element method applied to soil, rock and concrete mechanics. *State of the art of geotechnical engineering. Electronic Journal of Geotechnical Engineering 44*, 31.

Donzé, F. V. and S. A. Magnier (1995). Formulation of a 3D numerical model of brittle behaviour. *Geophysical Journal International 122*(3), 790–802.

Eberhardt, E. (2008). The role of advanced numerical methods and geotechnical field measurements in understanding complex deep-seated rock slope failure mechanisms. *Canadian Geotechnical Journal 45*(4), 484–510.

Eberhardt, E., D. Stead, and J. Coggan (2004). Numerical analysis of initiation and progressive failure in natural rock slopes—the 1991 Randa rockslide. *International Journal of Rock Mechanics and Mining Sciences 41*(1), 69 – 87.

Echelard, T. (2014). *Contribution à l'étude de la dynamique des glaciers rocheux dans les Alpes françaises par interférométrie radar différentielle (D-InSAR)*. Ph. D. thesis, Université Joseph Fourier, France.

Einstein, H., D. Veneziano, G. Baecher, and K. O'Reilly (1983). The effect of discontinuity persistence on rock slope stability. *International Journal of Rock Mechanics and Mining Sciences and Geomechanics Abstracts 20*(5), 227 – 236.

Elmo, D., K. Moffitt, S. D'Ambra, and D. Stead (2009). Characterisation of brittle rock fracture mechanisms in rock slope failures. In *Proceedings of 2009 International Symposium on Rock Slope Stability in Open Pit Mining and Civil Engineering, Chile, Santiago*, pp. 1–11.

Elmouttie, M., G. Krähenbühl, G. Poropat, and I. Kelso (2014). Stochastic representation of sedimentary geology. *Rock mechanics and rock engineering 47*(2), 507–518.

Elmouttie, M. and G. Poropat (2012). A method to estimate in situ block size distribution. *Rock mechanics and rock engineering 45*(3), 401–407.

Elmouttie, M. and G. Poropat (2014). Quasi-stochastic analysis of uncertainty for modelling structurally controlled failures. *Rock mechanics and rock engineering 47*(2), 519–534.

Elmouttie, M., G. Poropat, and P. Soole (2012). Open cut mine wall stability analysis

utilising discrete fracture networks - ACARP C20029 Final Report. Technical report, CSIRO.

Esmaieli, K., J. Hadjigeorgiou, and M. Grenon (2010). Estimating geometrical and mechanical REV based on synthetic rock mass models at Brunswick mine. *International Journal of Rock Mechanics and Mining Sciences 47*(6), 915–926.

Fabre, D., L. Lorier, A. Mathy, and D. Hantz (2013). Gestion d'un risque rocheux en zone urbanisée: le cas des rochers du Néron près de Grenoble (Isère-France). In *Proceedings of the 1st international conference on Landslides risk, 14-15-16 Mars 2013*, pp. 149–162.

Farve, R. (2010). Evaluation of laser rangefinders. Technical report, U.S. Department of Agriculture.

Favalli, M., A. Fornaciai, I. Isola, S. Tarquini, and L. Nannipieri (2012). Multiview 3D reconstruction in geosciences. *Computers & Geosciences 44*, 168–176.

Firpo, G., R. Salvini, M. Francioni, and P. Ranjith (2011). Use of digital terrestrial photogrammetry in rocky slope stability analysis by distinct elements numerical methods. *International Journal of Rock Mechanics and Mining Sciences 48*(7), 1045–1054.

Francioni, M., R. Salvini, D. Stead, and S. Litrico (2014). A case study integrating remote sensing and distinct element analysis to quarry slope stability assessment in the Monte Altissimo area, Italy. *Engineering Geology 183*, 290–302.

Frayssines, M. and D. Hantz (2009). Modelling and back-analysing failures in steep limestone cliffs. *International Journal of Rock Mechanics and Mining Sciences 46*(7), 1115–1123.

Gates, W., W. Haneberg, et al. (2012). Comparison of standard structural mapping results to 3D photogrammetric model results: Boundary transformer banks rockfall mitigation project, Metaline Falls, Washington. In *Proceedings American Rock mechanics Association, 46th US Rock Mechanics/Geomechanics Symposium held in Chicago, IL, USA, 24–27 June*.

Gidon, M. and H. Arnaud (1978). Carte géologique détaillée de la France à 1/50 000ème, feuille Grenoble.

Graça, S., J. F. Oliveira, and V. Realinho (2012). Worldplus: An augmented reality application with georeferenced content for smartphones-the Android example.

Grenon, M., G. Bruneau, and I. K. Kalala (2014). Quantifying the impact of small variations in fracture geometric characteristics on peak rock mass properties at a mining project using a coupled DFN–DEM approach. *Computers and Geotechnics 58*, 47 – 55.

Hammah, R., T. Yacoub, B. Corkum, J. Curran, et al. (2005). The shear strength reduction method for the generalized Hoek - Brown criterion. In *Alaska Rocks 2005, The 40th US Symposium on Rock Mechanics (USRMS)*. American Rock Mechanics Association.

Haneberg, W. C. (2008). Using close range terrestrial digital photogrammetry for 3D rock slope modeling and discontinuity mapping in the united states. *Bulletin of Engineering Geology and the Environment 67*(4), 457–469.

Harthong, B., L. Scholtès, and F. V. Donzé (2012). Strength characterization of rock masses, using a coupled DEM-DFN model. *Geophysical Journal International 191*(2), 467–480.

Hass, C. (2008). JPEG Rotation and EXIF Orientation. http://www.impulseadventure.com/photo/exif-orientation.html. Online; accessed 19-March-2013.

Havaej, M., J. Coggan, D. Stead, and D. Elmo (2015). A combined remote sensing–numerical modelling approach to the stability analysis of delabole slate quarry, cornwall, uk. *Rock Mechanics and Rock Engineering*, 1–19.

Havaej, M., D. Stead, E. Eberhardt, and B. R. Fisher (2014). Characterization of bi-planar and ploughing failure mechanisms in footwall slopes using numerical modelling. *Engineering Geology 178*, 109–120.

Hoek, E. (1983). Strength of jointed rock masses, 23rd. Rankine lecture. *Géotechnique 33*(3), 187–223.

Hoek, E. and J. D. Bray (1981). *Rock slope engineering*. CRC Press.

Hoek, E. and E. Brown (1997). Practical estimates of rock mass strength. *International Journal of Rock Mechanics and Mining Sciences 34*(8), 1165–1186.

Hoek, E. and E. T. Brown (1980). *Underground excavations in rock*. London: The Institute of Mining and Metallurgy.

Hoek, E., C. Carranza-Torres, and B. Corkum (2002). Hoek - Brown failure criterion-2002 edition. *Proceedings of NARMS-Tac 1*, 267–273.

Jennings, J. (1970). A mathematical theory for the calculation of the stability of slopes in open cast mines. In *In Van Rensburg, P. (Eds.), Planning open pit mines: Proceedings of the Symposium on the Theoretical Background to the Planning of Open Pit Mines with Special Reference to Slope Stability, Johannesburg, Republic of South Africa*, pp. 87–102.

Kemeny, J. (2003). The time-dependent reduction of sliding cohesion due to rock bridges along discontinuities: a fracture mechanics approach. *Rock Mechanics and Rock Engineering 36*(1), 27–38.

Kersten, T. P. and M. Lindstaedt (2012). Image-based low-cost systems for automatic 3D recording and modelling of archaeological finds and objects. In *Progress in cultural heritage preservation*, pp. 1–10. Springer.

Kozicki, J. and F. V. Donzé (2008). A new open-source software developed for numerical

simulations using discrete modeling methods. *Computer Methods in Applied Mechanics and Engineering 197*(49), 4429–4443.

Kozicki, J. and F. V. Donzé (2009). YADE - OPEN DEM: an open-source software using a discrete element method to simulate granular material. *Engineering Computations 26*(7), 786–805.

Lambert, C., K. Thoeni, A. Giacomini, D. Casagrande, and S. Sloan (2012). Rockfall hazard analysis from discrete fracture network modelling with finite persistence discontinuities. *Rock mechanics and rock engineering 45*(5), 871–884.

Lévy, C. (2011). *Etude instrumentale et numérique de la réponse dynamique d'une écaille calcaire potentiellement instable*. Ph. D. thesis, Université de Grenoble, France.

Li, S.-H., B. Gao, and L. Yan (2002). 3D simulation of the excavation of high steep slope of Three-Gorges permanent lock by distinct element method. *Rock and soil mechanics - Wuhan - 23*(3), 272–277.

Mas-Ivars, D., M. E. Pierce, C. Darcel, J. Reyes-Montes, D. O. Potyondy, R. P. Young, and P. A. Cundall (2011). The synthetic rock mass approach for jointed rock mass modelling. *International Journal of Rock Mechanics and Mining Sciences 48*(2), 219–244.

Mejía-Camones, L. A., E. do Amaral Vargas, R. P. de Figueiredo, and R. Q. Velloso (2013). Application of the discrete element method for modeling of rock crack propagation and coalescence in the step-path failure mechanism. *Engineering Geology 153*, 80–94.

Miller, S. M., J. K. Whyatt, E. L. McHugh, et al. (2004). Applications of the point estimation method for stochastic rock slope engineering. In *Proceedings, Rock Mechanics Across Borders and Disciplines, 6th North American Rock Mechanics Conference, Gulf Rocks 2004*, pp. 1–12.

Nguyen, H. M., B. Wünsche, P. Delmas, and C. Lutteroth (2012). 3D models from the black box: investigating the current state of image-based modeling. In *20th International Conference on Computer Graphics, Visualization and Computer Vision*. Václav Skala-Union Agency.

Pariseau, W. G., S. Puri, and S. C. Schmelter (2008). A new model for effects of impersistent joint sets on rock slope stability. *International Journal of Rock Mechanics and Mining Sciences 45*(2), 122–131.

Petrie, G. (2013). Commercial operation of lightweight UAVs for aerial imaging and mapping. *GEO Informatics 16*, 28–39.

Pix4D (2012). Pix4UAV Desktop. http://pix4d.com/pix4uav_product.html. Online; accessed 02-April-2013.

Poropat, G. (2001). New methods for mapping the structure of rock masses. In *Proceed-*

ings, Explo 2001, pp. 253–260.

Poropat, G. V. (2006). Remote 3D mapping of rock mass structure. pp. 63–75.

Potyondy, D. and P. Cundall (2004). A bonded-particle model for rock. *International journal of rock mechanics and mining sciences 41*(8), 1329–1364.

Pouya, A. (2015). A finite element method for modeling coupled flow and deformation in porous fractured media. *International Journal for Numerical and Analytical Methods in Geomechanics*.

Read, J. (2007). Predicting the behaviour and failure of large rock slopes. rock mechanics meeting society's challenges and demands. In *Proceedings of the 1st Canada US Rock Mechanics Symposium, Vancouver, Canada*, Volume 1, pp. 1237–1243.

Read, J., P. Stacey, et al. (2009). *Guidelines for open pit slope design*. CSIRO.

Rogers, S., D. Kennard, W. Dershowitz, and A. Van As (2007). Characterising the in situ fragmentation of a fractured rock mass using a discrete fracture network approach. In *Rock mechanics: Meeting society's challenges and demands, Proceedings of the 1st Canada-US Rock Mechanics Symposium. Vancouver, Canada: Taylor & Francis*, pp. 137–143.

Salvini, R., M. Francioni, S. Riccucci, F. Bonciani, and I. Callegari (2013). Photogrammetry and laser scanning for analyzing slope stability and rock fall runout along the domodossola–iselle railway, the italian alps. *Geomorphology 185*, 110–122.

Scavia, C. (1990). Fracture mechanics approach to stability analysis of rock slopes. *Engineering Fracture Mechanics 35*(4), 899–910.

Scholtès, L. and F. V. Donzé (2012). Modelling progressive failure in fractured rock masses using a 3D discrete element method. *International Journal of Rock Mechanics and Mining Sciences 52*, 18–30.

Scholtès, L. and F. V. Donzé (2013). A DEM model for soft and hard rocks: Role of grain interlocking on strength. *Journal of the Mechanics and Physics of Solids 61*(2), 352–369.

Scholtès, L. and F. V. Donzé (2015). A DEM analysis of step-path failure in jointed rock slopes. *Comptes Rendus Mecanique 343*(2), 155–165.

Scholtès, L., F. V. Donzé, and M. Khanal (2011). Scale effects on strength of geomaterials, case study: coal. *Journal of the Mechanics and Physics of Solids 59*(5), 1131–1146.

Sirovision (2010). *Sirovision 3D Imaging Mapping System Manual Version 4.1*. CSIRO.

Šmilauer, V., E. Catalano, B. Chareyre, S. Dorofeenko, J. Duriez, A. Gladky, J. Kozicki, C. Modenese, L. Scholtès, L. Sibille, et al. (2010). *Yade reference documentation*. http://yade-dem.org/doc/: In Yade Documentation (V. Šmilauer, ed.), The Yade

Project.

Stead, D., E. Eberhardt, and J. Coggan (2006). Developments in the characterization of complex rock slope deformation and failure using numerical modelling techniques. *Engineering Geology 83*(1), 217–235.

Stead, D., E. Eberhardt, J. Coggan, and B. Benko (2001). Advanced numerical techniques in rock slope stability analysis—applications and limitations. In *International Conference on Landslides-Causes, Impacts and Countermeasures*, pp. 615–624.

Stead, D. and A. Wolter (2015). A critical review of rock slope failure mechanisms: The importance of structural geology. *Journal of Structural Geology 74*, 1–23.

Strecha, C. (2011). Automated photogrammetric techniques on ultra-light UAV imagery. pp. 289–294.

Strecha, C., A. M. Bronstein, M. M. Bronstein, and P. Fua (2012). LDAHash: Improved matching with smaller descriptors. *Pattern Analysis and Machine Intelligence, IEEE Transactions on 34*(1), 66–78.

Sturzenegger, M. (2010). *Multi-scale characterization of rock mass discontinuities and rock slope geometry using terrestrial remote sensing techniques*. Ph. D. thesis, Simon Fraser University, Burnaby, BC, Canada.

Sturzenegger, M. and D. Stead (2009). Close-range terrestrial digital photogrammetry and terrestrial laser scanning for discontinuity characterization on rock cuts. *Engineering Geology 106*(3-4), 163–182.

Sturzenegger, M. and D. Stead (2012). The Palliser rockslide, Canadian rocky mountains: characterization and modeling of a stepped failure surface. *Geomorphology 138*(1), 145–161.

Sturzenegger, M., D. Stead, and D. Elmo (2011). Terrestrial remote sensing-based estimation of mean trace length, trace intensity and block size/shape. *Engineering Geology 119*(3), 96–111.

Travelletti, J., C. Delacourt, P. Allemand, J.-P. Malet, J. Schmittbuhl, R. Toussaint, and M. Bastard (2012). Correlation of multi-temporal ground-based optical images for landslide monitoring: Application, potential and limitations. *ISPRS Journal of Photogrammetry and Remote Sensing 70*, 39–55.

Wang, C., D. Tannant, and P. Lilly (2003). Numerical analysis of the stability of heavily jointed rock slopes using PFC-2D. *International Journal of Rock Mechanics and Mining Sciences 40*(3), 415 – 424.

Wang, L., S. Yamashita, F. Sugimoto, C. Pan, and G. Tan (2003). A methodology for predicting the in situ size and shape distribution of rock blocks. *Rock Mechanics and Rock Engineering 36*(2), 121–142.

Wiesen, G. and H. Bailey (2013). What is Photogrammetry Software? http://www.wisegeek.com/what-is-photogrammetry-software.htm/. Online; accessed 07-February-2013.

Wittke, W. (1990). *Rock mechanics: Theory and applications, with case histories*. Springer-Verlag.

Wyllie, D. C. and C. Mah (2004). *Rock slope engineering*. CRC Press.

Zhang, L. and H. Einstein (2000). Estimating the intensity of rock discontinuities. *International Journal of Rock Mechanics and Mining Sciences 37*(5), 819–837.

Zi, G. and T. Belytschko (2003). New crack-tip elements for xfem and applications to cohesive cracks. *International Journal for Numerical Methods in Engineering 57*(15), 2221–2240.